ARO-UR Center for

OPTO-ELECTRONIC SYSTEMS RESEARCH

TECHNICAL REPORT

INTERACTION OF ATOMIC HYDROGEN WITH PICO- AND FEMTOSECOND LASER PULSES

Jonathan S. Parker

December 1989

The Institute of Optics
University of Rochester

Prepared for:

U.S. Army Research Office
ATTN: DRXRO-IP-Library
P. O. Box 12211
Research Triangle Park, NC 27709

UNCLASSIFIED
SECURITY CLASSIFICATION OF THIS PAGE

REPORT DOCUMENTATION PAGE

1a. REPORT SECURITY CLASSIFICATION Unclassified	1b. RESTRICTIVE MARKINGS
2a. SECURITY CLASSIFICATION AUTHORITY	3. DISTRIBUTION / AVAILABILITY OF REPORT Approved for public release; distribution unlimited.
2b. DECLASSIFICATION / DOWNGRADING SCHEDULE	
4. PERFORMING ORGANIZATION REPORT NUMBER(S)	5. MONITORING ORGANIZATION REPORT NUMBER(S) ARO 24626.126-PH-UIR
6a. NAME OF PERFORMING ORGANIZATION University of Rochester 6b. OFFICE SYMBOL (If applicable)	7a. NAME OF MONITORING ORGANIZATION U. S. Army Research Office
6c. ADDRESS (City, State, and ZIP Code) The Institute of Optics Rochester, New York 14627	7b. ADDRESS (City, State, and ZIP Code) P. O. Box 12211 Research Triangle Park, NC 27709-2211
8a. NAME OF FUNDING / SPONSORING ORGANIZATION U. S. Army Research Office 8b. OFFICE SYMBOL (If applicable)	9. PROCUREMENT INSTRUMENT IDENTIFICATION NUMBER DAAL03-86-K-0173
8c. ADDRESS (City, State, and ZIP Code) P. O. Box 12211 Research Triangle Park, NC 27709-2211	10. SOURCE OF FUNDING NUMBERS PROGRAM ELEMENT NO. / PROJECT NO. / TASK NO. / WORK UNIT ACCESSION NO.

11. TITLE (Include Security Classification)
Interaction of Atomic Hydrogen with Pico- and Femtosecond Laser Pulses

12. PERSONAL AUTHOR(S)
Jonathan S. Parker

13a. TYPE OF REPORT	13b. TIME COVERED	14. DATE OF REPORT (Year, Month, Day)	15. PAGE COUNT
Technical	FROM _____ TO _____	December 1989	134

16. SUPPLEMENTARY NOTATION
The view, opinions and/or findings contained in this report are those of the author(s) and should not be construed as an official Department of the Army position, policy, or decision, unless so designated by other documentation.

17. COSATI CODES			18. SUBJECT TERMS (Continue on reverse if necessary and identify by block number)
FIELD	GROUP	SUB-GROUP	multiphoton ionization; ultra-intense fields; above threshold ionization

19. ABSTRACT (Continue on reverse if necessary and identify by block number)

See Abstract on Page iv-v

20. DISTRIBUTION / AVAILABILITY OF ABSTRACT ☐ UNCLASSIFIED/UNLIMITED ☐ SAME AS RPT. ☐ DTIC USERS	21. ABSTRACT SECURITY CLASSIFICATION Unclassified
22a. NAME OF RESPONSIBLE INDIVIDUAL Carlos R. Stroud, Jr.	22b. TELEPHONE (Include Area Code) 716-275-2598 22c. OFFICE SYMBOL

DD FORM 1473, 84 MAR 83 APR edition may be used until exhausted. All other editions are obsolete.

SECURITY CLASSIFICATION OF THIS PAGE
UNCLASSIFIED

INTERACTION OF ATOMIC HYDROGEN WITH PICO- AND FEMTOSECOND LASER PULSES

by

Jonathan S. Parker

Submitted in Partial Fulfillment

of the

Requirements for the Degree

DOCTOR OF PHILOSOPHY

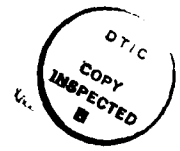

Supervised by Carlos R. Stroud, Jr.

The Institute of Optics

University of Rochester

Rochester, New York

1989

CURRICULUM VITAE

The author was born on December 13, 1956 in Rochester Minnesota. From 1974 to 1979 he attended the University of Minnesota, in Minneapolis, Minnesota. There he received a Bachelor of Science degree and graduated with high distinction. He began graduate study at the Institute of Optics at the University of Rochester in 1982. At the Institute of Optics he has conducted research in theoretical quantum optics and atomic physics under the supervision of Carlos R. Stroud, Jr.

ACKNOWLEDGMENTS

It is a pleasure to acknowledge the many people who aided me in this research, directly and indirectly. I am particularly indebted to my thesis advisor Professor Carlos Stroud, Jr. His collaboration, support, and encouragement have been essential over and over again. I am also grateful to my co-workers and friends in Prof. Stroud's, Prof. Raymer's, and Prof. Boyd's research groups. A high percentage of them have done something on my behalf at one time or another. In particular I am indebted to John Yeazell and Mark Mallalieu for working with me on several problems, and also Karl Koch, Stephen Chakmakjian, Zagorka Dacic, Jeff Maki, and Bill Davis who have shown interest in my research and have engaged me in many useful discussions.

I gratefully acknowledge the financial support of The Institute of Optics, the Joint Services Optics Program, and the Army Reasearch Office.

ABSTRACT

This thesis presents a theoretical study of the interaction of atomic hydrogen with coherent laser pulses in the 5 femtosecond to 10 picosecond range, in the weak-field limit, and in intense fields. We approach the problem in the weak-field limit by studying the relationship between the Fourier relation of the laser pulse ($\Delta\omega\Delta t$) and the $\Delta E\Delta t$ relation of the atomic Rydberg wave packet generated by the laser pulse. A derivation of the wave packet based on the WKB approximation is given, permitting the quantity Δt to be derived for the quantum state, with the conclusion that under certain circumstances a transform-limited laser pulse (satisfying $\Delta\omega\Delta t = 1/2$) can generate a transform-limited electron (satisfying $\Delta E\Delta t/\hbar = 1/2$).

The interaction of hydrogen with femtosecond pulses is studied at field intensities as high as $2.2 \cdot 10^{14} W/cm^2$. The full three-dimensional Schrödinger equation is numerically integrated at intensities of this order as a guide to the development of theory. In terms of the Fermi golden rule (FGR) formulation of ionization, the results may be summarized as follows: just about every approximation employed in the derivation of FGR breaks down at $10^{14} W/cm^2$. Nevertheless, it was possible to provide straightforward non-perturbative methods to replace the approximations and perturbative methods employed in FGR.

A population-trapping effect is found numerically and modeled theoretically. Despite the high field intensities, population representing the excited electron is recaptured from the ionization continuum by bound states during the excitation. Population returns to the atom

with just the right phase to strongly inhibit ionization. A theory is presented that models this effect for a variety of laser pulse shapes, with and without the rotating-wave approximation.

The numerical integration reveals that a certain amount of above-threshold ionization (ATI) occurs. A theory similar to the Keldysh-type theories of ATI is developed. The theory differs from the Keldysh theories in that, like Schrödinger's equation, it is invariant under certain gauge transformations. The proposed theory gives far superior agreement with the numerical integration than Keldysh theory.

Classical ionization at $2.2 \cdot 10^{14} W/cm^2$ is studied by numerically integrating Newton's equation on a Monte Carlo ensemble constructed to correspond to the above examples.

TABLE OF CONTENTS

LIST OF FIGURES

PUBLICATIONS

1. J. Parker and C. R. Stroud Jr., "Coherence and decay of Rydberg wavepackets," Phys. Rev. Lett. **56**, pp.716-719 (1986).

2. J. Parker and C. R. Stroud Jr., "Transient theory of cavity modified spontaneous emission," Phys. Rev. A **35**, pp. 4226-4237 (1987).

3. J. Parker and C. R. Stroud Jr., "Rydberg wave packets and the classical limit," Physica Scripta **T12**, pp. 70-75 (1986).

4. M. Mallalieu, J. Parker, and C. R. Stroud Jr., "Transient absorption by a Rydberg atom in a resonant cavity", Phys. Rev. A **37**, pp. 4765-4768 (1988).

5. J. Parker and C. R. Stroud Jr., "Generalization of the Keldysh theory of above-threshold ionization for the case of femtosecond pulses," Phys. Rev. A **40**, 5651-5658 (1989).

6. J. A. Yeazell, Mark Mallalieu, J. Parker, and C. R. Stroud, Jr., "Observation of classical motion of atomic wave packets", Phys. Rev. A **40**, pp. 5040-5042 (1989).

7. J. Parker, and C. R. Stroud Jr., "Population trapping in short pulse ionization", To appear in Phys. Rev. A.

CHAPTER I
INTRODUCTION

The theoretical study of quasi-classical atomic states is as old as quantum mechanics. Lorentz and Schrödinger corresponded[1] on the subject of atomic wave packets and their relation to the classical correspondence as early as 1925. Schrödinger[2] discovered the minimum uncertainty wave packets of the harmonic oscillator in his search for the classical correspondence of his wave theory of electrons. However, only recently have methods been proposed to use short laser pulses to generate quasi-classical atomic states, and only recently has a connection been drawn between the coherence of laser pulses, and the coherence of the atomic wave packets generated by a laser pulse[3-7]. In the last two years there have been several successful experiments[8,9] in which mode-locked picosecond lasers have been used to generate atomic wave packets in one-electron atoms, and to probe their quasi-classical motion.

The development of mode-locked picosecond and femtosecond lasers has coincided with the advent of ultra-intense lasers capable of intensities in the 10^{13} to 10^{17} W/cm^2 range. The interaction of atoms with ultra-intense fields has produced a wealth of new experimental phenomena, some of it quite surprising. Of particular importance has been the discovery of above-threshold ionization (ATI) of xenon[10], in which an ionizing electron absorbs more than the minimum number of photons necessary to ionize. The energy spectrum of above-threshold ionized xenon

shows not just a single ionization peak, but sometimes as many as 20 or 30 ionization peaks separated by a photon in energy, $\hbar\omega$, where ω is the laser frequency. Above-threshold ionization has turned out to be a complex physical process that is dfficult to model accuately.

This thesis presents a study of the interaction of atomic hydrogen with pico- and femtosecond laser pulses, at laser intensities as high as $2.2 \cdot 10^{14}\,\mathrm{W/cm^2}$.

One of the goals of this research has been to demonstrate whenever feasible a wave packet interpretation of the physics of atom-laser interactions. Wave packets are solutions of the time-dependent Schrödinger equation that resemble in certain respects the motion of a particle in the classical trajectories of the corresponding classical systems. The ordinary differential equations of classical mechanics are easy to solve numerically, and once the solutions have been generated, the physics is easy to comprehend. This ease of understanding is lost in the transition to wave mechanics. Not only are partial differential equations difficult to solve and analyze, but Schrödinger's equation (in its coordinate form) is a boundary value problem; the nature of the boundary at some distance from the atom plays an essential role in the mathematical solution of the boundary value problem, and this complicates analysis of the physical processes that take place at the atom independently of the boundary. The solutions of time-dependent boundary value problems and Schrödinger's equation in particular are often conveniently written in terms of the stationary (time-independent) bound states of the cavity whose boundary gives rise to the boundary conditions. But in the ultra-fast laser-atom

interactions that are the subject of this thesis, the individual stationary states are by themselves poor representations of the state of the atom during and after the interaction. Instead, the state of the atom is represented by certain coherent superpositions of stationary states that in configuration space turn out to be a well-defined wave packet. Not only are wave packets the physical states of the atom, but they return to the problem some of the physical clarity that was lost in the transition from classical mechanics to wave mechanics.

In chapter II we begin analysis of the Schrödinger equation describing the interaction of atomic hydrogen with pico- and femtosecond laser pulses. A major goal is to demonstrate the wave packet character of the solutions and some of the classical and quantum mechanical characteristics of the wave packets. The solutions will also clarify the relationship between the wave packets and the set of stationary states used to solve the boundary value problem.

The theme of chapter II is motivated by the question: Are there any circumstances under which a transform limited laser pulse (satisfying $\Delta\omega\Delta t = 1/2$) may generate a minimum uncertainty wave packet? Chapter II presents numerical results demonstrating a wide range of circumstances under which near-minimum uncertainty radial wave packets are generated. The wave packets are localized in the radial variable $r = |r|$, but not in the angular variables θ and ϕ. The quantity minimized is the uncertainty product: $\Delta r \Delta p_r \simeq \hbar/2$. Analytically, a formula for the radial wave packet is derived using the WKB approximation, but a direct relationship between the laser pulse's Fourier relation $\Delta\omega\Delta t = 1/2$ and the

wave packet's uncertainty product $\Delta r \Delta p_r$ is not found. Instead, we are able to define a time-energy relation $\Delta E \Delta t$ for the atomic wave packet (or more precisely, for the WKB wave packet), and it is this quantity that has a direct relationship with the time-frequency product of the laser pulse.

In chapter III and in succeeding chapters we focus on the problem of the hydrogen atom interacting with femtosecond laser pulses at intensities of $2 \cdot 10^{14}$ W/cm^2.

Chapter III is a general discussion of methods used to numerically integrate the three-dimensional Schrödinger's equation describing atomic hydrogen in intense coherent laser fields. A major goal of this research was to numerically integrate the three-dimensional Schrödinger's equation as a guide to the physics, and as a test of the theory. Such a program has a disadvantage in that numerical tests can only be applied to a limited number of examples and cases. Numerical algorithms for the solution of three-dimensional partial differential equations are laborious to develop and debug, and the computer programs can require days or weeks of computer time, even on the fastest computers. For that reason, in this thesis all theory and numerical examples have been restricted to the case in which a single photon of the field is sufficient in energy to ionize (or nearly ionize) the atom. However, the advantages of numerically integrating the three-dimensional Schrödinger's equation are many. In particular:

1. It is a means of testing the utility of basic techniques and approximations used in atomic physics, e.g. the rotating-wave

approximation, essential-states approximation, zeroth-order Born approximation.

2. It is a powerful means finding and explaining unexpected physical phenomena.

3. It proves to be a useful guide to developing theory by quickly revealing which approximations are good and which are bad. This is particularly important in the study of complicated phenomena like ATI, where there is some controversy and confusion.

4. It is a means of improving the likelihood that the numerical results and the accompanying theory, if successful, have some applicability in real-world experiments.

In chapter III we also discuss some of the results of the numerical integration. The specific example chosen assumed a laser pulse of intensity $2.2 \cdot 10^{14}$ W/cm^2, and duration 7.5 femtoseconds. The initial state was chosen to be the ($n=3$, $\ell=2$, $m=2$) state, and the laser was tuned so that a single photon was sufficient to ionize the atom. Two particularly interesting phenomena were apparent in the numerical example studied. The first effect was the above-threshold ionization of the atom. Instead of absorbing a single photon during ionization, the electron could in some cases absorb two, three or four photons. Instead of a single ionization peak in the ionization spectrum, four ionization peaks were present, separated in energy by about the energy of one photon. The second effect may be described as a population-trapping effect. Population remains trapped in the initial state throughout the laser interaction despite the fact that a Fermi golden rule (FGR) calculation predicts that laser fields an order of

magnitude less intense should be sufficient to ionize the atom. Both the ATI and the population trapping effects may be regarded as fundamental ways in which FGR fails in the intense field limit.

The origin of the population trapping is easily determined by removing basis states from the basis set during the numerical integration. This technique reveals that bound states with the same angular momentum as the initial state have a profound influence on the physics of the laser atom interaction. In the numerical example studied in chapter III, the initial state is the ($n=3$, $\ell=2$, $m=2$) state. It is found that if the ($n=4$, $\ell=2$, $m=2$) state is removed from the basis set during the integration, then the atom is ionized nearly as predicted by Fermi's golden rule. The numerical integration seems to indicate the surprising result that recapture of population from the set of $\ell=3$ states by the ($n=4$, $\ell=2$, $m=2$) state can somehow inhibit ionization of the ($n=3$, $\ell=2$, $m=2$) state. In chapters IV and V, general theories of ATI and population trapping are developed and tested numerically.

The numerical integration of Schrodinger's equation described in chapter III reveals that recapture of population from the ionization continuum by bound states of the same parity as the initial state has the effect of inhibiting ionization of population from the initial state. The numerical integration of course cannot reveal how general the effect is, whether it is due to some special or accidental choice of initial conditions, atomic structures, and laser pulse shapes. The goal of chapter IV is to develop a theory that can explain the effect as simply as possible, but with sufficient generality to determine what role laser pulse shapes and various

atomic structures may have in the physics of the population trapping. The method employed is a generalization of the Fermi's golden rule theory developed in chapter II and as a result reduces to the FGR result in the proper limit, and handles non-rectangular laser pulse shapes. In chapter IV the theory is applied to a simple model atom rather than the full hydrogen atom investigated in chapter III. The theory proves capable of modeling the phenomenon for a variety of laser pulse shapes, and atomic structures. The simpler version of the theory employs the rotating-wave approximation (RWA), and admits analytic solutions in several special cases. The predictions of the theory in the RWA agree qualitatively with a numerical integration of the full equations of motion, but do not give complete quantitative agreement. We are able to show that the source of the failure is the RWA by developing a more sophisticated version of the theory that does not employ the RWA. The more sophisticated version gives superior agreement with the numerical integration of the full equations of motion.

In chapter V we turn to the problem of the above-threshold ionization (ATI) of atomic hydrogen. Above-threshold ionization has proved to be a challenge to atomic theorists. A number of standard techniques of atomic physics that have proved so useful in the past are poorly justified in the ATI limit. When atoms interact with ultra-intense laser fields, perturbative expansions converge slowly (if at all), and as we have mentioned, out-of-resonant atomic states at unexpected energies and angular momenta can profoundly influence the physics of atomic energy absorption. The fact that we found it necessary to use 1600 atomic states

in our numerical integration of hydrogen undergoing ATI attests to the complexity of the ATI process. A certain class of theories has met with some popularity in the search for theoretical models of ATI. These are the theories of the type first proposed by Keldysh[11,12] in 1965. Theories of the Keldysh type may be derived from scattering theory in the limit in which the Coulomb potential of the atom is treated as a perturbation to the ultra-intense laser field.

In chapter V we develop a theory of the Keldysh type appropriate for treating the femtosecond excitation of atomic hydrogen[13]. The theory is actually much more general than the various published Keldysh-like theories. It is derived in a few lines directly from the time-dependent Schrödinger equation and we describe the further approximations required to put the general theory in a time-independent *form similar to* the Keldysh-type scattering theories. This derivation proves extremely useful in correcting a serious defect associated with the theories of the Keldysh type. The Keldysh theories are not invariant under the gauge transformation in which $\Psi(r,t)$ is replaced by $\Psi(r,t)e^{i\Lambda(t)}$, whereas the Schrödinger equation is invariant under transformations of this sort. We show how to preserve the Schrödinger equation's invariance in the Keldysh-like theory presented in chapter V. The consequences of this approach are non-trivial; the equations derived in chapter V give predictions that differ by orders of magnitude from the predictions of the published Keldysh theories. In chapter V numerical evidence is given supporting the gauge-invariant theory.

The classical correspondence of one electron atoms in the absence of external fields is a problem that has been well understood since the early days of quantum mechanics. However, the problem of the classical correspondence of atoms interacting with external fields is far more difficult. The three-dimensional classical hydrogen atom in an external field is described by a non-linear system of second order differential equations that is analytically intractible. However, the problem can be adequately handled numerically with Monte Carlo techniques. In the chapters previous to chapter VI a number of interesting ionization effects were revealed in a numerical integration of the three-dimensional Schrödinger equation, among them ATI, and population trapping. In chapter VI some numerical experiments on the corresponding three-dimensional classical problem, using a Monte Carlo method, are described. To a surprising degree, many of the ionization phenomena apparent in the quantum mechanical integration seem to be present in the classical model as well.

References

1. **Letters on Wave Mechanics** (edited by K. Przibram), Philosophical Library (1967).

2. E. Schrödinger, Natürwissenschaften **28**, 664 (1926).

3. J. Parker and C. R. Stroud, Jr., Phys. Rev. Lett. **56**, 716 (1986).

4. G. Alber, H. Ritsch, and P. Zoller, Phys. Rev. A **36**, 683 (1987).

5. J. Parker and C. R. Stroud, Jr., Physica Scripta T12, 70 (1986).

6. W. A. Henle, H. Ritsch, and P. Zoller, Phys. Rev. A **36**, 683 (1987)

7. J. A. Yeazell and C. R. Stroud, Jr., Phys. Rev. A **35**, 2806 (1987).

8. J. A. Yeazell and C. R. Stroud, Jr., Phys. Rev. Lett. **60**, 1494 (1988).

9. A. ten Wolde, L. D. Noordam, H. G. Muller, A. Lagendijk and H. B. Van Linden van den Heuvell, Phys. Rev. Lett. **61**, 2099 (1988).

10. P. Agostini, F. Fabre, G. Mainfray, G. Petite, and N. Rahman, Phys. Rev. Lett. **42**, 1127 (1979).

11. L. V. Keldysh, Sov. Phys. JETP 20, 1307 (1965).

12. A. I. Nikishov and V. I. Ritus, Sov. Phys. **23**, 168 (1966); F. Faisal, J. Phys. B **6**, L312 (1973); H. R. Reiss, Phys. Rev. A 22, 1786 (1980); W. Becker, R. R. Schlicher, and M. O. Scully, J. Phys. B **19**, L-461 (1986); H. R. Reiss, J. Phys. B **20**, L-79 (1987); J. Kupersztych, Europhys. Lett. **4**, 23 (1987).

13. J. Parker and C. R. Stroud Jr., Phys. Rev. A **40**, 5651-5658 (1989).

CHAPTER II
SHORT PULSE EXCITATION OF RYDBERG WAVE PACKETS

Section 2.1 Introduction.

In this chapter we begin our study of the interaction of one-electron atoms with short coherent laser pulses. We approach the problem from a novel point of view by studying the relationship between the $\Delta r \Delta p$ uncertainty product of the excited electron and the $\Delta\omega\Delta t$ Fourier relation of the laser pulse that excites the electron. It will be shown numerically that in a certain limit a transform-limited laser pulse (satisfying $\Delta\omega\Delta t = 1/2$) may generate a nearly minimum uncertainty electron state (satisfying $\Delta r \Delta p \simeq \hbar/2$).

There is a well known theorem in quantum mechanics that the minimum uncertainty state is uniquely a Gaussian wave packet. As might be expected from the remarks above, the results of this chapter may viewed from another perspective: we will be studying a case in which Gaussian shaped laser pulses generate (nearly) Gaussian shaped electron wave packets.

Throughout this chapter it will be assumed that the laser pulses have a special property, namely that they are transform-limited. Additionally, it will be assumed that they are linearly polarized. A transform-limited Gaussian laser pulse satisfies the relation

$$\Delta\omega\Delta t = 1/2, \tag{2.1}$$

where $\Delta\omega$ is the dispersion in the power spectrum, and $c\,\Delta t$ is the width of the pulse in space in the direction of propagation. Near the atom, the corresponding linearly polarized electric field may be written

$$\mathbf{E}(x,t) = \mathbf{E}_0 f(t - x/c)\sin(\omega(t - x/c) + \phi). \qquad (2.2)$$

In Eq. (2.2), f(t) is the shape of the envelope of the electric field, x is the direction of propagation, and $\mathbf{E}_0$ is a vector giving the direction and magnitude of the electric field at the peak of the pulse. If the frequency ω is time dependent, or if ϕ is time dependent (e.g., there are sudden phase jumps in the field), then the relation (2.1) will not be satisfied. But in all cases, the Fourier relation

$$\Delta\omega\Delta t \geq 1/2, \qquad (2.3)$$

is satisfied. Henceforth, we will assume that the field is coherent, and define $\Delta\omega$ to be the width of the square modulus of the Fourier transform of the pulse shape f(t), and similarly Δt to be the width of $f^2(t)$.

The time-frequency Fourier relations of electrodynamics have a special importance in laser physics. If a Gaussian pulse fails to satisfy Eq. (2.1), then this is an indication of incoherence in the field. Another immediate consequence of Eq. (2.1), and more generally Eq. (2.3), is that an attempt to make a laser pulse shorter in time (and equivalently narrower in space) requires making the bandwidth broader according to $\Delta\omega \geqq 1/(2\Delta t)$. The equality $\Delta r = c\,\Delta t$ yields the equivalent relation, $\Delta\hbar\omega/c \geqq \hbar/(2\Delta r)$. Comparison with the quantum mechanical uncertainty relation $\Delta p \geqq \hbar/(2\Delta r)$ suggests a physical similarity. In fact, it is well known that the two relations have a similar interpretation: an attempt to make the wave packet of an electron narrower in space requires making

the momentum spectrum of the electron (and equivalently the energy spectrum) broader according to $\Delta p \geqq \hbar / (2\Delta r)$.

In the quantum mechanics of atoms, a time-energy uncertainty relation $\Delta E \Delta t \geqq \hbar/2$ cannot be rigorously formulated in constrast to the $\Delta r \Delta p \geqq \hbar/2$ uncertainty relation. In quantum mechanics, probability distributions for the space and momentum variables (r and p) are defined by the wave function $\Psi(r,t)$, but no probability distribution is defined for time. Time is not an observable in the sense that r and p are observables. For example, a dispersion Δp for momentum can be defined which predicts the results of measurements of the observable p,

$$\Delta p = \left[\int \Psi^* \left(p - \langle p \rangle \right)^2 \Psi \, d^3r \right]^{1/2}, \qquad (2.4)$$

but Δt does not have a similarly well defined physical interpretation.

Nevertheless, Δt and the $\Delta\omega\Delta t \geqq 1/2$ Fourier relation have precise meanings and important applications in classical electrodynamics and in laser physics. In this chapter a limit will be studied in which Δt does have a precise meaning in the quantum mechanics of Rydberg wave packets, and it will be shown that the Δt of the atomic state is related to the Δt of the laser pulse that generates the wave packet.

The physical system to be studied is the hydrogen atom interacting with laser pulses of duration 5 femtoseconds to 10 picoseconds. The atom is initially in a low lying bound state, and the laser is tuned so that the electron is excited to the Rydberg states - typically states of principal quantum number 20 or higher. Under these conditions the laser pulse generates an excited state with some of the special properties alluded to

above: near minimum uncertainty in r and p, quasi-classical orbital motion, and a well localized wave packet structure.

In section 2.2 Schrödinger's equation will be solved numerically under the conditions described above, and some numerical results will be discussed.

In section 2.3 we begin development of the theory in an effort to explain the numerical results as simply as possible. The emphasis will be on calculating the state of the atom at the end of the laser pulse rather than the subsequent evolution of the atom. A generalized Fermi's golden rule will be developed to describe the atom-laser interaction in the wave packet limit.

In section 2.4 we turn to a study of the spatial properties of the wave packet $\Psi(r,t)$. Using the WKB approximation and the methods of section 2.3, an approximate formula for $\Psi(r,t)$ will be derived and compared with the numerically generated $\Psi(r,t)$.

In section 2.5 uncertainty products will be discussed. The formulas of section 2.4 will be used to establish the connection between the $\Delta\omega\Delta t$ relation of the laser pulse, and the corresponding quantity of the wave packet generated by the pulse.

Section 2.2 Generation of Rydberg Wave Packets: Numerical Results

In this section the Schrödinger equation will be written down for the set of states shown in Fig. 2.1 and some numerical solutions will be described. As Fig. 2.1 shows, the hydrogen atom initially is in the bound state labeled

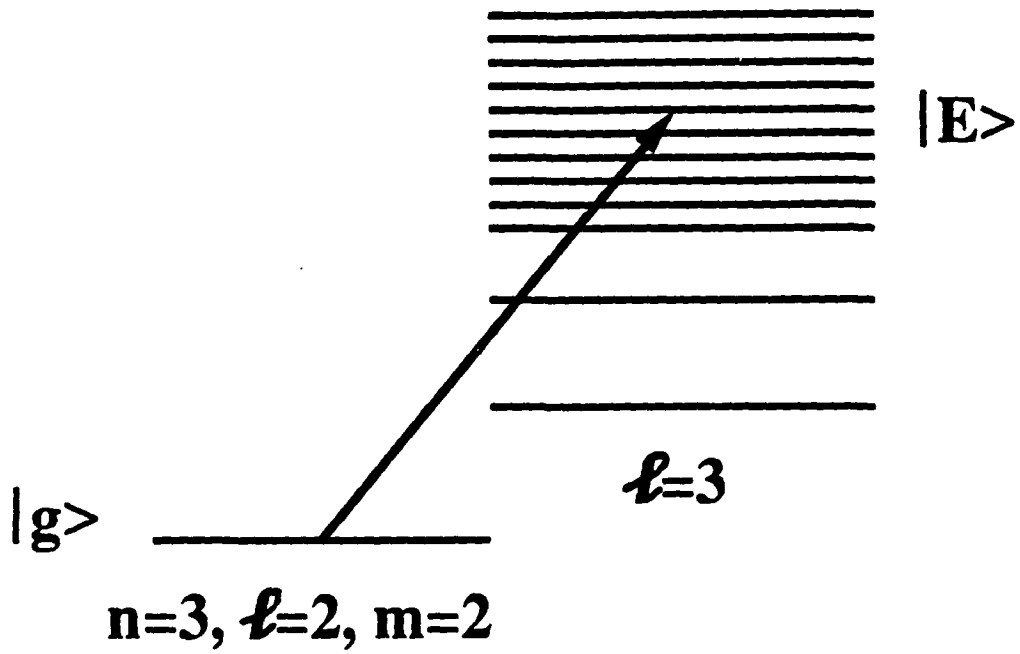

Fig. 2.1. Energy level diagram for short pulse laser excitation of Rydberg wave packets. A linearly polarized laser pulse, represented by the solid arrow, interacts with an atom initially in state $|g\rangle$ with quantum number $n=3$, $\ell=2$, $m=2$. The pulse is short enough, and its bandwidth broad enough to excite a coherent superposition of $\ell=3$ Rydberg states labeled $|E\rangle$. The states are not drawn to scale. Altogether, 150 states are used.

$|g>$ with quantum numbers ($n=3$, $\ell=2$, $m=2$). In the dipole approximation, the electron cannot make the transition to states of quantum number $\ell=1$, because the pulse is linearly polarized, so that quantum number m must remain constant. Figure 2.1 represents the resonant one photon transition from the initial state $|g>$ to the $\ell=3$, $m=2$ Rydberg states labeled $|E>$.

Two examples will be discussed. In the first example the laser will be tuned to the $n=85$ state. The pulse will be short enough (10 picoseconds) and its bandwidth broad enough that the $n=84$ and $n=86$ states will also receive substantial population during the laser excitation. It will be seen that under these conditions the state of the atom at the end of the pulse is a well localized wave packet that is narrow in comparison to the 14,400 Bohr radii extent of the $n=85$ eigenstate. The subsequent evolution of the wave packet in the absence of the laser pulse has a quasi-classical character. Although the packet spreads, its orbital period is the same orbital period as that of a classical electron with the same energy as the $n=85$ state.

In the second example the laser will be tuned to the $n=25$ state. The goal in this example will be to study the atomic state at the end of laser pulses of varying duration, from 5 femtoseconds to 300 femtoseconds. Of particular interest in this example is the $\Delta r \Delta p$ uncertainty product of the atomic state at the end of the pulse.

Schrödinger's equation, in the dipole approximation, restricted to the set of states of Fig. 2.1 is,

$$i\frac{da_E(t)}{dt} = 2V_{Eg}\, a_g(t) \exp(-i\omega_g t) \exp(i\omega_E t) \sin(\omega t) f(t) , \qquad (2.5a)$$

$$i\frac{da_g(t)}{dt} = \sum_E 2V_{Eg}\, a_E(t)\, \exp(i\omega_g t)\exp(-i\omega_E t)\sin(\omega t) f(t) \ . \qquad (2.5b)$$

In Eq. (2.5), the electric field is given by Eq. (2.2) and $2\hbar V_{Eg}\sin(\omega t)f(t)$ is the matrix element of the interaction Hamiltonian ($<E \mid \mathbf{d}\cdot\mathbf{E}(t) \mid g>$) connecting the states $|E>$ and $|g>$. The energy of the state $|E>$ is $\hbar\omega_E$, the energy of the state $|g>$ is $\hbar\omega_g$, and $\hbar\omega$ is the photon energy. Here the pulse envelope function, f(t), is normalized to unity at its maximum. The variables a(t) are the probability amplitudes of the states in the interaction picture.

Equation 2.5 is solved numerically, and then the wave function $\psi(r,t)$ is calculated from

$$\Psi(r,t) = \sum_E a_E(t)\ \exp(-i\omega_E t)\, u_E(r) \ . \qquad (2.6)$$

where the sum is over all of the Rydberg states $|E>$ used in the numerical integration of Eq. (2.5). The eigenfunctions $u_E(r)$ are in the radial variable $r = |\mathbf{r}|$, and are calculated for each principal quantum number n by numerically integrating the time-independent Schrödinger equation with the energy eigenvalue set to $E = -\hbar\omega_R/n^2$. Here $\hbar\omega_R$ is the Rydberg energy, 13.6 eV. The method of numerical integration will be described in the next chapter.

Let us return to the first numerical example. The coherent laser pulse excites principally the n=84, 85, and 86 states. The state of the atom at the end of the pulse is a localized wave packet, shown in Fig. 2.2, labeled 15. The quantity plotted is $r^2\Psi^*\Psi$ and the label is the number of picoseconds that have elapsed from the time at which the center of the laser pulse

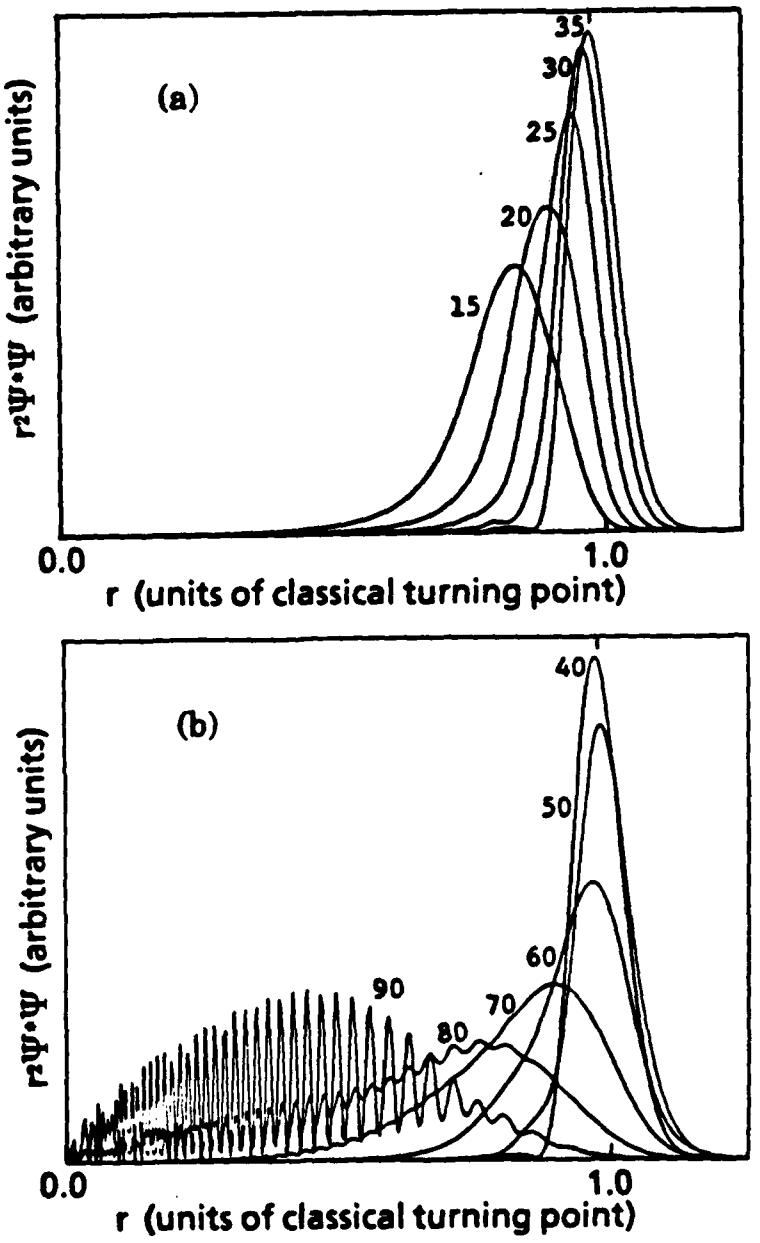

Fig. 2.2. A Rydberg wave packet at various times after creation. Each curve is labeled by the time that has elapsed, in picoseconds, from the time that the center of the laser pulse reached the atom. A 10 picosecond (FWHM) laser pulse was used to excite Rydberg states in the vicinity of n=85. The wave packet travels to the classical turning point, is reflected, and returns to the core of the atom in about 93 picoseconds, which is the orbital of period a classical electron corresponding to the n=85 state.

reached the atom. The subsequent evolution of the wave packet during its first orbit of the atom is also shown in Fig. 2.2. The wave packet travels away from the core, out to about 14,400 Bohr radii, the outer turning point of the n=85 state. This is also the outer turning point of a classical electron with energy equal to that of the n=85 state. The wave packet begins its return to the core of the atom at about 50 picoseconds. The wave packet reaches its closest approach to the core of the atom at 93 picoseconds, which is just the orbital period of a classical electron with energy equal to that of the n=85 state. The subsequent evolution of the state is not shown, but the orbital cycle repeats itself three times, with an orbital period of 93 picoseconds, before the spreading of the wave packet obscures the quasi-classical orbital motion evident in Fig. 2.2.

Figure 2.3 shows the $\Delta r \Delta p_r$ uncertainty product of the atomic state shown in Fig. 2.2. Here r is again the radial variable $r = |\mathbf{r}|$. It should be noted that the wave packet is localized only in r. Its angular distribution is given by the spherical harmonic $Y_{lm}(\theta,\phi)$ where $\ell=3$, and $m=2$. The variable p_r is the radial momentum defined (in the absence of external fields) by m(dr/dt), where m is the mass of the electron. The two variables satisfy $[r, p_r] = i\hbar$. The Heisenberg uncertainty principle states then that under certain special circumstances $\Delta r \Delta p_r$ may equal $\hbar/2$, but it may never be less than $\hbar/2$. In Fig. 2.3 the minimum of $\Delta r \Delta p_r$ is $.5002\hbar$, which occurs at about 25 picoseconds, suggesting that the Gaussian laser pulse generated a (nearly) Gaussian electron wave packet. The rapid spreading of the wave packet in r is evidently the reason $\Delta r \Delta p_r$ never again approaches $\hbar/2$.

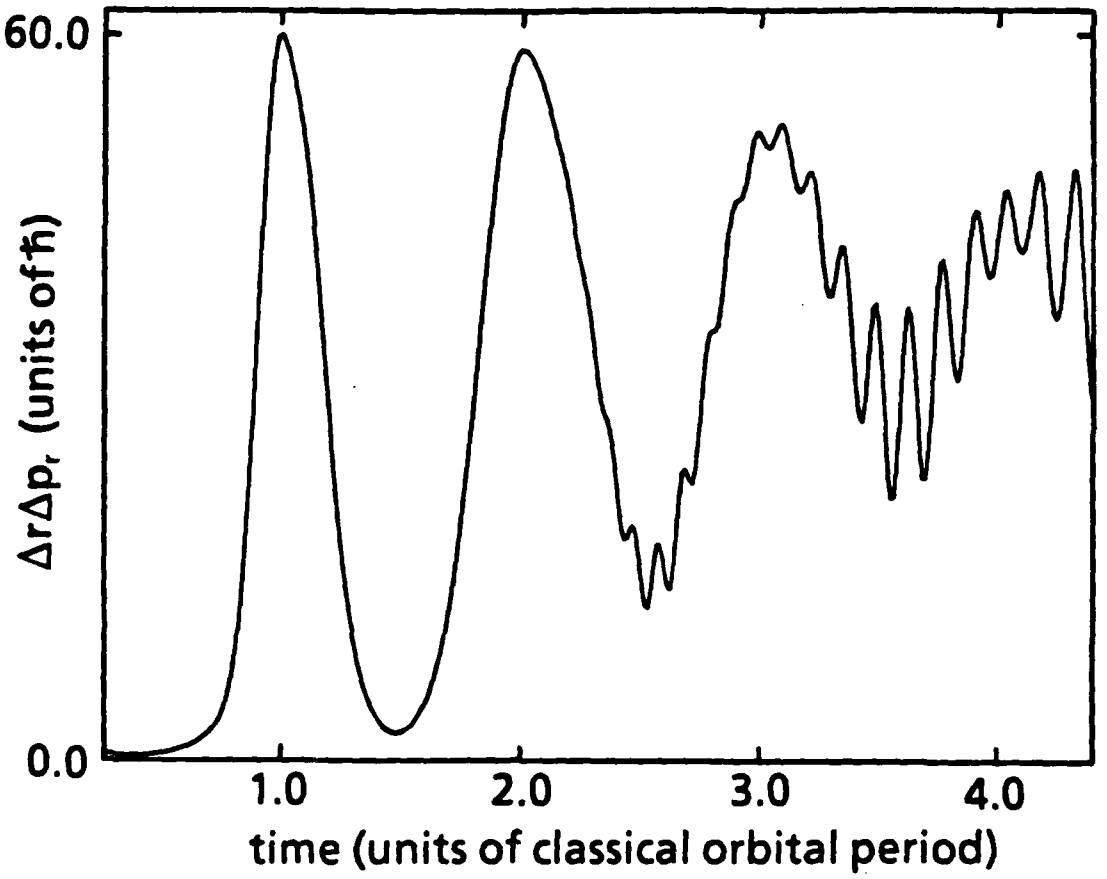

Fig. 2.3. The uncertainty product $\Delta r \Delta p_r$ of an orbiting Rydberg wave packet. The packet is as described in Fig. 2.2. It has an orbital period of 93 picoseconds, and an energy equal to that of the n=85 Rydberg state. The minimum uncertainty of .5002$\hbar$ ocurrs at about 25 picoseconds. As the packet spreads in r and returns to core of the atom, the uncertainty product increases by over two orders of magnitude. As the packet returns to the outer turning point (apogee), and narrows up, the uncertainty product falls to about 4$\hbar$, but does not return to its minumum value.

From the structure of the recurrences in Fig. 2.3 and from the discussion of Fig. 2.2, it appears that the wave packet corresponds to a classical electron that was at perigee (closest approach to the nucleus) at $t=0$, where t is such that the laser pulse peaks in intensity at $t=0$. One of the reasons we make this point is that it provides a physical explanation for the observation that a sufficiently short laser pulse generates a localized wave packet. The laser pulse used in the example described above was about 1/9th of the 93 picosecond orbital period of the classical electron associated with the $n=85$ state. Consequently the electron did not have time to travel to the outer turning point (apogee) of the orbit during the 10 picosecond pulse. The condition for a wave packet, then, is that the length of the laser pulse τ should be short in comparison to the orbital period of the excited state: $\tau << n n^3/\omega_0$. This inequality can be rewritten $2\pi/\tau >> 2\omega_0 / n^3$. This is also the condition that the laser pulse has sufficiently broad bandwidth to excite not just the resonant state (in this case $n=85$) but also neighboring eigenstates. The reason for this is that $2\omega_0/n^3$ is just the frequency separation of adjacent Rydberg states, and the bandwidth of the laser pulse goes as $2\pi/\tau$.

Now we begin discussion of the second example. In this example the laser is tuned to excite the $n=25$ state, and the pulse length is varied from 300 femtoseconds, down to 5 femtoseconds. The classical orbital period corresponding to $n=25$ is 2.37 picoseconds.

In this example we are interested in the state of the atom at the end of the pulse rather than its subsequent motion. In Fig. 2.4 is shown the wave packet $r^2\Psi^*\Psi(r)$ as it appears immediately after the the end of the pulse

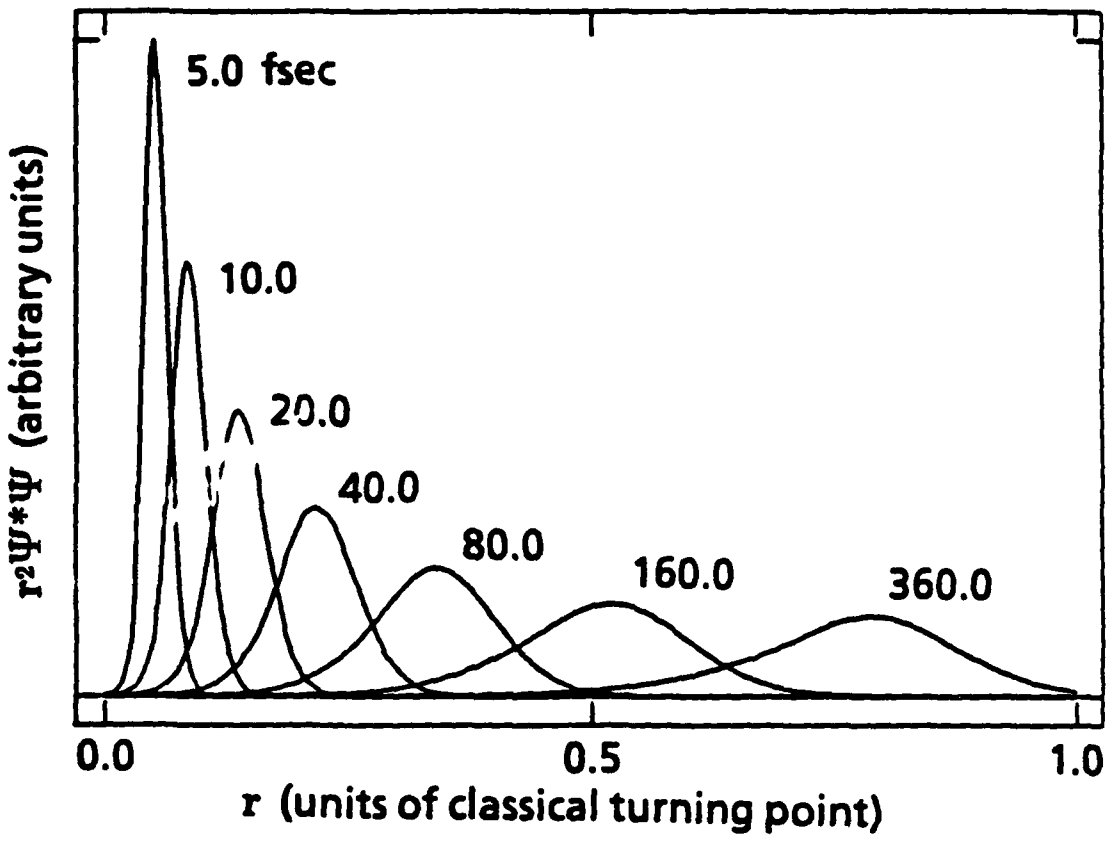

Fig. 2.4. Rydberg wavepackets generated by laser pulses of various lengths. Here the packets are labeled by the pulse lengths (FWHM intensity) in femtoseconds. The laser excites Rydberg states in the vicinity of $n = 25$. The packets are as they appear when the pulse has fallen to 0.4% of its peak amplitude.

for various pulse durations . The wave packets are labeled by the length of the laser pulse (in femtoseconds) that generated the wave packet. The amplitude of the field is adjusted so that the total pulse energy of the field is the same in each case. The pulse intensity is in each case the intensity required to pump 10% of the population into the Rydberg states. The spatial axis in Fig. 2.4 is labeled in units of the classical turning point of an electron with energy equal to that of the state n = 25, and with angular momentum $\hbar$. This turning point, or apogee, is given by approximately $2n^2a_0$, where a_0 is the Bohr radius.

Figure 2.5 shows the $\Delta r \Delta p_r$ uncertainty product of Rydberg wave packets of the sort shown in Fig. 2.4. The pulse length varies from 5 to 300 femtoseconds. The wave packets are near minimum uncertainty, although not within three significant figures of $0.5\hbar$ as in the n=85 case described above.

Section 2.3 Analysis of the Equations of Motion

The numerical examples and simple physical arguments of the previous section provided a definite range of parameters for which well localized Rydberg wave packets are formed. The actual working out in detail of the shape and evolution of the wave packet is made difficult, however, by the infinite sum over Rydberg states which occurs in Eq. (2.5). In this section and the next we will work out analytic approximation techniques which greatly simplify this problem.

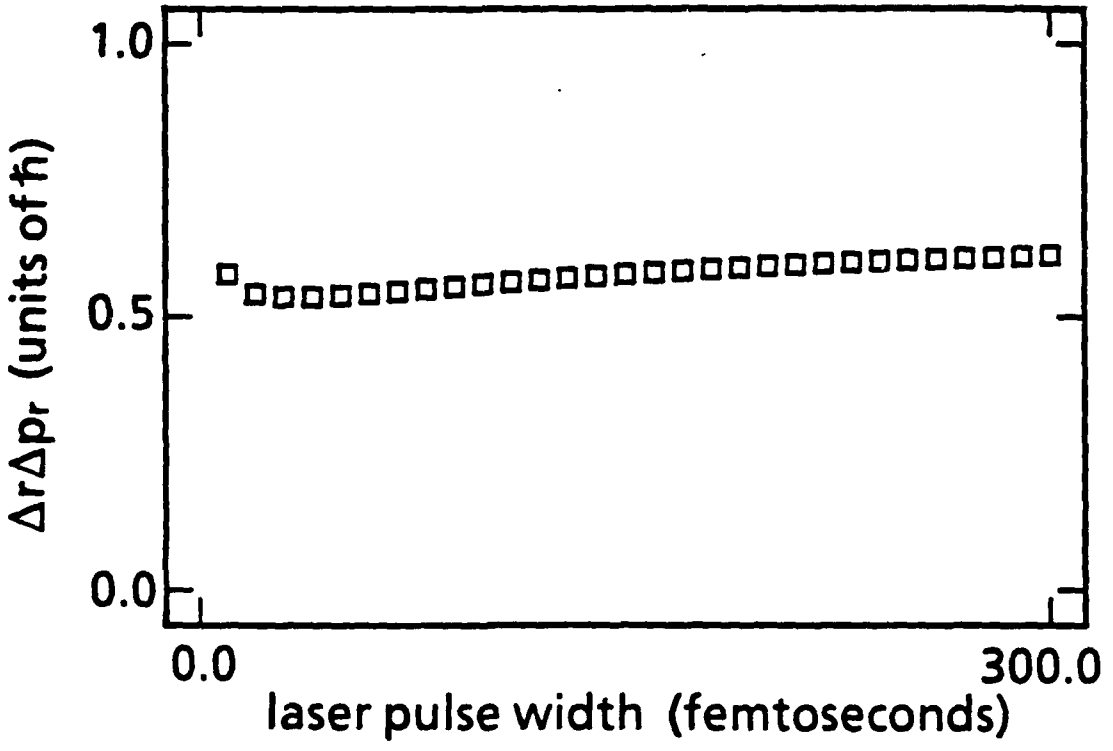

Fig. 2.5. The $\Delta r \Delta p_r$ uncertainty product of Rydberg wave packets at the end of laser pulses of various lengths. The laser pulses vary in length from 5 femtoseconds to 300 femtoseconds, and the laser is tuned to the n=25 Rydberg state, as in Fig. 2.4. The uncertainty product is calculated when the pulse has fallen to 0.4% of its peak amplitude. The uncertainty products (labeled by boxes in the figure) vary from $0.53\hbar$ to $0.60\hbar$.

In the previous section the numerical examples suggested that the limit in which wave packets are generated is the limit in which the bandwidth of the laser pulse is broad enough to excite more than one Rydberg state. This is also the limit in which a Fermi golden rule analysis is the appropriate description of the excitation. The main result of this section will be a straightforward derivation of a generalized Fermi's golden rule (FGR). We will also compare the frequency dispersion of the laser pulse $\Delta\omega$ with the frequency dispersion of the wave packets generated by the pulses $\Delta H/\hbar$. Here H is the atomic Hamiltonian, which at the end of the laser pulse is the energy of the atomic state. As will be seen, the energy uncertainty $\Delta H/\hbar$ of the Rydberg wave packets closely matches the $\Delta\omega$ of the laser pulse that generated it.

We are interested in the state of the atom just at the end of the pulse, as in Fig. 2.4. Although the equations below generalize without difficulty to arbitrary times, assume below that the field has died away at time t. To begin, the rotating-wave approximation is made on Eq. (2.5) by expanding the sine function in complex exponentials, and discarding the rapidly varying terms. With this simplification Eq. (2.5) becomes

$$i\frac{da_E(t)}{dt} = V_{Eg}\, a_g(t)\, f(t) \exp\left\{ i[\omega - (\omega_E - \omega_g)]\, t \right\}, \tag{2.7a}$$

$$i\frac{da_g(t)}{dt} = \sum_E V_{Eg}\, a_E(t)\, f(t) \exp\left\{ -i[\omega - (\omega_E - \omega_g)]\, t \right\}. \tag{2.7b}$$

Equation (2.7) can now be formally integrated in time to yield the amplitude of the excited Rydberg state of energy E at the end of the pulse:

$$a_E(t) = -iV_{Eg}\, F(\Delta_E) + a_E(-\infty) \tag{2.8}$$

where Δ_E is the detuning $\omega_E - \omega_g - \omega$ and $F(\Delta_E)$ is the Fourier transform of $f(t)a_g(t)$:

$$F(\Delta) = \int_{-\infty}^{\infty} dt \, \exp(i \Delta t) a_g(t) \, f(t) \, , \tag{2.9}$$

The upper limit of the integral of Eq. (2.9) is more precisely the time t of Eq. (2.7), but it is assumed that at time t the laser pulse has died away sufficiently that Eq. (2.9) is a good approximation. We turn now to a discussion of Fermi's golden rule by calculating the population in the excited state at the end of the pulse. The population in the excited state is just the sum over Rydberg states of the absolute values of the amplitudes of the states of energy E:

$$\sum_E |a_E(t)|^2 = \sum_E |V_{Eg}|^2 \, |F(\Delta_E)|^2. \tag{2.10}$$

This sum over Rydberg states $|E>$ can be formally rewritten as an integral over $dE\, \rho(E)$:

$$\sum_E |a_E(t)|^2 = \int dE \, R(E) \, |F(\omega_E - \omega_g - \omega)|^2 / (2\pi\hbar) \tag{2.11}$$

where R(E) is the FGR transition rate from the state $|g>$ to the Rydberg states centered about state $|E>$,

$$R(E) = 2\pi\hbar \, |V_{Eg}|^2 \rho(E) \tag{2.12}$$

and the density of states $\rho(E)$ is just the inverse of the energy separation of the Rydberg states adjacent $|E>$. Thus $\rho(E)\, \delta E$ is the number of Rydberg states in the energy interval δE.

The rate R(E) is the standard text book formula for the FGR rate. To show the connection between Eq. (2.11) and the usual FGR prediction of the population in the excited states at the end of the pulse, two more approximations are necessary. First it is assumed that the Fourier

transform $|F(\omega_E - \omega_g - \omega)|^2$ is a function that is sharply peaked at the energy of the resonant Rydberg state $E=\hbar(\omega+\omega_g)$, and consequently behaves like a δ-function. In these equations ω is the laser frequency and ω_E is the atomic state energy divided by $\hbar$: $E/\hbar$. Second, it is assumed that the population in the initial state is constant during the pulse: $a_g(t) = 1$. These are the standard approximations in FGR calculations. With these assumptions, Eq. (2.11) becomes:

$$\int dE\ R(E)\,|F(\omega_E - \omega_g - \omega)|^2/(2\pi\hbar) = R(\hbar(\omega+\omega_g))\int \frac{dE}{\hbar}\,|F(\omega_E - \omega_g - \omega)|^2/2\pi$$

$$= R(\hbar(\omega+\omega_g))\int dt\ |f(t)|^2 \qquad (2.13)$$

The last equality required Parseval's Theorem. In the next chapter we will show how to calculate the time evolution of $a_g(t)$ and will present a more thorough discussion of the equations of motion. In this section, the goal has been to introduce equations that are useful in studying the relationship between Δω of the laser pulse and $\Delta H/\hbar$ of the atomic state at the end of the pulse.

With this preparation, the relationship between Δω and $\Delta H/\hbar$ of the atomic state at the end of the pulse can be discussed. The frequency dispersion of the laser pulse is

$$\Delta\omega = \left[\frac{\int d\omega\,(\omega - \langle\omega\rangle)^2\,|G(\omega)|^2}{\int d\omega\ |G(\omega)|^2}\right]^{1/2}, \qquad (2.14)$$

where $G(\omega)$ is the Fourier transform of the laser pulse $f(t)\exp(-i\omega t)$.

The dispersion in energy of the atomic state is

$$\Delta H = \left[\frac{\int d^3r\ \Psi^*\,(H - \langle H\rangle)^2\,\Psi}{\int d^3r\ \Psi^*\,\Psi}\right]^{1/2}, \qquad (2.15)$$

where Ψ is the Rydberg state vector, which can be rewritten

$$\Delta H = \left[\frac{\sum_E |a_E(t)|^2 (E - \langle E \rangle)^2}{\sum_E |a_E(t)|^2} \right]^{1/2} . \qquad (2.16)$$

In the limit in which the FGR formulation of Eq. (2.11) is valid, this may be rewritten as an integral

$$\Delta H = \left[\frac{\int dE \ (E - \langle E \rangle)^2 \ R(E) \ |F(\omega_E - \omega_g - \omega)|^2}{\int dE \ R(E) \ |F(\omega_E - \omega_g - \omega)|^2} \right]^{1/2} . \qquad (2.17)$$

In order to make the comparison between Eq. (2.14) and Eq. (2.17) notice first that the functions F and G are identical (in width) in the limit in which the ground state amplitude $a_g(t)$ remains near one, (the weak field limit). In all of the numerical examples discussed in this chapter, the field is chosen sufficiently weak that $a_g(t)$ remains within 10% of one. Assuming the weak field limit, comparison of the $\Delta\omega$ of Eq. (2.14) with the $\Delta H/\hbar$ of Eq. (2.17) shows that the two are identical in the limit in which R(E) is constant in E (so that it can be moved outside the integral), or in the limit in which the spectrum $|F|^2$ of the pulse is well localized in E (for the same reason). In the examples discussed here, the latter condition is true to good approximation, and was in fact the same condition used to derive the FGR formulation of Eq. (2.13). Thus $\Delta\omega$ and $\Delta H/\hbar$ should be equal in the limit in which the FGR formulation of Eq. (2.13) is valid.

Let us test how well the $\Delta H/\hbar$ of the atomic state agrees with the $\Delta\omega$ of the laser pulse by calculating $\Delta H/\hbar$ for the example of Fig. 2.4. Figure 2.6 shows the results of such a comparison. The quantity plotted is $\Delta H/\hbar$, multiplied in each case by Δt of the laser pulse. In the plot, ΔH is labelled ΔE to emphasize that the Hamiltonian gives the energy of the atomic

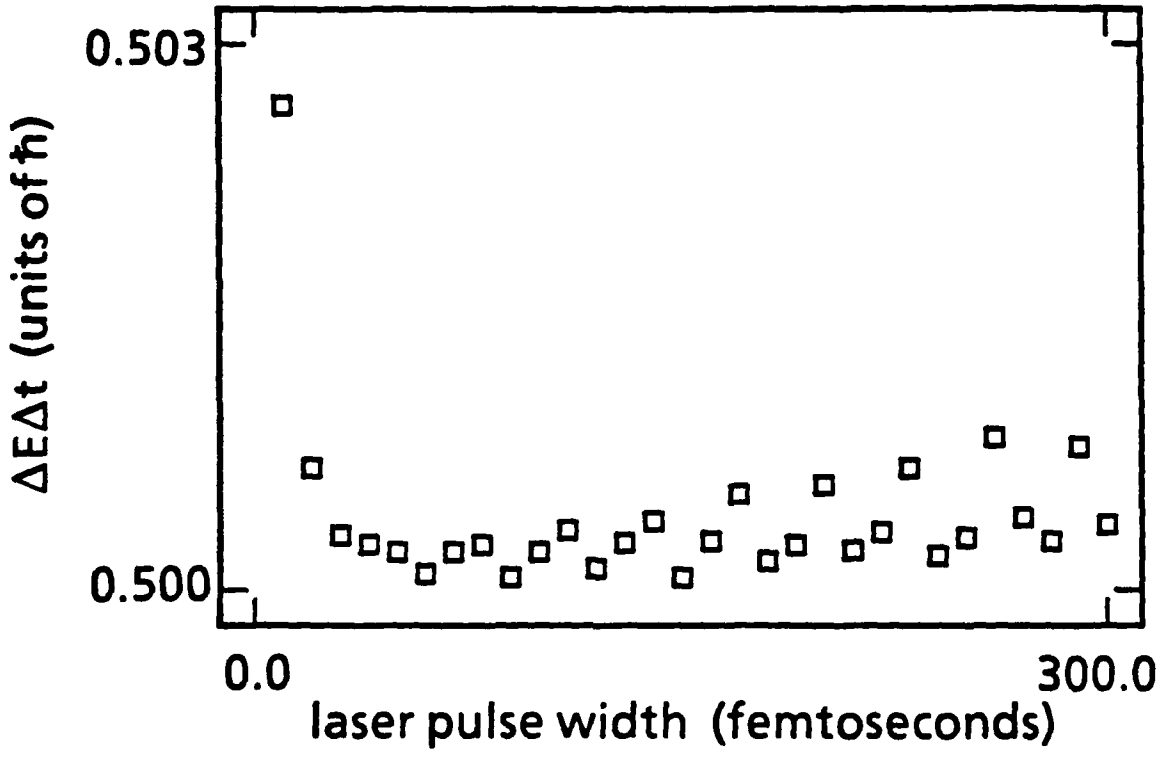

Fig. 2.6. The uncertainty in energy $\Delta E/\hbar$ of Rydberg wave packets generated by laser pulses of various length. The example is the same as described in Fig. 2.5. The ΔE of each Rydberg wave packet is multiplied by the Δt of the laser pulse that generated the packet in order to make the data easier to read. Gaussian laser pulses were used so that $\Delta\omega\Delta t$ of the laser pulse is 0.5 in each case shown above. Figure 2.6 shows, then, that $\Delta E/\hbar$ of the wave packet agrees with $\Delta\omega$ of the laser pulse to two significant figures.

states at the end of the pulse. In all but one case, $\Delta E/\hbar$, multiplied by the laser pulse's Δt, is within three significant figures of the laser pulse's $\Delta\omega\Delta t$ (which equals .5), confirming in this example that the approximations that lead to Eq. (2.13) and Eq. (2.17) are justified.

Section 2.4 WKB Analysis of the Wave Packet

In this section approximate analytic expressions for the shape of the wave packet at the end of the laser pulse will be developed. Here we will see that the methods of the previous section greatly simplify the sum over the rapidly oscillating radial wave functions, provided the WKB approximation is used to represent the radial wave functions. The wave function to be calculated is:

$$\Psi(r,t) = \sum_E a_E(t)\, u_E(r)\, \exp(-iE\,t/\hbar)\,. \tag{2.18}$$

The WKB method gives a good approximation of the wave function except near the turning points. In fact a numerical comparison of the $n=25$ WKB wave function with the exact Laguerre polynomial radial wave function reveals agreement between the two functions to three or more significant figures except near the classical turning points. We would expect then the WKB wave functions to describe the states shown in Fig. 2.1, except in the limit in which the wave packet nears the classical turning points of the $n=25$ state.

The WKB eigenfunction[1] is

$$r\,u_E(r) = k_E^{-1/2}(r)\left[\frac{1}{E_R\rho(E)\,n\,a_0^2}\right]^{1/2}\cos\left[\int_{r_0}^{r} k_E(r')\,dr' - n/4\right], \tag{2.19}$$

where

$$k_E(r) = \left[\frac{2m}{\hbar^2} (E - V(r)) \right]^{1/2} \qquad (2.20)$$

is $1/\hbar$ times the classical momentum of the electron, and V(r) is the effective potential. The quantity a_0 is the Bohr radius, $\rho(E)$ is the density of Rydberg states, E_R is the Rydberg energy, and r_0 is the inner turning point of the orbit (perigee).

The WKB wave functions can be used in Eq. (2.18) provided the sum over states $|E>$ is approximated by an integral just as was done in the previous section. Also, $k_E(r)$ will be approximated by its value at the resonant energy $E_0 = \hbar(\omega + \omega_g)$. The new function will be called $k_0(r)$. From now on the resonant energy $\hbar(\omega + \omega_g)$ will be written E_0. Next, in order to sum Eq. (2.18), an expression for $a_E(t)$ is needed. It will be useful to write $a_E(t)$ in terms of R(E) and $\rho(E)$. Equation (2.12) and Eq. (2.8) yield

$$a_E(t) = -iF(\omega_E - \omega_g - \omega) \left[\frac{R(E)}{2\pi\hbar\rho(E)} \right]^{1/2} \qquad (2.21)$$

The next step is to rewrite the sum over discrete states in Eq. (2.18) as an integral over $dE\rho(E)$, exactly as was done in the derivation of FGR in the previous section. Surprisingly, the density of states function $\rho(E)$ completely drops out of the problem. The time-dependent wave function, then, is

$$r\Psi(r,t) = (8na_0^2)^{-1/2} k_0^{-1/2}(r) \int \frac{dE}{\hbar} \left[\frac{\hbar R(E)}{E_R} \right]^{1/2} F(\Delta) \exp\left[i \int_{r_0}^{r} k_E(r')\,dr' - i\omega_E t \right] \qquad (2.22)$$

In deriving this expression an unimportant time-dependent phase factor has been dropped. The sine of the WKB wave function has been

broken into two exp functions, and only the term that results in a physical wave packet has been kept.

The rest of this section will be devoted to finding an approximate method of summing Eq. (2.22). The algebra is greatly simplified in a more natural system of units. Henceforth, the r will stand for r/a_0. Similarly E will stand for E/E_R, and ω will stand for $\hbar\omega/E_R$. The units for k(r) will be $1/a_0$, and the units of time $\hbar/E_R$. In this system of units, $k_E(r)$ is written very simply: $(E-V(r))^{1/2}$.

One more approximation is required to integrate Eq. (2.22). The exponent in Eq. (2.22) will be expanded to second order in a Taylor's series about the energy of the resonant Rydberg state E_0.

$$\Phi_1(r) = \frac{d}{dE}\int_{r_0}^{r} dr'\, k_E(r') \Big|_{E=E_0} \tag{2.23a}$$

$$\Phi_2(r) = \frac{1}{2!}\frac{d^2}{dE^2}\int_{r_0}^{r} dr'\, k_E(r') \Big|_{E=E_0} \tag{2.23b}$$

$$\int_{r_0}^{r} dr'\, k_E(r') \approx \int_{r_0}^{r} dr'\, k_{E_0}(r') + \Phi_1(r)(E-E_0) + \Phi_2(r)\,(E-E_0)^2 \tag{2.23c}$$

The quantity $\Phi_1(r)$ has an important physical interpretation. It is the time required for a classical particle of energy E_0 propagating freely in the Coulomb potential to travel from r_0 to r. For small $(E-E_0)$, the quantity $\Phi_2(r)(E-E_0)2$ is the difference in time that it takes two classical particles (of energy E and E_0 respectively) to travel from r_0 to r. As one might guess from the classical interpretation of $\Phi_2(r)$, $\Phi_2(r)$ governs spreading of the wave packet; if $\Phi_2(r)$ and all higher order terms of the Taylor's series is are

set to zero then the WKB wave packet will not spread as it propagates. If just the zeroth order and first order terms of the Taylor's series (2.23c) are kept then the wave function (2.22) can be summed for arbitrary laser pulse shape. If all three terms of Eq. (2.23c) are retained, then the wave function (2.22) can be summed for Gaussian pulse shapes under certain conditions. In what follows, the third term of Eq. (2.23c) will be discarded, and the WKB results will be compared with the numerically generated wave packets. Subsequently, the third term of Eq. (2.23c) will be kept in order to study spreading of the wave packet, and then the comparison will be repeated.

It is of historical interest that Van Vleck[2] in 1928 first noticed that the term $\Phi_1(r)$ in the Taylor's expansion Eq. (2.23) may be used to give a classical interpretation to the stationary WKB eigenstates.

With these assumptions, neglecting for the moment $\Phi_2(r)$ of Eq. (2.23c), Ψ is just the Fourier transform of a product of functions. Applying the convolution theorem, and neglecting an unimportant phase factor yields:

$$r\Psi(r,t) = (8\pi^2 k_0)^{-1/2} S(t-\Phi) * \left[f(t-\Phi)\, a_g(t-\Phi) \right] , \qquad (2.24)$$

where the * denotes convolution, and S is propotional to the Fourier transform of $R^{1/2}$

$$S(t) = 2\pi \int_{-\infty}^{\infty} dE\, R^{1/2}(E)\, \exp(-iEt) \ . \qquad (2.25)$$

This formula is consistent with the generalized Fermi golden rule formula of Eq. (2.11). It is straightforward to show that an integration over r of $|r\Psi|^2$ yields exactly Eq. (2.11) for the population in the wave packet at the end of the pulse. Equation (2.23) implies that $k_0(r)^{-1}dr = 2d\Phi$,

so that integrating Eq. (2.24) yields, :

$$\int dr\, |\, r\Psi(r,t)|^2 = \frac{1}{4\pi^2} \int d\Phi\, |\, S(t-\Phi)^*[\, f(t-\Phi)\, a_g(t-\Phi)\,]|^2 \quad . \quad (2.26)$$

Now an application of Parseval's theorem yields Eq. (2.11). The assumption is made that the wave functions are well localized wave packets as in Fig. 2.4, so that the integrations in Eq. (2.26) are over the extent of the packets and therefore avoid the turning points of the potential.

Now that it has been verified that the WKB method predicts the correct population in the wave packet at the end of the pulse, the discussion can be simplified by leaving out normalization constants. The next step will be to simplify Eq. (2.26) by applying the same approximation that led the FGR of the previous section.

In the previous section it was shown that the standard FGR formula results from the more general fromula Eq. (2.11) if it assumed that the rate R(E) is effectively constant in E wherever $F(\Delta_E)$ is significant, and if then R(E) is taken out of the integral. The numerical results presented in the previous section helped to support this approximation. In Eq. (2.24) the approximation that leads to the standard FGR, the assumption that R(E) is effectively constant, implies that S is a δ-function, leading to a very simple formula for the wave packet. An equivalent and simpler derivation is to assume R(E) is constant, and take it out of the integral of Eq. (2.22), yielding:

$$r\Psi(r,t) \propto \quad f(t-\Phi_1)\, a_g(t-\Phi_1)\, k_0^{-1/2} \qquad (2.27)$$

Eq. (2.27) is the principal result of this chapter. It predicts that the peak of the wave packet travels in the radial variable r just as a classical particle

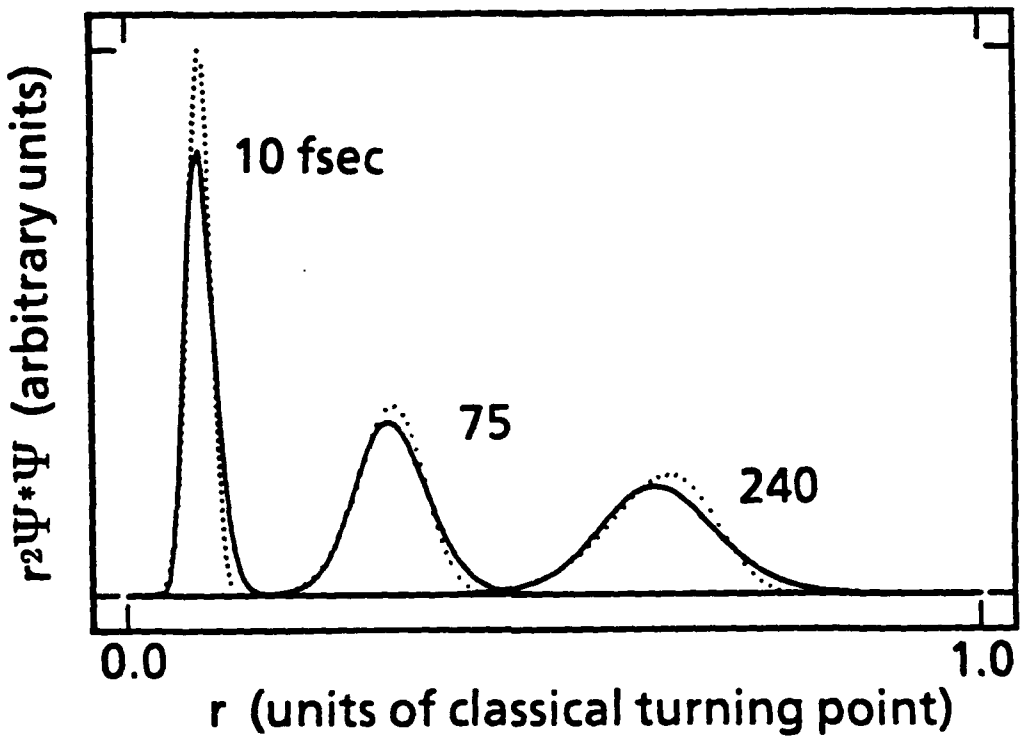

Fig. 2.7. Comparison of three Rydberg wavepackets generated by numerically integrating Schrödinger's equation (solid line) with the WKB predictions of Eq. (2.27), (dotted line). The laser is tuned to the n=25 Rydberg state, and the packets are labeled by the FWHM laser pulse width (in femtoseconds).

of energy E_0 travels. To see why this should be true, recall $\Phi_1(r)$ is the time it takes a classical particle of energy E_0 to travel from r_0 to r. Figure 2.7 compares the numerically generated wave packets with predictions of Eq. (2.27). The formula Eq. (2.27) agrees qualitatively with numerically generated results, but the numerically generated wave packets are broader in width, and hence have peak heights less than that of the WKB wave packets.

A long series of approximation was employed in the derivation Eq. (2.27). In order to learn if there is any limit in which Eq. (2.27) is valid, is important to know which of the approximations are the cause of the discrepency between the predictions of Eq. (2.27) and the numerically generated wave packets. We will show next that most of the discrepency between the theory and the numerical results is due to the neglect of the spreading term $\Phi_2(r)$. Furthermore, it will be found that if the laser is tuned to $n=85$ instead of $n=25$, then spreading is negligible, and the neglect of $\Phi_2(r)$ is a good approximation.

The third term of the Taylor's series, Eq. (2.23c), can be retained provided the laser pulse shape f(t) is Gaussian in shape, and provided that most of the population remains in the initial state during the pulse so that $a_g(t)$ remains approximately equal to one. In all of the numerical examples of this chapter, the laser pulse shape f(t) is the Gaussian $\exp(-t^2/w)$. Assuming, as we have throughout this chapter that the field is sufficiently weak that $a_g(t)=1$, the Fourier transform of f(t), neglecting some normalization constants, is $F(\Delta_E) = \exp(-w\Delta_E^2/4)$. With this choice of F, and with the full second order Taylor's series of Eq. (2.23c), Eq.(2.22) for

the wave packet becomes

$$r\Psi(r,t) \propto k_0^{-1/2}(r) \int d\Delta E \exp\left[i(\Phi_1(r) - t)\Delta E \right] \exp\left[-(w/4 - i\,\Phi_2(r))\Delta E^2 \right] \quad (2.28)$$

In Eq. (2.28) normalization constants have been neglected, as well as an unimportant overall phase factor. Also, the system of units is the system described above, so that $dE = d\omega = d\Delta E = d(E - E_0)$. The integral Eq. (2.28) can be looked up in textbooks[3]. The result is

$$r\Psi(r,t) \propto k_0^{-1/2}(r) \left[\frac{1}{w/4 - i\Phi_2(r)} \right]^{1/2} \exp\left[-\frac{(t-\Phi_1(r))^2}{4(w/4 - i\Phi_2(r))} \right]. \quad (2.29)$$

Figure 2.8 compares the predictions of the new WKB wave packet formula with the numerically generated wave packet for a variety of pulse lengths. The agreement is still not quantitative. For example the wave packets have a slightly different skew. However, most of the discrepency between the theory and the numerically generated results apparent in Fig. 2.7 is now gone.

There is a limit in which spreading is negligible and Eq. (2.27) is valid at the end of the pulse. Brown[4] has shown that the rate of spreading of Rydberg wave packets goes as $1/n^4$ where n is the principal quantum number of the resonant Rydberg state. Consequently, one expects the limit of high n to be the regime in which Eq. (2.27) is valid. This is supported by a study of Rydberg wave packets generated by a laser tuned to n=85. At n=85, a comparison of the predictions of Eq. (2.27) for the WKB wave packet without spreading and the predictions of Eq. (2.29) for the WKB wave packet with spreading shows that the two wave packets are virtually identical.

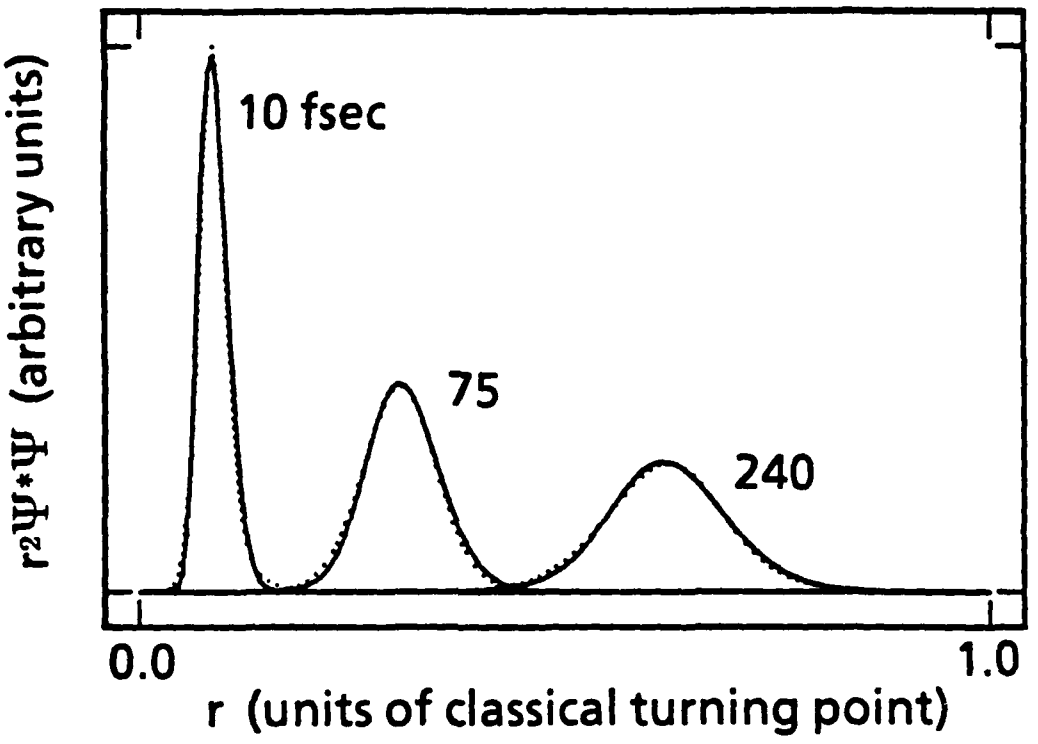

Fig. 2.8. Comparison of three Rydberg wavepackets generated by numerically integrating Schrödinger's equation (solid line) with the WKB predictions of Eq. (2.29), (dotted line). The laser is tuned to the n=25 Rydberg state, and the packets are labeled by the FWHM laser pulse width (in femtoseconds).

The agreement between the numerically generated wave packets, and the WKB predictions is about the same as shown in Fig. 2.8.

Section 2.5 Uncertainty Products

The principal result of this chapter is Eq. (2.27), a formula for the WKB wave packet in terms of the envelope f(t) of the laser pulse that generated the wave packet. In the previous section we described the limit in which Eq. (2.27) gives semi-quantitative agreement with a numerical integration of Schrödinger's equation, and we described some of the limits in which Eq. (2.27) fails. In the limit in which Eq. (2.27) is valid, and in the limit in which $a_g(t)$ is nearly constant, (the weak-field limit), a calculation of the standard deviation in the time variable Δt of the WKB $|r\Psi|^2$ (of Eq. (2.27)) yields just the Δt of the laser pulse that generated the wave packet. In Section 2.3 it was argued and verified numerically, that the $\Delta H/\hbar$ of the wave packet and the $\Delta\omega$ should agree closely in the limit in which short pulses generate wave packets. Consequently the derivation implies that, in the weak field limit for sufficiently high n, the $\Delta t \Delta H/\hbar$ product of the WKB wave packet should closely agree with the $\Delta t\ \Delta\omega$ product of the laser pulse.

The derivation does not imply that $\Delta r \Delta p_r$ of the wave packet equals $\Delta t \Delta H$ of the wave packet. There is an argument given in elementary textbooks that there should be a rough agreement between the $\Delta r \Delta p_r$ of the wave packet and $\Delta t \Delta H$, but the argument assumes that the wave packet is free space. Numerically, though, there was found a fair

agreement between the $\Delta r\Delta p_r$ of the wave packet and the $\Delta t\Delta\omega$ of the laser pulse. In fact in the high Rydberg limit (n=85) $\Delta r\Delta p_r$ was $\hbar/2$ to three significant figures. In the example in which the laser was tuned to n=25, the $\Delta r\Delta p_r$ uncertainty was typically between $0.53\hbar$ and $0.60\hbar$.

Section 2.6 Conclusion

In this chapter a number of numerical experiments were conducted in which short laser pulses excited localized wave packets among Rydberg states. The wave packets exhibited quasi-classical behavior, and for a brief period near the end of the laser pulse had a $\Delta r\Delta p_r/\hbar$ in rough agreement with the $\Delta t\Delta\omega$ of the laser pulse that generated the wave packet. The agreement between $\Delta r\Delta p_r/\hbar$ and $\Delta t\Delta\omega$ was not exact, but the agreement was striking enough to suggest that it would be worthwhile to study the theory of atom-laser interactions in terms of laser-pulse Fourier relations, and atomic uncertainty products.

A derivation of the wave packet using the WKB approximation implied that it was the quantity $\Delta t\Delta H/\hbar$ of the wave packet that in certain limits closely agrees with the $\Delta t\Delta\omega$ of the laser pulse. The derivation was useful in revealing some of the many ways in which a coherent Gaussian laser pulse may fail to generate a wave packet satisfying $\Delta t\Delta H/\hbar = 1/2$. Let us review this chapter by discussing some of the ways in which a coherent Gaussian laser pulse may fail to generate a wave packet satisfying $\Delta t\Delta H/\hbar = 1/2$.

First, it is important to notice that the shape of the Rydberg wave packet is strongly governed not by the laser pulse envelope f(t) but by $f(t)a_g(t)$, where $a_g(t)$ is the amplitude of the initially populated state. Similarly, ΔH is calculated from the Fourier transform of $f(t)a_g(t)$, not f(t). If $a_g(t)$ is rapidly varying, then it will strongly modify the value of ΔH, and $\Delta H/\hbar$ will not equal $\Delta\omega$. Throughout this chapter, the laser field was chosen to be weak enough that most of the population remained in the initial state, and $a_g(t)$ remained within 10% of 1.

Second, the theory and the numerical examples discussed in section 2.3 suggest that the laser pulse must be short enough and its bandwidth broad enough to resonantly excite several Rydberg states in order that the $\Delta H/\hbar$ of the atomic state approximate the $\Delta\omega$ of the laser pulse. This is precisely the limit in which a well localized wave packet is generated.

References

1. H. A. Bethe and E. Salpeter, **Quantum Mechanics of One- and Two-Electron Atoms** (Plenum, New York, 1977), p. 19.

2. J. H. Van Vleck, Proc. N. A. S 14, 178 (1928).

3. C. Cohen-Tannoudji, B. Diu, and F. Laloe, **Quantum Mechanics** (Wiley, New York, 1977), p. 62.

4. L. S. Brown, Am. J. Phys. 41, 525 (1973).

CHAPTER III
NUMERICAL INTEGRATION OF SCHRÖDINGER'S EQUATION IN THREE-DIMENSIONS

Section 3.1 Introduction

The purpose of this chapter is to review the numerical methods employed in a numerical integration of the three-dimensional Schrödinger equation. The integration will be used principally in the succeeding chapters as a guide to study of atomic hydrogen interacting with coherent fields of exceptional intensity (10^{14} W/cm^2). Some of the numerical results of the integration will be discussed in this chapter also.

The methods to be discussed in this chapter were developed to solve problems of the type that arose in the previous chapter, in which coherent laser pulses as short as five femtoseconds were used to excite an electron from a hydrogenic bound state to the Rydberg series. Exceptionally high laser intensities are required to substantially ionize an atom with such a short pulse. The major difficulty that arises is that the energy level diagram shown in Fig. 2.1 neglects too many states to accurately describe the atom interacting with such intense fields.

In this chapter a specific example will be studied numerically. The initial state of the hydrogen atom will be the ($n=3, \ell=2, m=2$) state. The laser pulse will be 7.5 femtoseconds (FWHM) in duration, Gaussian in shape, and will be 1/8 of a Rydberg in frequency. The pulse will be linearly polarized and the dipole approximation will be made. The peak field

intensity will be $2.2 \cdot 10^{14}$ W/cm^2. We will see that in such intense fields it will be necessary to include in the atomic energy level structure not just the $\ell = 3$ states, as shown in Fig. 2.1, but also $\ell = 4$, 5, and 6 states.

Section 3.2 Taylor's Series Method of Numerical Integration

The Taylor's series method was the method used to numerically integrate differential equations in all of the numerical examples discussed in this thesis. In this section we will review the method with specific attention to the integration of Schrödinger's equation,

$$\frac{d\Psi(t)}{dt} = -i\, H(t)\, \Psi(t)\,. \tag{3.1}$$

In Eq. (3.1) Ψ is a column vector, and the Hamiltonian H is a matrix whose time dependence is a result of the electric field of the laser pulse.

In the Taylor's series method, the value of Ψ at some time $t_0 + \delta t$ is calculated from

$$\Psi(t_0 + \delta t) \simeq \Psi(t_0) + \sum_{n=1}^{N} \Psi^{(n)}(t_0)\, (\delta t)^n / n!\,, \tag{3.2}$$

In Eq. (3.2) the nth derivative of Ψ evaluated at t_0 has been written $\Psi^{(n)}(t_0)$. The higher order derivatives of Ψ are calculated in terms of the "initial condition" $\Psi(t_0)$ by taking higher order time derivatives of the original differential equation, Eq. (3.1). For example, the time derivative of Eq. (3.1) yields

$$\Psi^{(2)}(t_0) = -i\, H^{(1)}(t_0)\, \Psi(t_0) - i\, H(t_0) \Psi^{(1)}(t_0) \tag{3.3}$$

or,

$$\Psi^{(2)}(t_0) = -i\, H^{(1)}(t_0)\, \Psi(t_0) + i\, H(t_0)\, i\, H(t_0) \Psi(t_0)\,. \tag{3.4}$$

The time variation of H is entirely due to the sinusoidal and Gaussian electric field, so that it is straightforward to calculate a general formula for the nth derivative of Ψ.

Let us make some general remarks on how well the Taylor's series method performed.

1. In improving the accuracy of the numerical integration it was observed that increasing the order N of the Taylor's series, Eq. (3.2), was far superior to decreasing the integration step size δt. For example, in numerically integrating Eq. (3.1), it was found that reducing δt by a factor of two improved normalization of the wavefuction from six significant figures to seven significant figures, and doubled the integration time. By contrast, raising the order of the Taylor's series from order $N=5$ to order $N=9$ also doubled the integration time, but improved the normalization of the wavefunction from 6 to 15 significant figures.

2. When the numerical integration failed catastrophically, as when the normalization of the wavefunction went to infinity, then increasing the order of the Taylor's series did not solve the problem. It was necessary to make the step size smaller. Once the step size was small enough that the numerical integration no longer failed catastrophically, then the most efficient way to improve accuracy was to increase the order of the integration.

3. It was straightforward to work out analytical formulas for the Taylor's series, Eq. (3.2), to arbitrary order N. The ability to choose an arbitrary

order proved to be useful over and over again in ensuring accuracy, not just in the integration of Schrödinger's equation, but in all other numerical integrations attempted in this research. For example, for a particular integration step size, the numerical integration of Schrödinger's equation gave what turned out to be poor answers at order 5, but gave consistent answers at orders 7, 8 and 9. Another case in which this technique turned out to be useful was in the integration of the time-independent Schrödinger's equation for the radial bound states and unbound states of the Coulomb potential. The accuracy of the bound states could be checked, because analytical formulas are available[1] and easily calculated for the unbound states. The order of the Taylor's series could then be turned up arbitrarily to get desired accuracy. This method set the order of the Taylor's series for numerically integrating the unbound states.

Section 3.3 Basis Set for the Numerical Integration of Schrödinger's Equation

Schrödinger's equation in matrix form, Eq. (3.1), is a first order differential equation that is straightforward to numerically integrate via a Taylor's series Eq. (3.2). But in configuration space, Schrödinger's equation is a second order partial differential equation, which is difficult to integrate numerically. In order to write Schrödinger's equation in matrix form, a complete set of states is needed as a basis set.

The natural choice of basis sets is the set of eigenstates of the atomic Hamiltonian, H_{atom}. The electron is in an eigenstate of H_{atom} before the

laser pulse arrives, and is in a coherent superposition of eigenstates of H_{atom} after the laser pulse has departed. During the pulse, the set of eigenstates of H_{atom} simply serves as complete set on which to solve the equation.

In order to make the basis set finite, it is assumed that at some large radius r = R there is a spherical boundary of infinite potential energy surrounding the atom centered at r=0. The effect of the boundary is to discretize the continuum of unbound states. The set of eigenstates that results is complete for solutions of Schrödinger's equation that satisfy the boundary conditions: $\Psi(0) = 0$, and $\Psi(R) = 0$. To justify the use of such an eigenbasis, we must verify that the wave packet representing the excited electron does not travel from the nucleus at r=0 to the boundary at r=R during the laser excitation. In the numerical examples discussed in this thesis, R is set at 1400 Bohr radii, and the wave packet representing the ionized electron travels only 1/4 of the distance to the boundary during the 22.5 femtoseconds of the numerical integration. In the next section figures showing the wave packet at the end of the pulse will be presented.

Let us next turn to some of the numerical problems encountered in the construction of the basis set. The eigenenergies were found by the well known[2] point and shoot method. First an approximate value E_1 for the eigenenergy was determined using the WKB method, and then E_1 and a slightly larger $E_1 + \delta E$ were used to construct two candidate eigenstates. Using interpolation, and the degree by which the two candidate eigenstates failed to satisfy the boundary conditions, it was possible to predict an improved eigenenergy E_2. Thus, by iteration the eigenenergy E

could be calculated. The process converged surprisingly quickly. At most three iterations were required to get an energy E such that the wavefunction was zero to 14 significant figures at the outer boundary.

The energy level diagram of the basis set is drawn in Fig. 3.1. For each azimuthal quantum number ℓ, the true basis set has an infinite number of states. Each element of the basis set has the form $Y_{\ell,m}(\theta,\phi)u_{E,\ell}(r)$, where $Y_{\ell,m}(\theta,\phi)$ is the spherical harmonic, m is always 2, ℓ varies from 2 to 6, and the energy eigenvalues E are fixed at discrete energies by the boundary conditions. The function $u_{E,\ell}(r)$ is the eigenstate of the radial Schrödinger equation, with effective potential $-e^2/r + \hbar^2\ell(\ell+1)/(2mr^2)$. To make the energy level diagram Fig. 3.1 more legible every fifth positive energy state is plotted. The continuum states (unbound states) are not evenly spaced in energy, but are (nearly) evenly spaced in momentum. This spacing, sometimes called the momentum scale, results from the choice of boundary conditions. The eigenstates of the well-known infinite square well have a similar property. In each of the continua ($\ell=2$ to 5) there are 270 unbound states. At $\ell=6$, 370 unbound states are used. In each case, the number of bound states is about 30.

In Fig. 3.1, the arrows correspond to possible resonant transitions. As shown in the figure, the initial state is ($n=3$, $\ell=2$, $m=2$). This choice of initial state and linear field polarization simplify the excitation in an important way. Because the dipole approximation is made throughout, the dipole selection rules for linearly polarized light forbid transitions from the ($\ell=2$, $m=2$) initial states to the $\ell=1$ states.

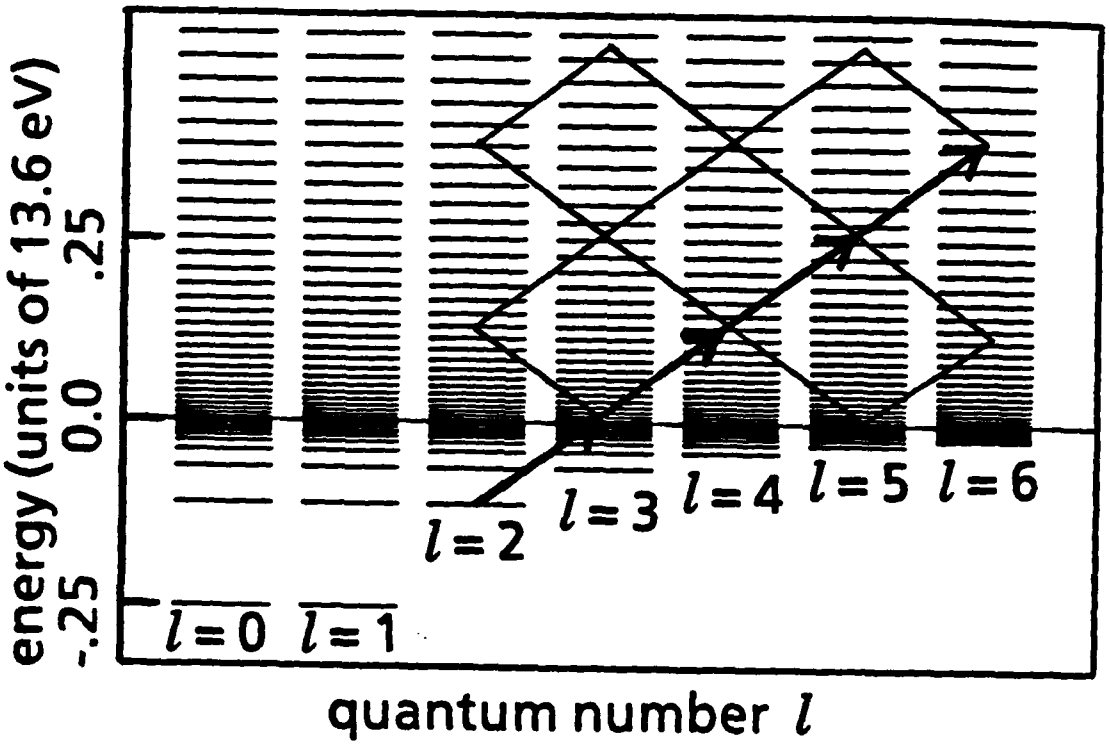

Fig. 3.1. Energy level diagram for the numerical integration of Schrödinger's equation. The thick arrows represent the most probable paths taken by population during the excitation. The population also follows the thin lines, although these paths are of less importance because of the smaller dipole moments. One in five of the unbound states are plotted. Altogether over 1600 states were used.

This prevents, for example, a Rabi oscillation between the ($n=3, \ell=2$) and the ($n=2, \ell=1$) states that would greatly complicate the problem. In Fig. 3.1 the thick arrows represent the absorption of $\hbar\omega$ in energy and are drawn to represent the most probable path that population takes during the excitation. Cross sections are largest for transitions in which both energy and angular momentum increase. Some population also follows the thin lines, but these excitation paths do not contribute significantly to the final spectrum.

One of the advantages of integrating the equation on a complete set of discrete, physical states is that particular bound states may be removed from the set during the time integration to see what effect they have on the ATI energy spectrum. This tells us unambiguously the origin of effects such as the inhibition of ionization. Using a physical basis set, and knowing which bound states are of importance during the excitation allows us also to generalize results to other one-electron atoms. It is easily seen from the energy level diagrams of lithium and sodium that the results would differ little in the $m=2$ case if the atom were lithium or sodium. In recent years, another numerical method, the Sturmian method has become increasingly popular in problems of the sort discussed here. It should be noted that the Sturmian basis states are not equivalent to the hydrogenic basis states drawn in Fig. 3.1. A recent review of the advantages and disadvantages of the two methods is given by Susskind and Jensen[3].

Section 3.4 Numerical Results: Above-threshold Ionization

In this section we will discuss some of the results revealed by the numerical integration. To produce the results to be discussed in this section, the step size of the time-integration was made sufficiently small that the wave function Ψ remained normalized to ten significant figures throughout the integration. We then repeated the numerical integrations with a smaller step size and higher order Taylor's series, so that the wave function remained normalized to 15 significant figures. The results remained unchanged.

As remarked above, about 1600 states ($\ell = 2,3,4,5$ and 6) were used in the integration. The fact that we cannot use the full infinite set of basis states in the integration meant that another approximation was necessary, namely the essential states approximation, in which states that receive virtually no population during the excitation are discarded from the basis set. This approximation was relatively easy to make reliably. It was however necessary to inspect the population of the states during the numerical integration. Many more states than were necessary for the integration were kept in the basis. In particular we kept states of high energy and high angular momentum that received negligible population and that could only receive population through many-photon transitions.

In Fig. 3.2 is plotted the final energy distribution of the electron as predicted by the numerical integration of Schrödinger's equation. The solid curve represents the energy distribution of the electron at the end of the pulse. The curve is constructed by dividing each photon energy interval (of energy 1/8th Rydberg) into ten bins. The amount of population in each bin is plotted in Fig. 3.2. The bound states are drawn as rectangles;

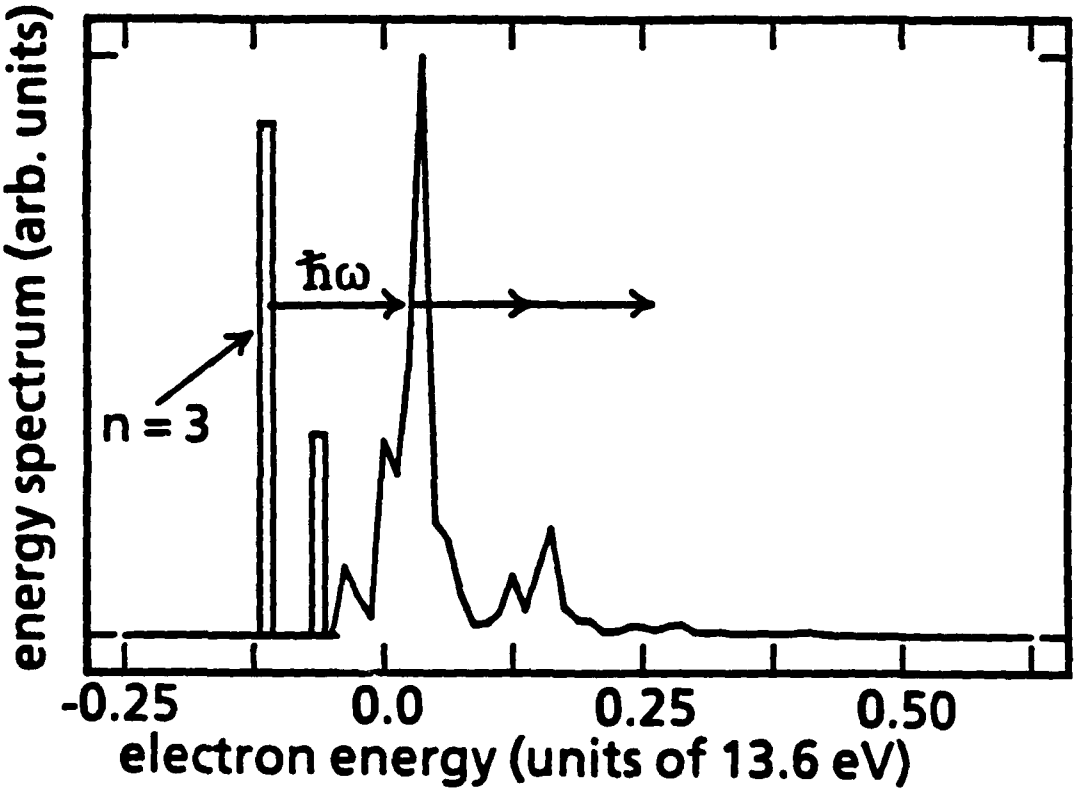

Fig. 3.2. Electron energy at the end of the excitation pulse. The separation of the x-axis hash marks is one photon in energy: 1/8th Rydberg. The curves are constructed by dividing each energy interval of 1/8th Rydberg into ten bins. Population in each bin is plotted with a rectangle for the bound states $n=3$ and $n=4$, and with a solid line otherwise. Here the initial state is $n=3$, $\ell=2$, $m=2$ and the peak intensity of the laser pulse is $2.2 \cdot 10^{14}$ Watts/cm^2.

the population in unbound states (the ionization spectrum) is plotted with a smooth curve rather than a histogram to make comparison with the other theories easier. There are four ionization peaks, although the fourth, with .09% of the population, is not visible in the figure. The figure demonstrates that the atom is undergoing a certain amount of above-threshold ionization, in which more photons are absorbed than are necessary to ionize the atom.

It is instructive to compare the example of ATI presented in this chapter with some of the experimental parameters of the well-known ATI experiments. All experiments to date have been done in the low frequency limit, in which a many photon transition is required to ionize the atom. An analysis of the Stark shifts of the bound states in this limit yields a simple formula which is widely quoted in the ATI literature and which can be extremely useful in providing simple explanations to very complicated multi-photon phenomena. For example, the frequency shift of the initial state is given by second-order perturbation theory[4]:

$$\Delta E = -U_p - .5\alpha E^2 \quad , \tag{3.5}$$

where α is the ground state polarizability given by the dc stark effect. The quantity U_p equals $e^2E^2/(4m\omega^2)$, where E is amplitude of the electric field. The quantity U_p is called the ponderomotive potential because it also shows up in an analysis of ponderomotive effects. (However, effects due to ponderomotive forces are not directly related to the Stark-shift theory discussed here.) In the numerical example described in this chapter, U_p is .16 multiplied by the Rydberg energy at the peak intensity of the pulse, or slightly greater than the peak energy of the field photon, $\hbar\omega$. Both of the

terms in Eq. (3.5) are negative, so the formula predicts extemely large frequency shifts. The derivation of Eq. (3.5) (given in ref. 4) requires that the frequency difference between the initial state and all neighboring states be very much greater than the field frequency ω. This is typically the case when a many-photon transition is required to ionize the atom. A calculation of the frequency shifts of threshold (Rydberg) states[5] yields a similarly large value: U_p.

In light of this theory, let us return to the example of ATI presented in this chapter. In the numerical results, we clearly do not see frequency shifts of the order U_p. This is puzzling at first. Since the frequency shifts are intensity dependent, and since a high percentage of the population in the first ionization peak gets there during the turn-on of the pulse when the pulse varies in intensity greatly, large intensity-dependent frequency shifts would shift the peaks a variable amount during the pulse, and have the effect of broadening the ionization peaks. There is no evidence of shifts or broadening of peaks of the order U_p. The failure of Eq. (3.5) to apply to the numerical results presented in this chapter is easy to explain. Equation (3.5) is derived under the assumption that many photons are required ionize the atom, and that the frequency of the laser is very much less than the frequency difference between the initial state and all intermediate states. In the numerical examples studied here, these conditions do not hold.

However, calculation of the frequency shifts of the threshold states also yields the large value U_p. Why such a shift is not apparent in the

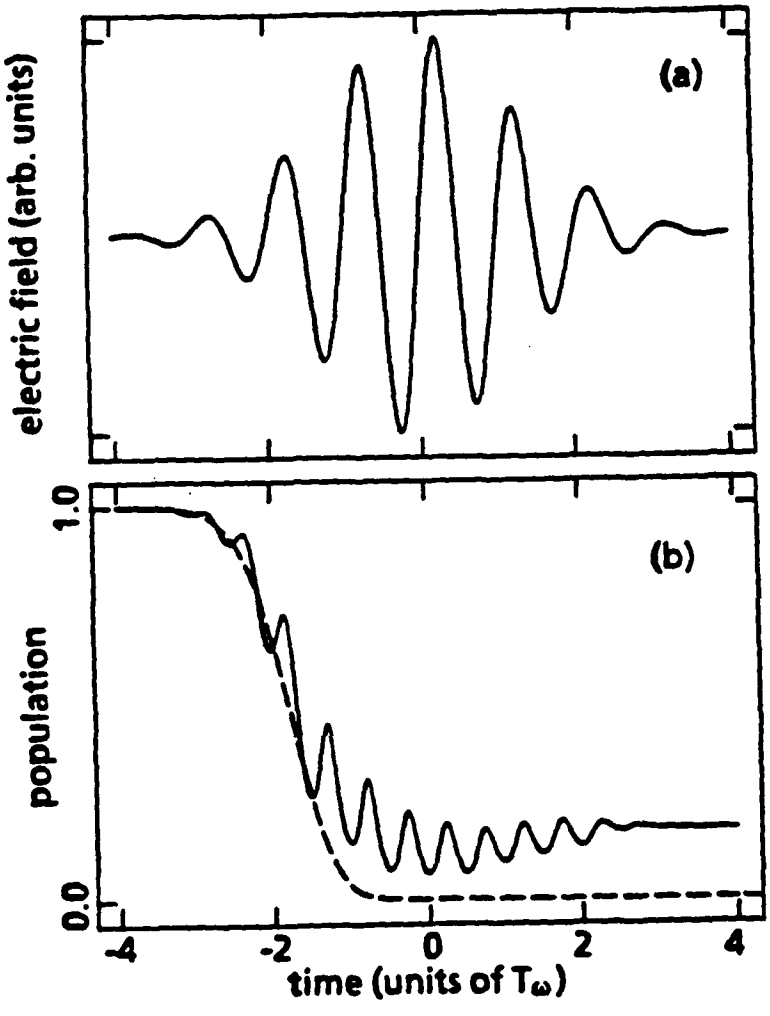

Fig. 3.3. (a) Laser pulse electric field. The pulse has a Gaussian envelope, and the optical frequency ω is 13.6eV/(8$\hbar$). The pulse has a FWHM of $3T_\omega$. T_ω is the period of the optical field. (b) Population in the initial ($n=3$, $\ell=2$, $m=2$) state during the laser pulse. The solid lines shows the initial state population predicted by the numerical integration of Schrödinger's equation. The dashed line shows the initial state population predicted by Fermi's golden rule.

numerical results is more troubling. One possibility is that the discrepency between theory and numerical experiment is due to the failure of second order time-independent perturbation theory at high intensities. They successfully describe the frequency shifts of ionization peaks in high-resolution spectroscopy, in which laser fields are CW and orders of magnitude weaker than in this work. But the justification of these techniques at high field intensities is non-trivial, and does not fall within the scope of this thesis.

Section 3.5 Numerical Results: The Failure of Fermi's Golden Rule

In Fig. 3.3(b) is plotted (solid line) the population of the initial state ($n=3, \ell=2, m=2$) during the pulse. The pulse peaks in intensity at $t=0$ and has a FWHM of $3T_\omega$, where T_ω is the period of the electric field. From Fig. 3.3(b) it is evident that when the pulse is the most intense ($t=0\pm1.5T_\omega$) almost no net population leaves the initial state.

For comparison, Fig. 3.3(a) shows the electric field of the laser pulse. The rapid oscillations in the population of the initial state (solid line of Fig. 3.3(b)) have a frequency of twice the optical frequency of the electric field. These are counter-rotating oscillations, that are normally discarded in the rotating-wave approximation. This inhibition of ionization may be characterized as an intense-field modification of Fermi's golden rule (FGR). For comparison, the FGR prediction is also plotted in Fig 3.3b (dashed line). The FGR rate of exponential decay is calculated by assuming

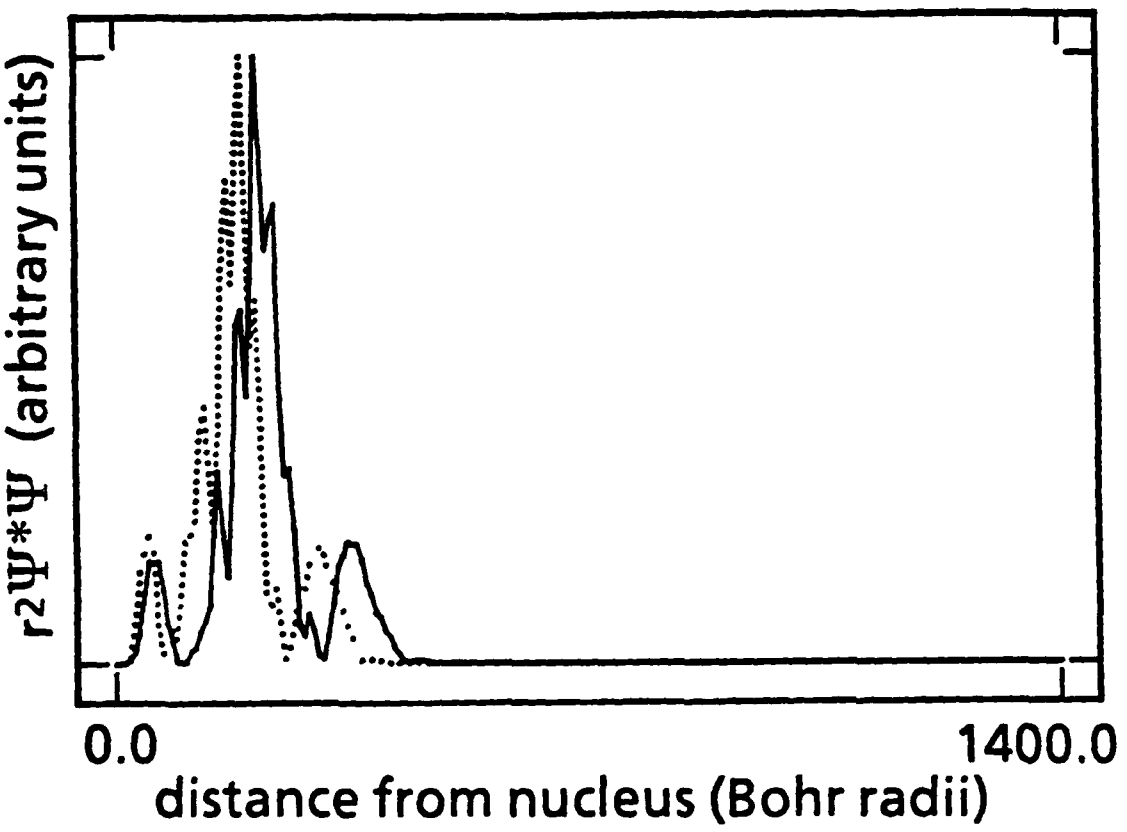

Fig. 3.4. Electron wave packets near the end of the laser pulse. The figure shows only the radial distribution of the ($\ell = 6$, $m = 2$) wave packets. The dotted line shows the wave packet as it appears 9.0 femtoseconds after the laser pulse peaked in intensity. The solid line shows the wave packet 11.25 femtoseconds after the laser peaked in intensity. In both cases the laser pulse has fallen to less than .5% the peak intensity, so the motion of the electron is not strongly perturbed by the laser.

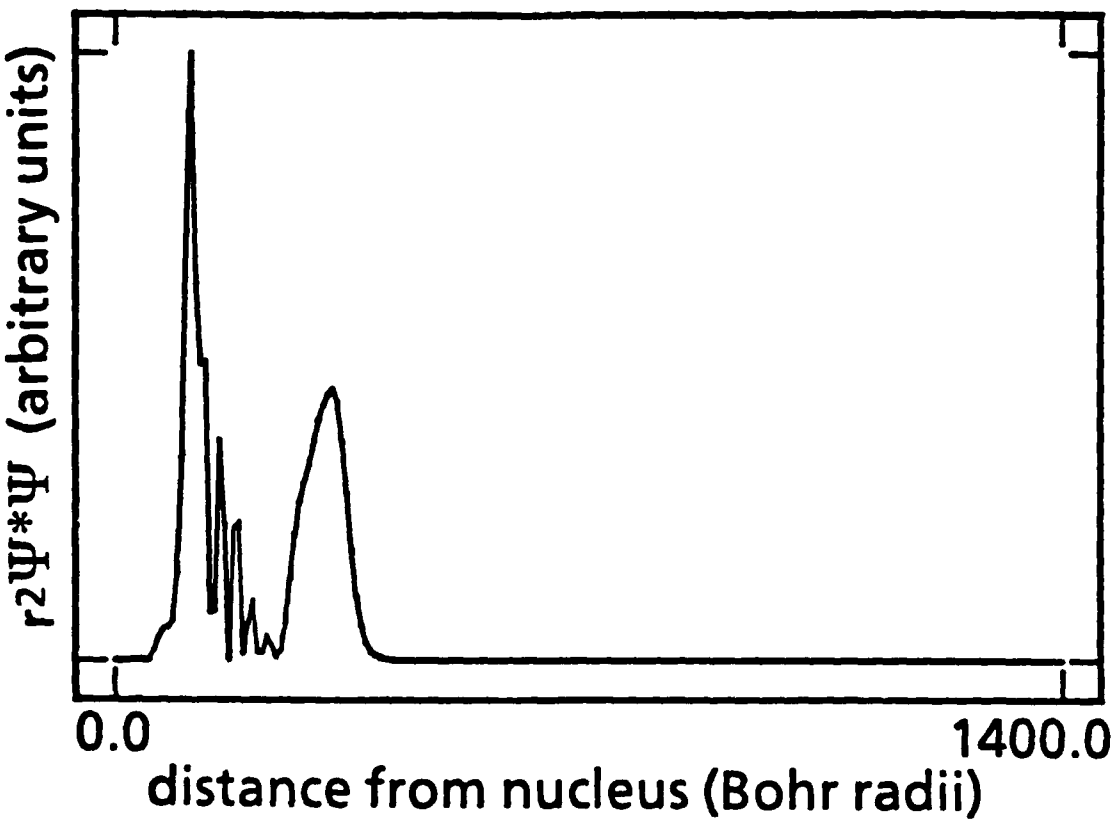

Fig. 3.5. Electron wave packet near the end of the laser pulse. The figure shows the radial distribution of the ($\ell=5$, $m=2$) wave packet. The solid line shows the wave packet when the numerical integration finishes, 11.25 femtoseconds after the laser peaked in intensity.

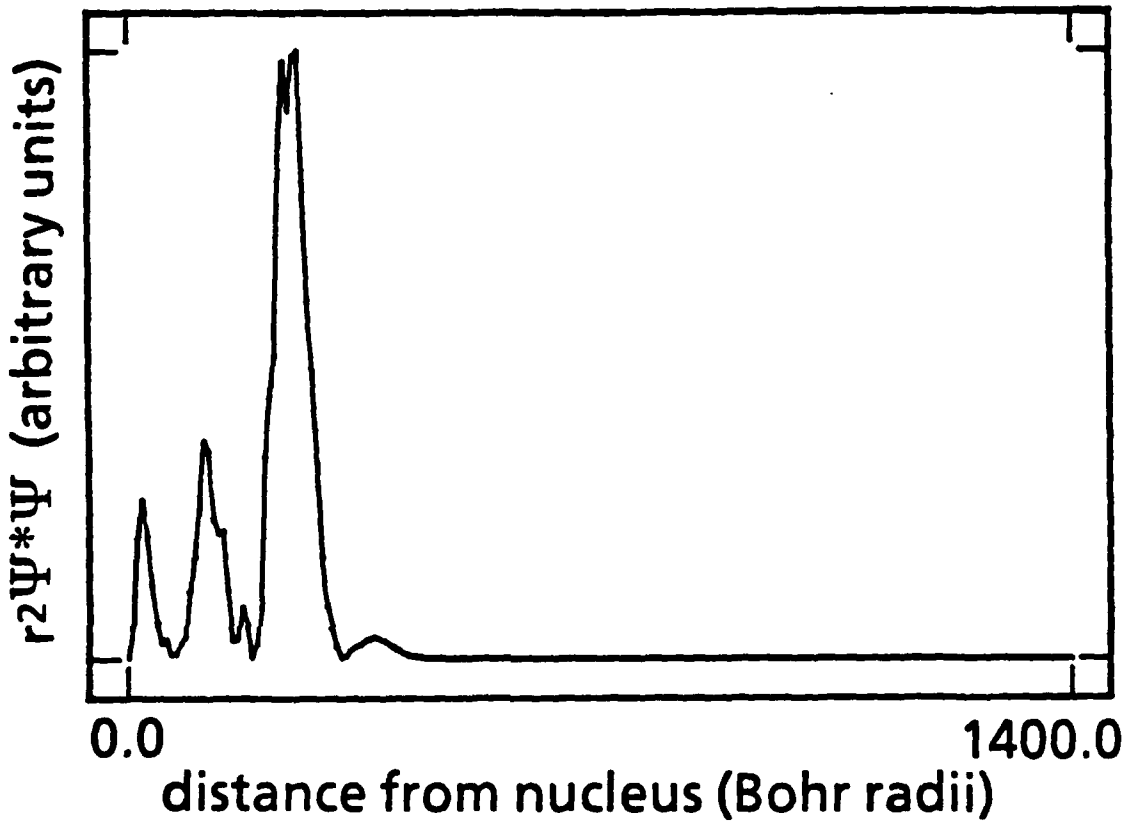

Fig. 3.6. Electron wave packet near the end of the laser pulse. The figure shows the radial distribution of the ($\ell = 4$, $m = 2$) wave packet. The solid line shows the wave packet when the numerical integration finishes, 11.25 femtoseconds after the laser peaked in intensity.

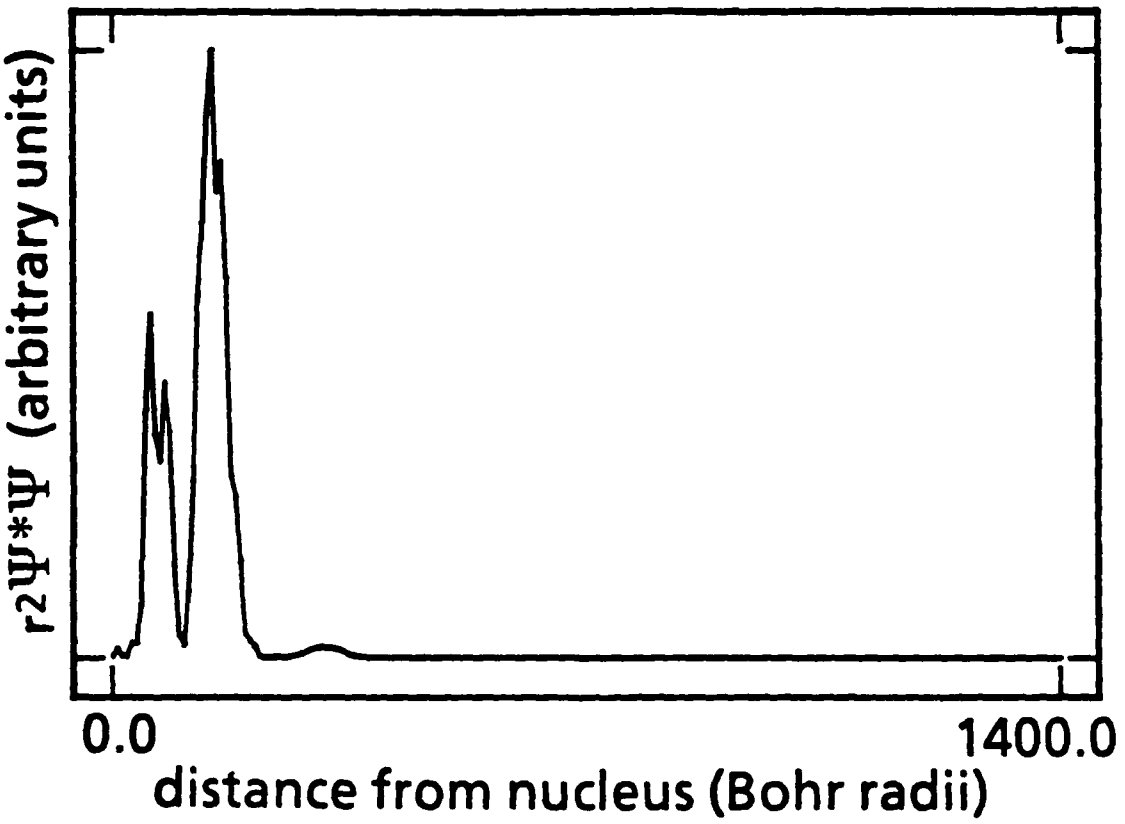

Fig. 3.7. Electron wave packet near the end of the laser pulse. The figure shows the radial distribution of the ($\ell=3$, $m=2$) wave packet. The solid line shows the wave packet when the numerical integration finishes, 11.25 femtoseconds after the laser peaked in intensity.

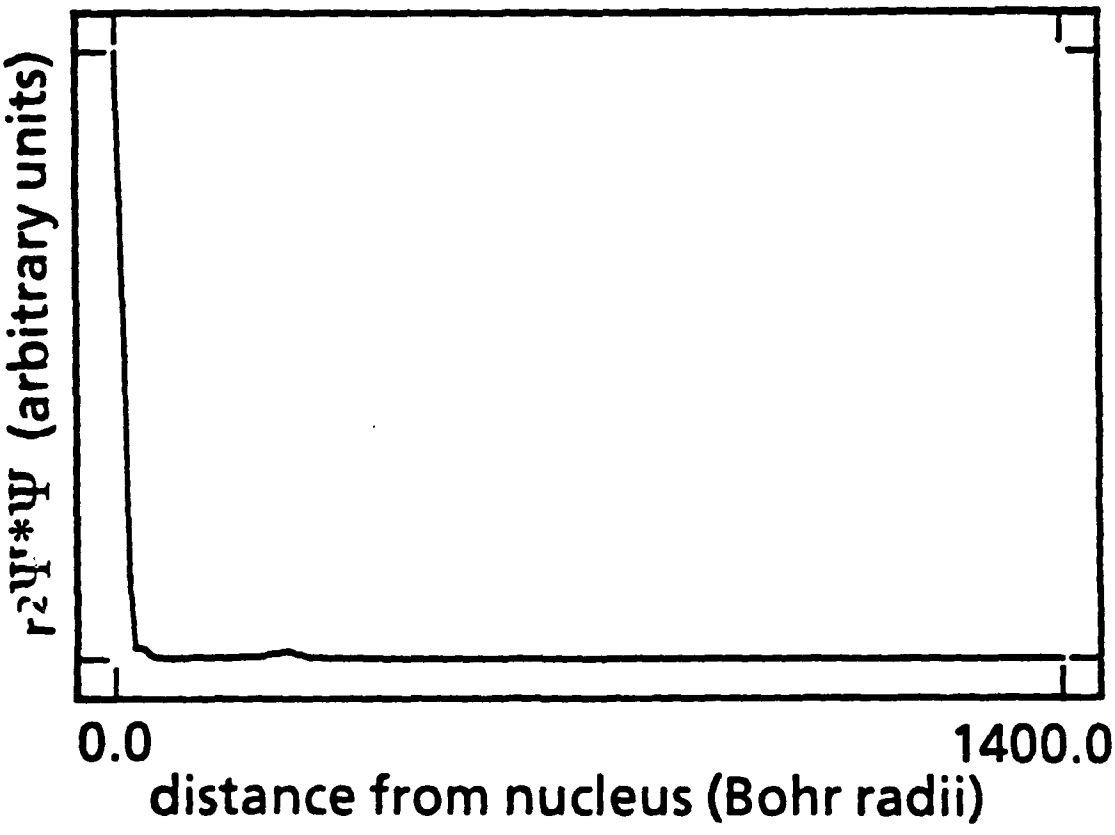

Fig. 3.8. Electron wave packet near the end of the laser pulse. The figure shows the radial distribution of the ($\ell=2$, $m=2$) wave packet. The solid line shows the wave packet when the numerical integration finishes, 11.25 femtoseconds after the laser peaked in intensity.

a single $\ell=2$ bound state and a single $\ell=3$ continuum of unbound states. A simple FGR calculation predicts complete ionization at intensities an order of magnitude lower than the 2.2×10^{14} W/cm^2 peak intensity actually used.

The origin of the inhibited ionization may be easily demonstrated by removing basis states from the basis set during the integration. If the states (n=4, $\ell=2$, m=2) and (n=5, $\ell=2$, m=2) are removed from thebasis set, then the initial state decays nearly as predicted by FGR. Absorption of population by the n=4 and 5 states (via the $\ell=3$ continuum of unbound states) then in effect inhibits ionization.

These results cannot be modelled by the methods of chapter II. In chapter II FGR worked well and the laser fields were weak in the sense that at least 90% of the population remained in the initial state during the laser pulse. This trapping of population in intense fields will be studied analytically in the next chapter.

Section 3.6 Wave Packets Representing an Electron Undergoing ATI

Finally, we show in Figures 3.4 through 3.8 the spatial (radial) distribution of the wave function at the end of the numerical integration. The figures do not show the true $\Psi^*\Psi(r,t)$. The true wave function $\Psi^*\Psi(r,t)$ is calculated from the square modulus of $\Sigma\Psi_\ell(r)Y_{\ell,2}(\theta,\phi)$ where the sum is over the angular momentum ℓ. Instead the figures show $r^2|\Psi_\ell(r)|^2$ for $\ell=2$ to 6 where r is the radial variable r = |r|. The true wave

function $\Psi^*\Psi(r,t)$ probably has complicated interference phenomena from cross-terms in the square modulus of $\Sigma\Psi_\ell(r)Y_{\ell,2}(\theta,\phi)$. This interference does not show up in the figures. However, the principal purpose of Figs. 3.4-3.8 is to show that the wave packet representing the above-threshold ionized electron has not reached the artificial infinite-potential boundary at r = 1400 Bohr radii. The success of the numerical method relies heavily on this fact, so it was especially important to verify.

Figure 3.4 shows the wavefunction of the sixth continuum $r^2|\Psi_6(r)|^2$ at the end of the laser pulse, t = 11.25 femtoseconds (solid line), and well as the wave packet at a somewhat earlier time, 9.0 femtoseconds (dotted line). The figure was drawn to give an idea of the velocity of wave packet relative to the well.

The wave packets shown in Figs. 3.4-3.8 were valuable in another respect. They proved to be sensitive tests for certain numerical errors. For example, in an early attempt to numerically integrate Eq. (3.1), the wave functions did not show the sharp leading-edge cut-off that Figs. 3.4-3.8 show. Instead, the wave packet appeared throughout the cavity, even early in the integration, as though the electron had traveled at unphysically high velocities to reach the outer boundary. It was found that a single element of the basis set had been inadvertantly left out during the integration. When the missing state was re-introduced into the basis set, then the wave packets had sharp leading edges, as shown in the figures. In each of the Figs. 3.4-3.8 the wave packet $r^2|\Psi_\ell(r)|^2$ at values of r beyond the leading edge of the wave packet is 5 to 6 orders of magnitude smaller than the peak value of the wave packet.

Section 3.7 Conclusion

In this chapter we began the study of the interaction of one-electron atoms with coherent laser pulses of exceptionally high intensity. The purpose of the chapter was to discuss the methods and some of the results of a numerical integration of a second-order partial differential equation in three-dimensions: Schrödinger's equation describing an atom in fields of $2.2 \cdot 10^{14} W/cm^2$ peak intensity. The numerical integration revealed several surprising intense-field effects that cannot be explained by the analysis of chapter II. The first effect was a population trapping effect. Population remained trapped in the initial state of the atom in striking disagreement with the Fermi golden rule prediction. The second effect was above-threshold ionization. The electron absorbed as many as three photons in energy in excess of that required to ionize it. These phenomena will be studied analytically in the following chapters.

References

1. H. A. Bethe and E. E. Salpeter, **Quantum Mechanics of One- and Two-Electron Atoms** (Plenum, New York, 1977).

2. W. H. Press, B. P. Flannery, S. A. Teulosky, and W. T. Vetterling, **Numerical Recipes** (Cambridge Press, Cambridge, 1986) p. 582.

3. S. M. Susskind and R. V. Jensen, Phys. Rev. A 38, 711 (1988).

4. L. Pan, L. Armstrong, Jr., and J. H. Eberly, J. Opt. Soc. Am. B 3, 1319 (1986).

5. P. Avan, C. Cohen-Tannoudji, J. Dupont-Roc, and C. Fabre, J. Phys. (Paris) 37, 993 (1976).

CHAPTER IV
POPULATION TRAPPING IN SHORT PULSE LASER IONIZATION

Section 4.1 Introduction

In the previous chapter we presented a numerical study of above-threshold ionization of hydrogen by an intense ($2.2 \cdot 10^{14}$ W/cm^2), short (7.5 femtosecond) laser pulse. In order to integrate the full three-dimensional Schrödinger equation a few specializing assumptions were made. In particular it was assumed that the atom was prepared in the $n=3$, $\ell=m=2$ state, and that the field frequency was $\omega_R/8$, one-eighth the Rydberg frequency. One particularly striking result of the numerical study was the observation that the atom was not completely ionized even for extremely intense fields. Instead some of the population was trapped in the initial state.

In this chapter we will study the basic physics of this trapping and see that it is a quite general occurrence for any process in which a short laser pulse is used to excite an atom. The only requirement is that there be other bound levels of the same parity as the initial state, separated from the initial state by less than the bandwidth of the laser pulse. Although the original numerical study was carried out for the case of hydrogen, we will demonstrate the basic physics using a much simpler model atom. The level structure of this atom is shown in Fig. 4.1. In this model atom we have three bound states that are of the same parity as the initial state, and

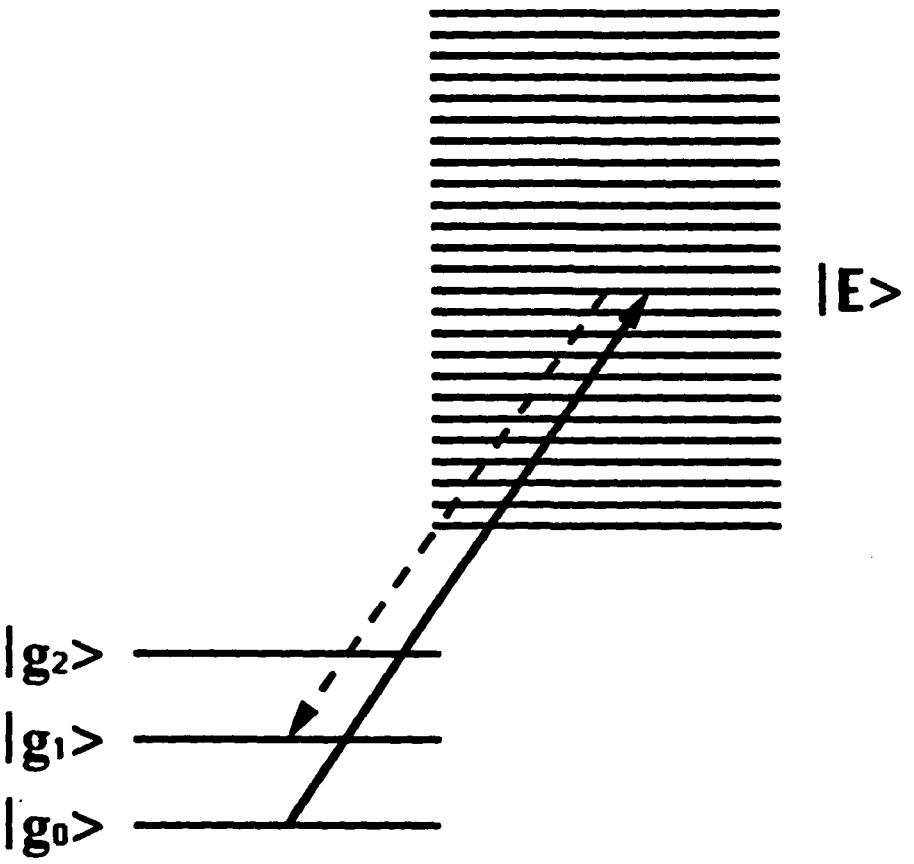

Fig. 4.1. Energy level diagram of ionization model. The states $|g\rangle$ are bound states of angular momentum ℓ_0. All of the population is initially in state $|g_0\rangle$. The states $|E\rangle$ represent unbound states of angular momentum quantum number ℓ_0+1. The separation of the states $|E\rangle$ is small enough that the quasi-continuum of states in the drawing behaves as a continuum of unbound states.

for simplicity are equally spaced in energy. The continuum is modeled by a quasi-continuum that is made up of equally spaced levels, each with the same dipole moment coupling to the bound levels. The solid arrow indicates the transition from the initial state to the continuum produced by the center frequency of the laser pulse. Because of the finite bandwidth of the short laser pulse, the second transition indicated by the dashed line will also be resonantly excited by the laser field, returning population to the set of initially unpopulated bound states $|g_1>$, $|g_2>$, and so on. The field then produces not only ionization but also stimulated recombination. As we shall see, the return of population inhibits the ionization from the initial state $|g_0>$. Without the presence of the states $|g_1>$, $|g_2>$, and so on, the ionization would be accurately described by Fermi golden rule (FGR) exponential decay. The effect we will be describing, then, may be characterized as one of the ways FGR fails in the intense field ionization of real atoms and molecules.

As remarked above, the conditions for population trapping (Fig. 4.1) are likely to be encountered in a variety of laser-molecule interactions due to the close spacing of the $|g>$ levels. The same is true in the study of microwave Rydberg-atom interactions. Several authors have studied the problem from this point of view [1,2] and have reported on coherent effects that trap population or modify Fermi's golden rule. Inhibition of ionization and population trapping due to coherences among two or more bound states has been extensively studied both in the theory of two-color ionization[3] and in the theory of one-color ionization[4].

As pointed out above, the recapture of population by the bound states $|g>$ occurs during ionization by very short laser pulses that have sufficiently broad bandwidth to drive both the transition represented by the solid arrow of Fig. 4.1 and the transition represented by the dashed arrow of Fig. 4.1. For inhibition of ionization to become apparent, the pulse must also be sufficiently intense to drive significant population along this two photon transition. As we shall see, under these conditions a coherent superposition $\Psi_c(t) = \Sigma\, a_g(t)\, |g>$ is generated that exhibits a greatly reduced ionization cross section in comparison to the ionization cross section of the initial state $\Psi_0(t) = a_{g_0}(t)\, |g_0>$.

It is surprising that population should return from the ionization continuum $|E>$ with just the right phase to strongly inhibit ionization of an atom prepared initially in the discrete bound state $|g_0>$. The numerical integration reveals the phenomenon but can not tell us if it occurs under more general conditions. Consequently, a major goal of the chapter is to develop a theory capable of predicting the major features of the phenomenon for a variety of laser pulse shapes, field intensities, atomic dipole moments, and atomic energy level spacings. Throughout this chapter, predictions of the theory will be compared with predictions of the numerical solution of Schrödinger's equation on the set of states of Fig. 4.1. The theory will be presented in two versions. The first version will employ the rotating-wave approximation (RWA). The RWA version of the theory is useful in demonstrating in an uncomplicated way the general features of population trapping and inhibited ionization. The RWA

version of the theory can be solved analytically in several special but instructive cases.

The RWA version of the theory shows a small but systematic failure in comparison with the numerical integration of Schrödinger's equation. The failure is due to the failure of the RWA. To demonstrate this, we have also developed a more sophisticated theory that does not employ the RWA. The more sophisticated version gives superior agreement with the numerical integration of Schrödinger's equation.

In section 4.2 we will write down the appropriate equations of motion for the system of Fig. 4.1, and describe some numerical solutions that demonstrate the effects to be studied here. In section 4.3 the simplest version of the theory will be presented. The strategy will be to eliminate the variables associated with the unbound states $|E>$, leaving equations involving only the variables of the bound states. The resulting equations may then be solved numerically, or in special cases, solved analytically. In sections 4.4 and 4.5, the equations will be solved analytically in two particularly instructive cases. In section 4.4 it will be assumed that the bound states $|g>$ are degenerate in energy. The result will be that population is permanently trapped in the initial state $|g_0>$. In section 4.5 it will be assumed that the states $|g>$ are not degenerate in energy but that the pulse is rectangular in shape. In section 4.6 the theory will be generalized to take into account terms that are discarded when the RWA is made.

Section 4.2 Schrödinger's Equation and Numerical Solutions

In this section we will write down the Schrödinger equation for the set of states shown in Fig. 4.1 and describe some numerical solutions.

Schrödinger's equation in the dipole approximation, restricted to the set of states of Fig. 4.1 is,

$$i\frac{da_E(t)}{dt} = \sum_g 2V_{Eg}\, a_g(t)\, \exp(-i\omega_g t)\exp(i\omega_E t)\sin(\omega t) f(t) \ , \qquad (4.1a)$$

$$i\frac{da_g(t)}{dt} = \sum_E 2V_{Eg}\, a_E(t)\, \exp(i\omega_g t)\exp(-i\omega_E t)\sin(\omega t) f(t) \ . \qquad (4.1b)$$

In Eq. (4.1), $2\hbar V_{Eg} f(t)\sin(\omega t)$ is the matrix element of the interaction Hamiltonian connecting the states $|E>$ and $|g>$. The energy of the state $|E>$ is $\hbar\omega_E$, the energy of the state $|g>$ is $\hbar\omega_g$, and $\hbar\omega$ is the photon energy. The electric field goes as $f(t)\sin(\omega t)$. Here the pulse envelope function, $f(t)$, is normalized to unity at its maximum. The variables $a(t)$ are the probability amplitudes of the states in the interaction picture. To make the notation simpler, $a_{g_0}(t)$ will be written $a_0(t)$, and $a_{g_1}(t)$ will be $a_1(t)$.

Next, we review the method of numerically integrating Eq. (4.1). The numerical integation of Eq. (4.1) was performed using a set of 150 equally spaced states (Fig. 4.1) to represent the ionization continuum. The laser pulse was (in all of the numerical examples shown in the figures) three optical periods FWHM in duration. The ground states $|g>$ are equally spaced in frequency, unlike the hydrogenic states, and are drawn to scale

in Fig. 4.1. The actual integration was accomplished by the Taylor's series method. The 150 states span a width in frequency equal to that of the frequency of the laser pulse. It is well known[5,6] that a quasi-continuum of discrete states behaves as an ionization continuum provided the states are sufficiently closely spaced in energy. The discrete nature of the quasi-continuum begins to become apparent after a time $2\pi/\Delta$, where Δ is the frequency separation of the states. In this case Δ is $\omega/150$ where ω is the laser frequency, so that $2\pi/\Delta$ is 150 periods of the laser field. The entire integration period of the examples shown in the figures is nine field periods. To understand why the discrete nature of the continuum should become apparent in the numerical integrations only after a time $2\pi/\Delta$, notice that pulse lengths of this duration or longer have a sufficiently narrow spectrum to resolve the level structure, but shorter pulses have too broad a spectrum.

In the case of the real hydrogen atom the situation is more complex than for the simple model atom studied here. Our numerical studies of hydrogen (using the ($\ell=2$, $n=3$) state as the initial $|g_0>$ state of Fig. 4.1) show that the counter-rotating terms at frequency 2ω are more pronounced than here, and several more atomic levels are coupled into the problem. To model the hydrogen atom accurately in such intense fields we have found that it is necessary to introduce the bound states ($\ell=3$, $n=4$), ($\ell=3$, $n=5$) and ($\ell=4$, $n=5$), as well as the ionization continua to which these states are coupled. The effect of these ($\ell=3$) bound states is to increase greatly the amplitude of the oscillations of frequency 2ω that are apparent in the numerical integrations of Eq. (4.1).

Figures 4.2 and 4.3 present several numerical solutions of Eq. (4.1) and demonstrate the profound effect that the states $|g_1>$ and $|g_2>$ have on the ionization rate of the initial state $|g_0>$. All three curves of Fig. 4.2 represent the population of the initial state, $|g_0>$, during the pulse. The pulse peaks in intensity at t=0. The pulse has 3 optical periods per FWHM. In Fig. 4.2, the solid curve labeled 1 represents the time evolution of $|g_0>$ in the case in which $|g_0>$ is the only bound state. The evolution of $|g_0>$ in this case most closely resembles FGR exponential decay. The peak pulse intensity I_0 was chosen so that FGR predicts that 90% of the population would be removed from the initial state by the time the pulse peaks in intensity. The curve labeled 2 represents the evolution of $|g_0>$ with one other bound state $|g_1>$ present. Now the inhibition of ionization (in comparison to the FGR prediction) is clearly evident. The curve labeled 3 represents the evolution of $|g_0>$ with the two states $|g_1>$ and $|g_2>$ present. The inhibition of ionization is greater.

In Fig. 4.3 the intensity of the pulse is varied, rather than the number of bound states as in Fig. 4.2. In each of the three cases shown in Fig. 4.2 there are three bound states. The solid line shows the evolution of $|g_0>$ at the same intensity I_0 used in Fig. 4.2. The dotted and dashed lines show the evolution of $|g_0>$ at intensity $2 \cdot I_0$ and $10 \cdot I_0$ respectively. Increasing the intensity by a factor of ten increases the population remaining in the initial state at the end of the pulse.

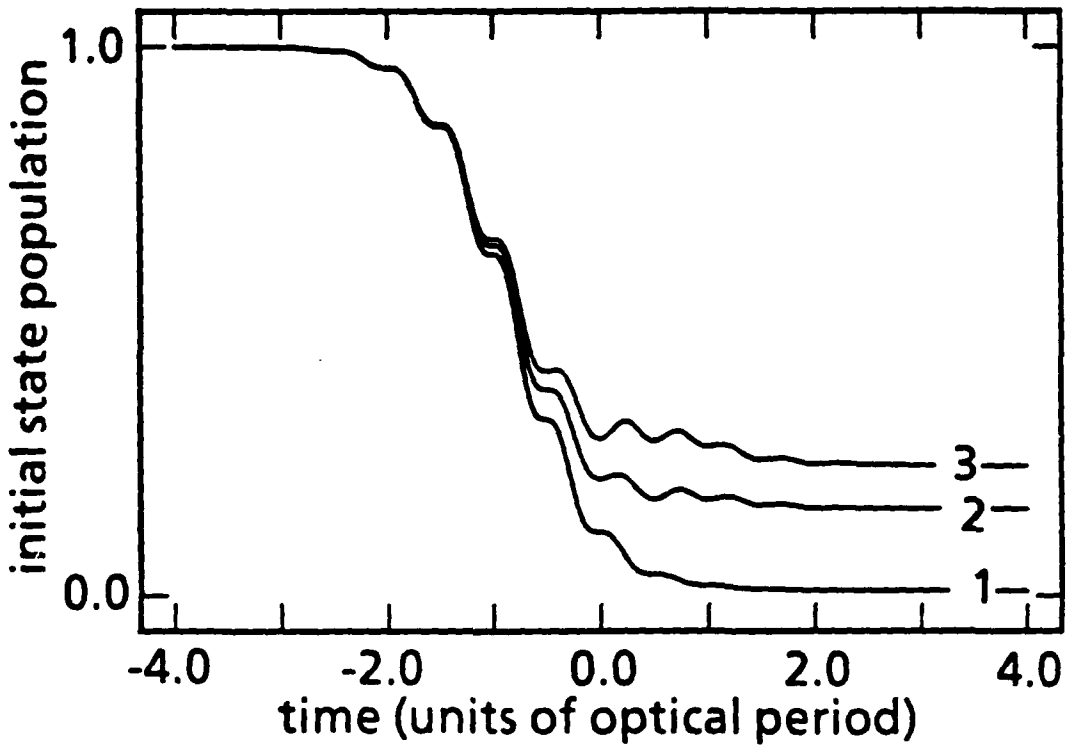

Fig. 4.2. Population in initial state $|g_0>$ during the laser pulse. The curves are generated by numerically integrating Schrödinger's equation on the basis set of Fig. 4.1. The curves are labeled by the number of bound states $|g>$ present in the numerical integration. The intensity of the laser pulse and all other parameters are constant for the three curves.

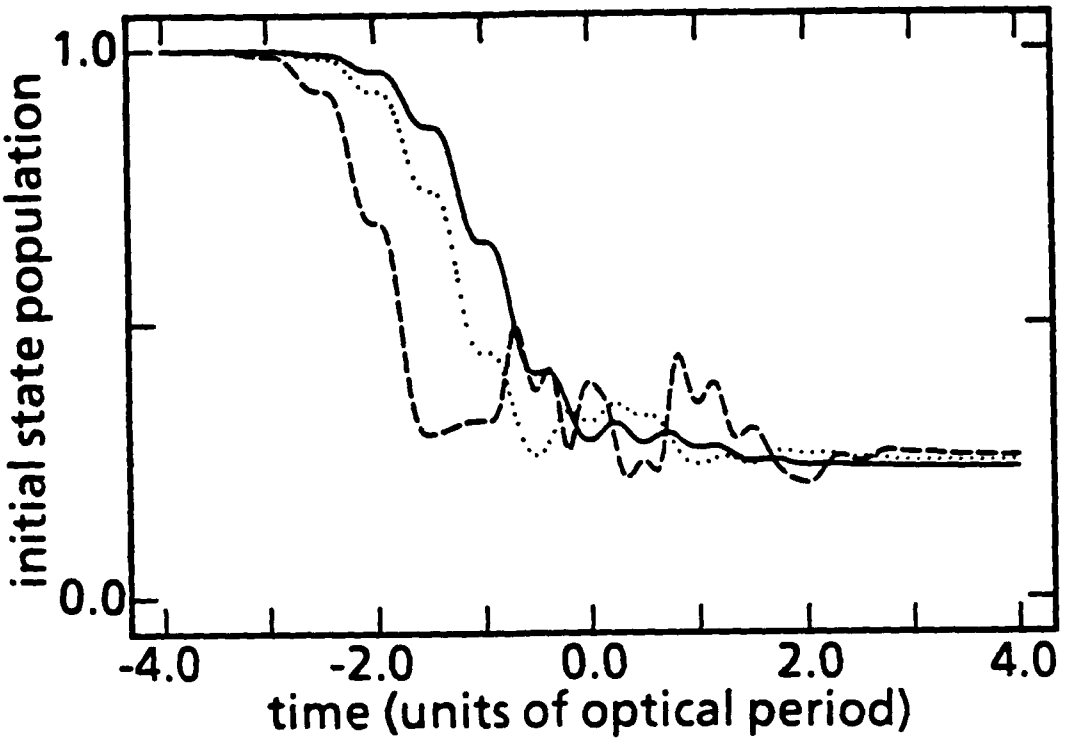

Fig. 4.3. Population in the initial state $|g_0>$ during the laser pulse. The curves were generated by numerically integrating the equations of motion. The solid curve shows the evolution of $|g_0>$ with the same intensity I_0 used in Fig. 4.2. The dotted curve shows the evolution of $|g_0>$ at intensity $2 \cdot I_0$. The dashed curve shows the evolution of $|g_0>$ at intensity $10 \cdot I_0$.

Section 4.3 Theory in the Rotating-wave Approximation

In this section we will describe an approximate solution of Eq. (4.1) that employs the rotating-wave approximation (RWA). The method is a generalization of a method discussed in reference 5. The strategy will be to eliminate the infinite set of unbound states $|E>$ from the set of equations leaving a finite number of equations containing only the variables of the unbound states $|g>$. The theoretical predictions will then be compared to the numerical solutions of Schrödinger's equation.

The major difficulty in simplifying and solving Eq. (4.1) is the assumption that the laser pulse has an arbitrary shape f(t). It will be assumed that f(t) is smoothly varying, but no other assumptions are made. This generality is particularly important in this study. In our numerical examples, f(t) will always be Gaussian.

Next, let us rewrite Eq. (4.1) in the RWA. To do this the $\sin(\omega t)$ in Eq. (4.1) is expanded in complex exponentials, and the rapidly oscillating terms are discarded to yield:

$$\frac{da_E(t)}{dt} = \sum_g V_{Eg}\, a_g(t)\, \exp(-i\omega_g t)\exp(i\omega_E t)\exp(-i\omega t) f(t)\ , \qquad (4.2a)$$

$$\frac{da_g(t)}{dt} = -\sum_E V_{Eg}\, a_E(t)\, \exp(i\omega_g t)\exp(-i\omega_E t)\exp(i\omega t) f(t)\ . \qquad (4.2b)$$

In Eq. (4.2), the variables are the same as those in Eq. (4.1). In order to solve Eq. (4.2) two more appproximations will be made. With these two new assumptions, it will be possible to derive exact solutions to Eq. (4.2) in several special cases.

The two further assumptions are the following: it is assumed that the ionization continuum is flat, i.e. V_{Eg} is independent of E, and second it is assumed that the continuum has no upper or lower bound. As one consequence, the width in energy of the ionization continuum is infinite, rather than the finite energy width drawn in Fig. 4.1.

With these two approximations, the next step is to eliminate the unbound states $|E>$ from Eq. (4.2). Formally integrating Eq. (4.2) for the amplitudes $a_E(t)$, and substituting $a_E(t)$ into Eq. (4.2b) yields

$$\frac{da_g}{dt} =$$

$$-\sum_{g'}\int_{-\infty}^{t} dt' \left\{ \sum_{E} V_{Eg} V_{Eg'} \exp[\, i(\omega_{E0}-\omega)(t'-t)\,] \right\} \exp(i\omega_g t)\exp(-i\omega_g t')a_{g'}(t')\, f(t')\, f(t), \tag{4.3}$$

where $\hbar\omega_0$ is the energy of the initial state $|g_0>$, and $\omega_{E0} = \omega_E - \omega_0$. Now, because of the second assumption above, the expression in the braces { } can be summed to yield $2\Gamma_g\, \delta(t' - t)V_{Eg'}/V_{Eg}$, where $2\Gamma_g$ is the Fermi golden rule rate of ionization of the state $|g>$ into the ionization continuum $|E>$. The equation is simpler in the Schrödinger picture. The Schrödinger picture variables $c_g(t)$ are related to $a_g(t)$ by,

$$c_g(t) = a_g(t)\exp(-i\omega_g t)\ . \tag{4.4}$$

With these new variables, and with the delta-function described above, Eq. (4.3) reduces to a very simple set of coupled equations:

$$\frac{dc_g(t)}{dt} + i\omega_g c_g(t) = -\Gamma_g f^2(t)\sum_{g'}\frac{V_{Eg'}}{V_{Eg}} c_{g'}(t)\ . \tag{4.5}$$

In Figures 4.4 and 4.5 we compare the results of the theory Eq. (4.5)

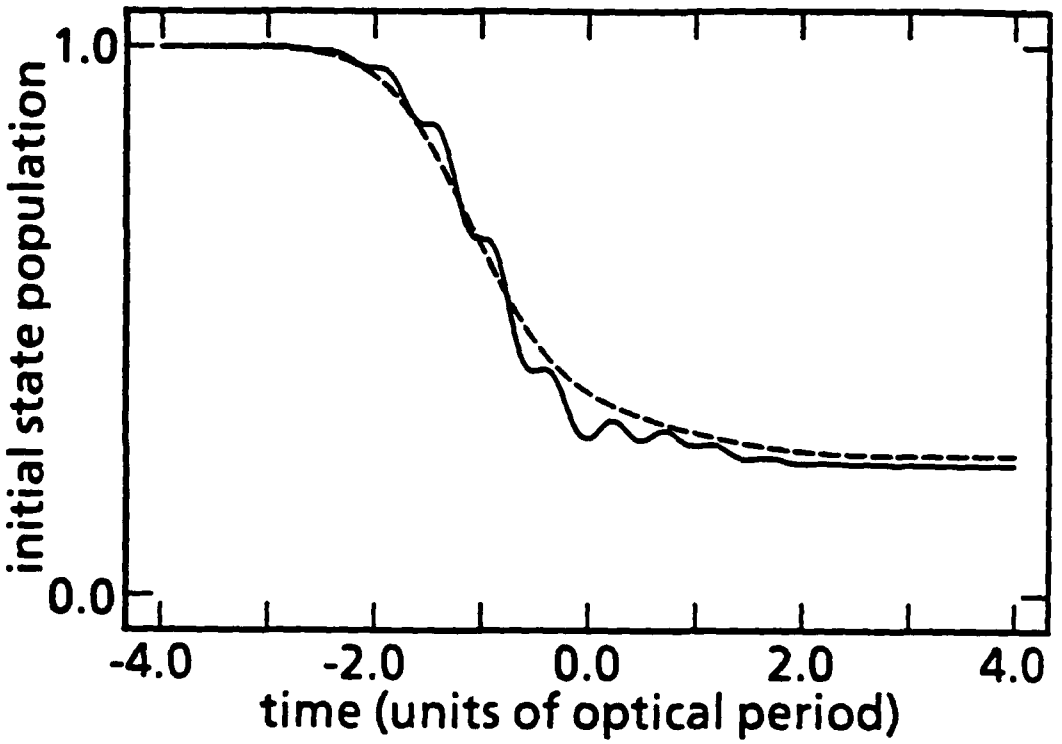

Fig. 4.4. Population in the initial state $|g_0>$ during the laser pulse. The solid curve was generated by numerically integrating the equations of motion. The dashed curve shows the predictions of the theory in the RWA. The pulse intensity was I_0, and 3 bound states were present, $|g_0>$, $|g_1>$, and $|g_2>$.

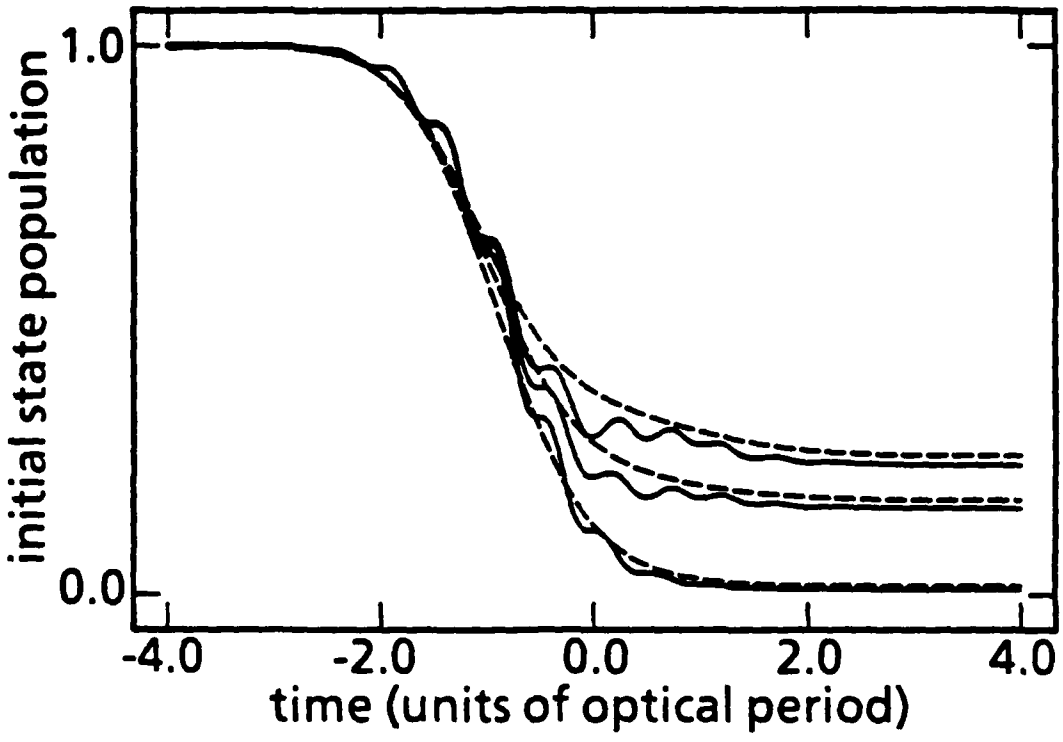

Fig. 4.5. Population in the initial state $|g_0>$ during the laser pulse. The solid curves were generated by numerically integrating the equations of motion. The dashed curves represent the theoretical predictions. The conditions were identical to those of Fig. 4.4, except that the number of bound states present was varied from one to three as in Fig. 4.2.

with the predictions of Schrödinger's equation. The theoretical equations are numerically integrated with a Gaussian pulse shape for f(t). Withrectangular pulse shapes it is possible to solve Eq. (4.5) analytically. For a variety of conditions, the theory qualitatively agrees with the predictions of Schrödinger's equation.

Section 4.4 Population Trapping

When the bound states $|g>$ are degenerate in energy, then the Eq. (4.5) may be solved exactly with arbitrary pulse shape f(t). The calculation shows, surprisingly, that population is trapped in the initial state $|g_0>$ for laser pulses of arbitrary duration. In other words the trapping is permanent.

Assume that the states $|g>$ are degenerate and without loss in generality set the initial state energy to zero : $\omega_0 = \omega_1 = \cdots = 0$. With the change of variables $D(t) = \Sigma V_{Eg} c_g(t)$, Eq. (4.5) becomes

$$\frac{d}{dt} c_g(t) = - \Gamma_g f^2(t)\, D(t) / V_{Eg} \quad , \tag{4.6}$$

and

$$\frac{d}{dt} D(t) = - \Big(\sum_{g'} \Gamma_{g'}\Big) f^2(t)\, D(t) \quad . \tag{4.7}$$

The initial condition of D is $D(-\infty) = V_{E0}$. This arises from the initial state $c_0(t)$, which satisfies $c_0(-\infty) = 1$. Solving for D(t) and substituting it into Eq. (4.6) yields

$$\frac{d}{dt} c_g(t) = - \Gamma_g f^2(t)\, \frac{V_{E0}}{V_{Eg}} \exp\left[- \int_{-\infty}^{t} dt' \Big(\sum \Gamma_{g'}\Big) f^2(t') \right] \quad , \tag{4.8}$$

which may be integrated immediately to get

$$c_g(t) = c_g(-\infty) + \frac{\Gamma_g}{(\sum \Gamma_{g'})} \frac{V_{E0}}{V_{Eg}} \left\{ \exp\left[-\int_{-\infty}^{t} dt' \, (\sum \Gamma_{g'}) \, f^2(t') \right] - 1 \right\} . \quad (4.9)$$

The solution is more transparent if we assume that the pulse is rectangular in shape, and turns on abruptly at t=0. Then the probability amplitude of the initial state is,

$$c_0(t) = 1 + \frac{\Gamma_0}{(\sum \Gamma_{g'})} [\exp(-(\sum \Gamma_{g'}) t) - 1] \quad . \quad (4.10)$$

Equation (4.10) implies that as long as the FGR ionization rates ($2\Gamma_g$) for transitions from $|g>$ to the ionization continuum are non-zero, then $\Gamma_0/\Sigma(\Gamma_g)$ is less than 1 and population will be permanently trapped in the initial state $|g_0>$.

Section 4.5 Non-degenerate States

Equation (4.5) can also be easily solved analytically for non-degenerate states $|g>$, provided that the laser pulse is rectangular in shape. In this section we will describe the solution in the simplest case (two bound states) and assume that the pulse is rectangular and turns on at t=0. Again the initial state energy $\hbar\omega_0$ is set to zero and the energy of $|g_1>$ will be denoted $\delta\omega = \omega_1 - \omega_0 = \omega_1$.

One important physical point we want to emphasize in this section is that the ionization exhibits qualitatively different behavior in two limits. In the weak field limit when the FGR rate $2\Gamma_0$ is so small that $\delta\omega > 2\Gamma_0$, then the initial state $|g_0>$ ionization closely follows the FGR exponential decay law $\exp(-2\Gamma_0 t)$ with or without the presence of the state $|g_1>$. In the

strong field limit, when $\delta\omega < 2\Gamma_0$, then the ionization rate is strongly inhibited in comparison to the FGR rate. We are assuming that $\Gamma_0 = \Gamma_1$. The rules are slightly modified when this condition is not met, but unless $\Gamma_1 << \Gamma_0$, it remains true that in the strong field limit, ionization is strongly inhibited in comparison to the FGR rate.

The solution of Eq. (4.5) in this limit (two bound states with rectangular laser pulse) is straightforward. With initial conditions $c_0(0)=1$ and $c_1(0)=0$, the solution for the probability amplitude of the initial state $c_0(t)$ is

$$c_0(t) = \frac{1}{A_2 - A_1}\left\{ (A_2 + \Gamma_0)\exp(A_1 t) - (A_1 + \Gamma_0)\exp(A_2 t)\right\} \quad , (4.11a)$$

$$A_{1,2} = -\Gamma - i\delta\omega/2 \pm \left[\Gamma^2 - (\delta\omega/2)^2 + i\,\delta\omega\,\Delta \right]^{1/2}. \qquad (4.11b)$$

Here $\Gamma = (\Gamma_0 + \Gamma_1)/2$ and $\Delta = (\Gamma_1 - \Gamma_0)/2$. The solution is particularly transparent when $\Delta = 0$. In that case, $A_{1,2} = -\Gamma - i\delta\omega/2 \pm (\Gamma^2 - (\delta\omega/2)^2)^{1/2}$ and it is immediately apparent why the ionization behavior is so different in the two limits $\delta\omega/2 > \Gamma_0$ and $\delta\omega/2 < \Gamma_0$. Consider for example the strong field case, $\delta\omega/2 < \Gamma_0$. Expanding the square root of A to order $((\delta\omega/2)/\Gamma)^4$ yields for $c_0(t)$:

$$c_0(t) = \exp(i\delta\omega t/2)\left\{ \frac{A_2 + \Gamma_0}{A_2 - A_1}\exp(-\frac{\delta\omega^2}{8\Gamma} t) - \frac{A_1 + \Gamma_0}{A_2 - A_1}\exp(-2\Gamma t)\exp(\frac{\delta\omega^2}{8\Gamma} t)\right\} \qquad 4.12)$$

Recall that $c_0(t)$ is the physical probability amplitude of the initial state. Thus $c_0(t)$ has a term with a decay rate that apprcaches zero as Γ approaches infinity. Moreover, the amplitude of this term is proportional to $(A_2 + \Gamma)/(A_2 - A_1)$, which approaches a non-zero constant (1/2) as Γ approaches infinity. Thus, if $\delta\omega/2 < \Gamma$, then increasing the intensity of the

pulse (keeping its duration fixed) increases the amount of population remaining in the initial state at the end of the pulse. This is true for a rectanglar pulse of any duration: the population remaining in $|g_0>$ at the end of the pulse, $|c_0|^2$, approaches 1/4 in the limit of high field intensity. The general behavior is also apparent in the numerical solution of Eq. (4.1) with Gaussian pulse shapes, as shown in Fig. 4.3.

Section 4.6 Theory Without the RWA

In the previous sections, a theory of ionization was developed in the rotating-wave approximation (RWA). The theory had the virtue of simplicity, but diverged noticably from the solutions of Schrödinger's equation that it was supposed to model. In particular, the theory's prediction of the population in the initial state at the end of the pulse was consistently wrong by 10%.

The question arises then, whether the failure was due to the RWA, or due to some other assumption made in the derivation of Eq. (4.5). In this section it will be shown that the theory may be developed without making the RWA. The new theory uses the same assumption in its derivation as the simpler theory, with the exception of the RWA. The new theory will give correct predictions of the population remaining in the initial state at the end of the pulse, suggesting that most of the failure evident in the RWA version of the theory was due to the RWA.

The derivation of the theory will be very similar to derivation of the RWA version of section 4.3. The first step, again, is to integrate Eq. (4.1a)

formally and substitute it into Eq. (4.1b) in an effort to eliminate the variables associated with the ionization continuum $|E>$. To simplify the algebra, a change of variables similar Eq. (4.4) is used,

$$c_g(t) = V_{Eg} \exp(-i\omega_g t)\, a_g(t). \qquad (4.13)$$

Equation (4.1) becomes:

$$\frac{dc_g}{dt} + i\omega_{g0} c_g = -\sum_{g'} \int_{-\infty}^{t} dt' \left\{ \sum_E V_{Eg}^2 \exp(i(\omega_{E0}-\omega)(t'-t)) \right\} c_{g'}(t')\, f(t')\, f(t)$$

$$+ \sum_{g'} \int_{-\infty}^{t} dt' \left\{ \sum_E V_{Eg}^2 \exp(i(\omega_{E0}+\omega)t') \exp(-i(\omega_{E0}-\omega)t) \right\} c_{g'}(t')\, f(t')\, f(t)$$

$$+ \sum_{g'} \int_{-\infty}^{t} dt' \left\{ \sum_E V_{Eg}^2 \exp(i(\omega_{E0}-\omega)t') \exp(-i(\omega_{E0}+\omega)t) \right\} c_{g'}(t')\, f(t')\, f(t)$$

$$- \sum_{g'} \int_{-\infty}^{t} dt' \left\{ \sum_E V_{Eg}^2 \exp(i(\omega_{E0}+\omega)t') \exp(-i(\omega_{E0}+\omega)t) \right\} c_{g'}(t')\, f(t')\, f(t). \qquad (4.14)$$

The next step is to assume that $c_g(t)$ may approximated by a truncated Fourier series:

$$c_g(t) = c_{g0}(t) + \sum_{n=1}^{2} c_{gn}^{+}(t) \exp(in\omega t) + \sum_{n=1}^{2} c_{gn}^{-}(t) \exp(-in\omega t). \qquad (4.15)$$

The new variable $c_{gn}(t)$ will be substituted into Eq. (4.14) and then the coefficients of $\exp(in\omega t)$ are equated. This is similar to the well-known approach in which the states are expanded in a full Fourier series. However, a new approximation is required, one that was not discussed in section 4.3. The new approximation is the slowly-varying envelope approximation (SVEA). It will be assumed that $c_{gn}(t)f(t)$ is slowly varying

formally and substitute it into Eq. (4.1b) in an effort to eliminate the variables associated with the ionization continuum $|E>$. To simplify the algebra, a change of variables similar Eq. (4.4) is used,

$$c_g(t) = V_{Eg} \exp(-i\omega_g t)\, a_g(t). \qquad (4.13)$$

Equation (4.1) becomes:

$$\frac{dc_g}{dt} + i\omega_{g0} c_g = -\sum_{g'} \int_{-\infty}^{t} dt' \left\{ \sum_E V_{Eg}^2 \exp(i(\omega_{E0}-\omega)(t'-t)) \right\} c_{g'}(t')\, f(t')\, f(t)$$

$$+ \sum_{g'} \int_{-\infty}^{t} dt' \left\{ \sum_E V_{Eg}^2 \exp(i(\omega_{E0}+\omega)t') \exp(-i(\omega_{E0}-\omega)t) \right\} c_{g'}(t')\, f(t')\, f(t)$$

$$+ \sum_{g'} \int_{-\infty}^{t} dt' \left\{ \sum_E V_{Eg}^2 \exp(i(\omega_{E0}-\omega)t') \exp(-i(\omega_{E0}+\omega)t) \right\} c_{g'}(t')\, f(t')\, f(t)$$

$$- \sum_{g'} \int_{-\infty}^{t} dt' \left\{ \sum_E V_{Eg}^2 \exp(i(\omega_{E0}+\omega)t') \exp(-i(\omega_{E0}+\omega)t) \right\} c_{g'}(t')\, f(t')\, f(t). \qquad (4.14)$$

The next step is to assume that $c_g(t)$ may approximated by a truncated Fourier series:

$$c_g(t) = c_{g0}(t) + \sum_{n=1}^{2} c_{gn}^{+}(t) \exp(in\omega t) + \sum_{n=1}^{2} c_{gn}^{-}(t) \exp(-in\omega t). \qquad (4.15)$$

The new variable $c_{gn}(t)$ will be substituted into Eq. (4.14) and then the coefficients of $\exp(in\omega t)$ are equated. This is similar to the well-known approach in which the states are expanded in a full Fourier series. However, a new approximation is required, one that was not discussed in section 4.3. The new approximation is the slowly-varying envelope approximation (SVEA). It will be assumed that $c_{gn}(t)f(t)$ is slowly varying

in the following sense. An integration by parts of certain terms in Eq. (4.14) goes as follows:

$$\int_{-\infty}^{t} dt' \left\{ \sum_E V_{Eg}^2 \exp(i(\omega_{E0}+\omega)(t'-t) \right\} c_g(t')\, f(t') \;=\; c_g(t) f(t) \sum_E \frac{V_{Eg}^2}{i(\omega+\omega_{E0})} -$$

$$+ \int_{-\infty}^{t} dt' \left\{ \sum_E \frac{V_{Eg}^2}{i(\omega+\omega_{E0})} \exp(i(\omega_{E0}+\omega)(t'-t) \right\} \frac{d}{dt'} (c_g(t')\, f(t')) \;. \quad (4.16)$$

The SVEA implies that the integral on the right-hand side of Eq. (4.16) is negligible due to the negligible time derivatives of f(t) and $c_{gn}(t)$. With this approximation, and with the methods of section 4.3, Eq. (4.14) can be greatly simplified. Substituting the Fourier series Eq. (4.15) into Eq. (4.14) yields:

$$\frac{d}{dt} \begin{bmatrix} c_{g0}(t) \\ c_{g2}^{+}(t) \\ c_{g2}^{-}(t) \end{bmatrix} = \begin{bmatrix} (-i\omega_g)\, c_{g0} \\ (-i\omega_g - 2i\omega)\, c_{g2}^{+} \\ (-i\omega_g + 2i\omega)\, c_{g2}^{-} \end{bmatrix} + f^2(t) \begin{bmatrix} (-\Gamma_g + i\Omega_{1g}) & (-i\Omega_{1g}) & (\Gamma_g) \\ (-i\Omega_{1g}) & (i\Omega_{1g} + i\Omega_{3g}) & (0) \\ (\Gamma_g) & (0) & (-\Gamma_g + i\Omega_{-3g}) \end{bmatrix} \begin{bmatrix} \sum_{g'} c_{g'0} \\ \sum_{g'} c_{g'2}^{+} \\ \sum_{g'} c_{g'2}^{-} \end{bmatrix} \quad (4.17)$$

In Eq. (4.17), the frequency shifts Ω arise from terms on the right hand side of Eq. (4.16):

$$\Omega_{ng} \;=\; -\sum_E \frac{V_{Eg}^2}{(n\omega+\omega_{E0})} \;. \quad (4.18)$$

Figures 4.6 and 4.7 show a comparison of a numerical integration of Schrödinger's equation with a numerical integration of Eq. (4.17). The theory is compared to Schrödinger's equation (Eq. (4.1)) for the three cases

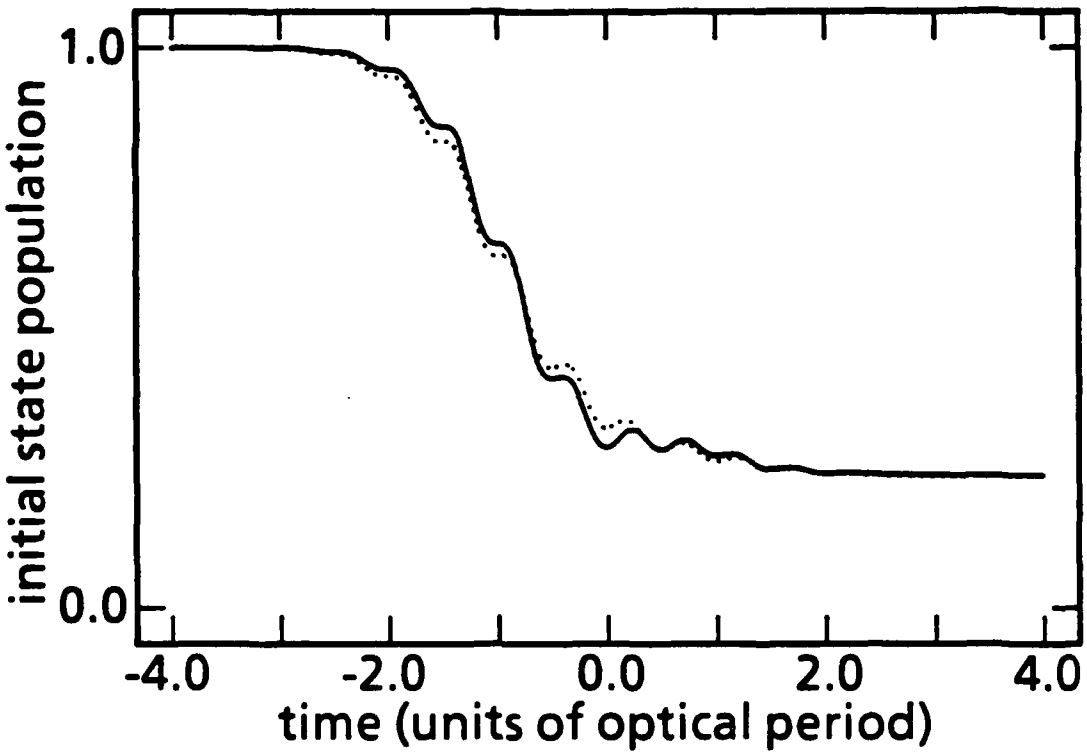

Fig. 4.6. Population in the initial state $|g_0>$ during the laser pulse, under conditions identical to those of Fig. 4.4. Here the dotted curve represents the theoretical predictions with three bound states present. The solid curve was generated by numerically integrating the equations of motion.

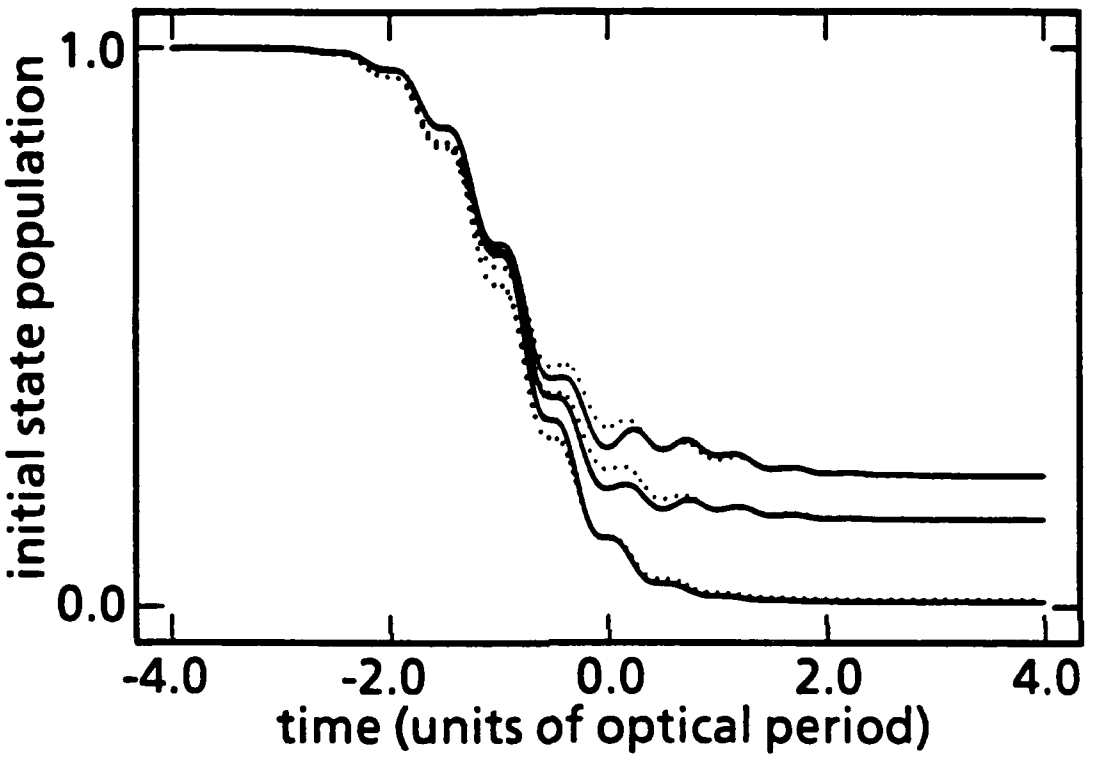

Fig. 4.7. Population in the initial state $|g_0>$ during the laser pulse, under conditions identical to those of Fig. 4.4. The solid curves were generated by numerically integrating the equations of motion. The dotted curves represent the theoretical predictions with 1, 2, and 3 bound states present as in Fig. 4.2.

of section 4.2, shown in Fig. 4.2. The agreement between theory Eq. (4.17) and Schrödinger's equation is superior to the RWA results, although the agreement is not quantitative.

Section 4.7 Conclusion

It is apparent from the numerical solutions with Gaussian pulses, and from the solutions Eq. (4.9) and Eq. (4.11), that the inhibition of ionization is not due to a special choice of pulse shapes, and atomic dipole moments. Rather, we have seen for a variety of pulse shapes, dipole moments and energy level spacings, that the ionization may be strongly inhibited in comparison to what is implied by the FGR ionation rate.

The population trapping and other modifications of FGR were found to be due to states of the same parity as the initial state ($|g_1\rangle$, $|g_2\rangle$, ...) which recapture population from the ionization continuum during the excitation. Significant population must actually enter these states for the inhibition effects to be significant. If no population were recaptured by the states $|g_1\rangle$, $|g_2\rangle$, ... , then the states could be discarded from Eq. (4.1) and analysis of Eq. (1) would yield the usual FGR predictions. I et $|\Psi_c(t)\rangle$ be the coherent superposition of the bound states $\Sigma\, c_g(t)\, |g\rangle$, and consider Eq. (4.1a) (in the Schrödinger picture) for the probability amplitude of a typical unbound state $|E\rangle$:

$$dc_E(t)/dt + i\omega_E c_E(t) = i\langle E | (e/mc\hbar)\, \mathbf{p}\cdot\mathbf{A}\, |\Psi_c(t)\rangle. \qquad (4.19)$$

In the examples of inhibited ionization studied here, population returns to the bound states with just the right phase so that the right hand side of

Eq. (4.19) is small in comparision to the matrix element used to calculate the Fermi golden rule rate: $<E \mid (e/mc\hbar)\ \mathbf{p}\cdot\mathbf{A} \mid c_g(t)\ g_0>$. In other words, the superposition state $|\Psi_c(t)>$ exhibits a reduced ionization cross section in comparison to the FGR prediction for the initial state $c_g(t) \mid g_0>$. The non-energy conserving aspect of these transitions is easily expained by the $\Delta E \Delta t$ arguments of chapter 2, in which apparently out of resonance excited states received population because the finite Δt of the laser pulse made ΔE non-zero. In terms of Fig. 4.1 this means simply that both the transition denoted by the solid arrow, and the transition denoted by the dashed arrow are resonant transitions.

The theory was developed to describe ionization under extreme conditions, in which the laser pulse intensity was sufficient to ionize the atom in a few cycles of the field. Such conditions arise, for example, in the study of the above-threshold ionization of atomic hydrogen. Under these conditions, much of the ionization takes place during the turn-on of the laser pulse. For this reason it was important to develop a theory capable of handling physical (eg. Gaussian) laser pulses. Despite the extreme conditions, the theory in its simplest (RWA) form qualitatively predicted the general features of population trapping and inhibited FGR observed in the numerical integration of Schrödinger's equation.

In order to understand the remaining discrepency between theory and numerical integration, a more sophisticated version of the theory was developed which did not employ the RWA. The more sophisticated theory gave superior agreement with the numerical integration by correctly predicting the population in the initial state at the end of the laser pulse.

As a result we were able to demonstrate in a variety of examples the partial failure of the RWA.

References

1. E. Kyrölä and J. H. Eberly, J. Chem. Phys. **82** (4), 1841 (1985).

2. M. V. Fedorov and A. M. Movsesian, J. Opt. Soc. Am. B **6**, 928 (1988).

3. E. Arimondo and G. Orriols, Nuovo Cimento Lett. **17**, 333 (1976); H. R. Gray, R. M. Whitley, and C. R. Stroud, Jr., Opt. Lett. **3**, 218 (1978); P. L. Knight, Opt. Comm. **31**, 148 (1979); P. E. Coleman and P. L. Knight, J. Phys. B **15**, 1235 (1982); P. M. Radmore and P. L. Knight, Phys. Lett. **102a**, 180 (1984).

4. D. A. Cardimona, M. G. Raymer and C. R. Stroud Jr., J. Phys. B **15**, 63 (1982); E. Kyrölä and J. H. Eberly, J. Chem. Phys. **82** (4), 1841 (1985).

5. J. J. Yeh, C. M. Bowden, and J. H. Eberly, J. Chem. Phys. **76**, 5936 (1982).

6. J. Parker and C. R. Stroud Jr., Phys. Rev. A **35**, pp. 4226-4237 (1987).

CHAPTER V

GENERALIZATION OF THE KELDYSH THEORY OF ABOVE-THRESHOLD IONIZATION

Section 5.1 Introduction

The first experimental observation of above-threshold ionization (ATI) a decade ago[1] has stimulated a great deal of work to develop the theory of the process by which an electron absorbs several extra photons beyond the minimum needed to ionize the atom to which it was initially bound. In some experiments more than 30 peaks have been seen in the spectrum of the electrons indicating the absorption of this many excess photons by the electron. The theory is complicated by the fact that ATI is fundamentally a high order multiphoton process, by the fact that ATI does not seem to be well-described by perturbative theories, and by the fact that most ATI experiments have been carried out in xenon, an element with a rather complicated energy level structure. Nevertheless, a certain class of theories has met with some success in modeling ATI ionization cross sections. The most widely used theory was proposed by L. V. Keldysh[2] in 1965, and later modified by several authors[3]. The modified theory is now sometimes called the Keldysh-Faisal-Reiss (KFR) theory.

At present, work is going on to extend ATI experiments into the femtosecond regime and to atoms other than the noble gases[4]. Recently J. Javanainen and J. H. Eberly[5] have compared several Keldysh models of the KFR type with the results of a numerical integration of a one-

dimensional hydrogen atom, finding poor agreement between theory and numerical experiment. In this chapter a variant of the Keldysh theory appropriate for short pulses is developed and tested by comparing its predictions with a direct numerical integration of the full three-dimensional Schrödinger's equation.

As discussed in he previous two chapters, the numerical integration of Schrödinger's equation reveals several new intense-field effects. These effects complicated both the development of the theory, and the effort to verify the theory numerically. In order to use the numerical integration as a test of Keldysh theory it is necessary to understand these effects. The first phenomenon is the inhibition of ionization due to coherent population trapping, which we discussed in chapter IV. Second, we find that the slowly varying population approximation (SVPA) fails in this example of ATI. The failure of the SVPA will be discussed in section 5.4. The SVPA is used in the derivation of several theories of ATI, and in the derivation of Fermi's Golden Rule.

In section 5.3 we will present a rigorous derivation of a variation of Keldysh theory beginning from Schrödinger's time-dependent equation. In section 5.3 we compare the proposed theory with the results of the numerical integration of Schrödinger's equation.

Several theories resembling Keldysh's original proposal have been discussed in the literature[3,6,7]. The best known modification to Keldysh's original proposal is the KFR theory. These theories are sometimes called Volkoff final-state theories, for reasons that are explained in section 5.5. Here we adopt the more common practice[5] of calling them "theories of the

Keldysh type". The theory developed in this paper yields formulas closely resembling the Keldysh formulas, although the derivation is very different. In section 5.5 we compare the conventional (KFR) Keldysh predictions with the results of the numerical integration, and discuss the relationship between our theory and the conventional Keldysh theory.

Section 5.2 Review of Previous Results

In order to formulate and test numerically theories of the Keldysh type, we will rely on our experience numerically integrating Schrödinger's equation (chapter III) and on the theoretical results of chapter IV. In chapter IV a population trapping phenomenon was analyzed that may be characterized as an intense-field modification of Fermi's golden rule (FGR). In the following sections we will see that the effect will modify the formulation of Keldysh-type theories just as it modified FGR.

Let us begin by reviewing Fig. 3.3b, which shows (solid line) the population in the initial state ($n=3$, $\ell=2$, $m=2$) during the numerical integration of Schrödinger's equation. A seven femtosecond Gaussian-shaped laser pulse, peaking at $2 \cdot 10^{14} W/cm^2$, was used. Despite the exceptionally high intensity of the laser field, the ionization appeared to be inhibited. This inhibition of ionization was characterized as an intense-field modification of Fermi's golden rule (FGR). For comparison, the FGR prediction was also plotted in Fig. 3.3(b) (dashed line). The FGR rate of exponential decay was calculated by assuming a single $\ell=2$ bound state and a single $\ell=3$ continuum of unbound states. The simple FGR

calculation also predicted complete ionization at intensities an order of magnitude lower than the 2.2×10^{14} W/cm^2 peak intensity actually used.

The origin of the inhibited ionization was easily demonstrated by removing basis states from the basis set during the integration. When the states ($n=4$, $\ell=2$, $m=2$) and ($n=5$, $\ell=2$, $m=2$) were removed from the basis set, then the initial state decayed nearly as predicted by FGR. Absorption of population by the $n=4$ and 5 states (via the $\ell=3$ continuum of unbound states) then in effect inhibited ionization.

To describe mathematically how population trapping modifies the excitation, consider the equation of motion of a state $|n>$ in the first ($\ell=3$) ionization peak. Let Ψ_i be the superposition of the three $\ell=2$ bound states, of principal quantum number 3, 4, and 5. Then the coupling of the ($\ell=3$) state $|n>$ to the initial ($\ell=2$) coherent state Ψ_i is governed by

$$i\hbar\frac{da_n}{dt} = \exp(i\omega_n t)\left[-\frac{e}{mc}A_z(t)\right]<n|\,p_z\,|\Psi_i(t)> \quad . \qquad (5.1)$$

Here a_n is the probability amplitude of a state $|n>$ at the center of the 1st ($\ell=3$) ionization peak and $A_z(t)$ is the field potential. A numerical calculation demonstrates that the quantity $<n|\,p_z\,|\Psi_i(t)>$ falls rapidly to near zero as the pulse peaks in intensity ($t = 0\pm 1.5T_\omega$). Population flows into the $n=4$ and 5 bound states ($\ell=2$) in such a way as to effectively turn off the transition from the $\ell=2$ bound states to the $\ell=3$ unbound states. In other words, a ($\ell=2$) coherent state Ψ_i is generated that exhibits a greatly reduced ionization cross section in comparison to the FGR prediction. Numerically it is found, by redoing the numerical integration described in chapter III, that the effect seems to occur naturally at intensities both higher (9×10^{14} W/cm^2) and lower (5×10^{13} W/cm^2) than in the example to

be discussed in this chapter (2.2×10^{14} W/cm^2). In fact, at 9×10^{14} W/cm^2 more population remained in the n=3 initial state at the end of the pulse than at the end of a 5×10^{13} W/cm^2 pulse.

We have reviewed this problem because Keldysh scattering theory calculations usually assume that population remains in the initial atomic state during the excitation. Our formulation will use as the initial state $|\Psi_i(t)>$ defined above.

Recently, J. H. Eberly and J. Javanainen[10], and B. Sundaram and L. Armstrong[11] have discussed the role of excited bound states play in modifying the ATI peak shapes. Inhibition of ionization and population trapping due to coherences among two or more bound states has been extensively studied both in the theory of two-color ionization[12] and in the theory of one-color ionization[13].

Section 5.3 Keldysh Theory From Time-Dependent Quantum Mechanics

A general theory of the Keldysh type can be derived in a few steps from the time-dependent Schrödinger's equation. The derivation is aided by experience with the basis state method described above and in chapter III.

The first step is to break the wave function into two parts, the initial state Ψ_i defined above, and the final state Ψ_f. By Ψ_f we mean the coherent superposition of all positive energy states. This subset of the complete set of states (shown in truncated form in Fig. 3.1) was chosen because experience with the numerical integration indicated that discarded states play little direct role in the excitation. Then

Schrödinger's equation is

$$i\hbar \frac{d\Psi_f}{dt} = (H_0 + H_{int}(t))\Psi_f + (H_0 + H_{int}(t) - i\hbar \frac{d}{dt})\Psi_i \qquad (5.2)$$

where H_0 is the atomic Hamiltonian and $H_{int}(t)$ is $-e\mathbf{p}\cdot\mathbf{A}/mc + e^2\mathbf{A}\cdot\mathbf{A}/2mc^2$.

Now writing the final state as $\Sigma\, c(\mathbf{p},t)\,|\mathbf{p}>$, a superposition of plane wave states, and taking the projection of Eq. (5.2) on $<\mathbf{p}|$ yields,

$$i\hbar \frac{d\,c(\mathbf{p},t)}{dt} = <\mathbf{p}|H_0|\Psi_f> + (-\frac{e}{mc}\mathbf{A}\cdot\mathbf{p} + \frac{e^2}{2mc^2}\mathbf{A}\cdot\mathbf{A})\,c(\mathbf{p},t) + <\mathbf{p}|H_0 + H_{int} - i\hbar\frac{d}{dt}|\Psi_i(t)>. \qquad (5.3)$$

The effect of taking the projection of the equation on $<\mathbf{p}|$ was to replace the canonical momentum operator $\mathbf{p}$ in the interaction Hamiltonian H_{int} with a c-number $\mathbf{p}$. Henceforth $\mathbf{p}$ will denote the c-number $\mathbf{p}$. At the end of the pulse, $\mathbf{p}$ is the physical (kinetic) momentum of the ionized electron, sinse the kinetic momentum is $\mathbf{p} - (e/c)\mathbf{A}(t)$ and we assume that the vector potential $\mathbf{A}(t)$ goes to zero at the end of the pulse.

The most important approximation in the derivation will be called the "plane-wave approximation." By the plane-wave approximation we mean that

$$<\mathbf{p}|H_0|\Psi_f> = <\mathbf{p}|\frac{\mathbf{p}\cdot\mathbf{p}}{2m} + V(r)|\Psi_f> \approx \frac{\mathbf{p}\cdot\mathbf{p}}{2m}<\mathbf{p}|\Psi_f> . \qquad (5.4)$$

The assumption is then that the Coulomb potential perturbs the final states insignificantly . The plane-wave approximation is closely related to the zeroth order Born approximation. It is well known[14] that the first order correction to the zeroth order Born approximation is small in transitions

from an initial bound state of quantum number ℓ to final unbound states of quantum number $\ell + 1$.

With this approximation, Eq. (5.3) may be immediately integrated to give ,

$$|c(\mathbf{p},t)|^2 = \left| \frac{1}{\hbar} \int_{-\infty}^{t} dt' \exp\left[\frac{i}{\hbar} \int_{-\infty}^{t'} dt'' \left(\frac{\mathbf{p}\cdot\mathbf{p}}{2m} + H_{int}(t'') \right) \right] \langle \mathbf{p} | H_0 + H_{int} - i\hbar \frac{d}{dt'} | \Psi_i(t') \rangle \right|^2 . \tag{5.5}$$

In the interaction Hamiltonian of Eqs. (5.2 - 5.5) we have kept the $\mathbf{A}\cdot\mathbf{A}$ term even though a simple transformation might have removed it from the dipole-approximation Schrödinger's equation at the start. In the dipole approximation, the $\mathbf{A}\cdot\mathbf{A}$ term has no effect on the ATI spectrum. If Ψ is a solution of the Schrödinger equation with the $\mathbf{A}\cdot\mathbf{A}$ term, and if Ψ^T is a solution of the Schrödinger equation without the $\mathbf{A}\cdot\mathbf{A}$ term, then Ψ and Ψ^T are related by a simple transformation

$$\Psi^T(r,t) = \exp\left[\frac{i}{\hbar} \int_{-\infty}^{t} dt' \left[\frac{e^2 \mathbf{A}(t')\cdot\mathbf{A}(t')}{2mc^2} \right] \right] \Psi(r,t) . \tag{5.6}$$

The gauge transformation, Eq. (5.6), is sometimes called a contact transformation.

The Schrödinger equation for Ψ^T and the Schrödinger equation for Ψ predict (in the absence of approximations beyond the dipole approximation) the same physical results. Next in this section we will show that our theory (Eq. (5.5)), with its approximations, predicts the same physical results whether it is derived from the Schrödinger equation for Ψ^T or the Schrödinger equation for Ψ. This corrects a well known[15,16] defect in the conventional Keldysh theory, which gives different physical

predictions depending on whether it is derived from the Schrödinger equation for Ψ^T or the Schrödinger equation for Ψ.

Let us now transform Eq. (5.5), using Eq. (5.6), to get a formula for c(p,t) that uses $\Psi^T{}_i$ instead of Ψ_i. Setting $\Psi_i = \exp[-i(e^2/2mc^2\hbar)\int^t \mathbf{A}\cdot\mathbf{A}]\,\Psi^T{}_i$, and using,

$$\exp\left[\frac{i}{\hbar}\int_{-\infty}^{t} dt'\left[\frac{e^2\,\mathbf{A}\cdot\mathbf{A}}{2mc^2}\right]\right]\left(\frac{e^2\,\mathbf{A}\cdot\mathbf{A}}{2mc^2} - i\hbar\frac{d}{dt}\right)\exp\left[-\frac{i}{\hbar}\int_{-\infty}^{t} dt'\left[\frac{e^2\,\mathbf{A}\cdot\mathbf{A}}{2mc^2}\right]\right]\Psi^T = -i\hbar\frac{d}{dt}\Psi^T \tag{5.7a}$$

yields,

$$|c(\mathbf{p},t)|^2 = \left|\frac{1}{\hbar}\int_{-\infty}^{t} dt'\exp\left[\frac{i}{\hbar}\int_{-\infty}^{t'} dt''\left(\frac{\mathbf{p}\cdot\mathbf{p}}{2m} - \frac{e\,\mathbf{p}\cdot\mathbf{A}}{mc}\right)\right]\langle \mathbf{p}\,|\,H_0 - \frac{e\,\mathbf{p}\cdot\mathbf{A}}{mc} - i\hbar\frac{d}{dt'}\,|\,\Psi_i^T(t')\rangle\right|^2. \tag{5.7b}$$

Equations (5.5) and (5.7b) are equivalent and must give the same predictions if properly evaluated. Equation (5.6) may be thought of simply as a change of variables to simplify the numerical integration of Eq. (5.5).

Equation (5.7b) is just the formula that would have followed from a Schrödinger equation that had no $\mathbf{A}\cdot\mathbf{A}$ term in the interaction Hamiltonian. We have shown then that our theory gives the same physical predictions whether it is derived from the Schrödinger equation for Ψ or the Schrödinger equation for Ψ^T. This is true because we kept the operator d/dt in the matrix elements of Eq. (5.5) and Eq. (5.7b). If, by contrast, we were to discard the d/dt term in Eq. (5.5), then such a theory, if it were derived from the Schrödinger equation for Ψ, would give physical predictions different from those of a theory derived from the Schrödinger equation for Ψ^T. In the next section we will show how to remedy this problem in an approximation in which the the d/dt operator is discarded.

To make a quantitative comparison between the numerical integration of Schrödinger's equation and the formulas derived above we will use the numerically integrated initial state $\Psi_i(t)$ defined in section 5.2. In practice we solve Schrödinger's equation without the $\mathbf{A}\cdot\mathbf{A}$ term to get Ψ^T_i directly, and then use Eq. (5.7b). To get an energy spectrum we sum all of the plane wave states $|\mathbf{p}>$ in each energy interval $(E,E+dE)$, where dE is the bin width of the spectrum of Fig. 5.2. This is a standard method of calculating a cross section with the Born approximation. A good textbook discussion of its justification is given by Gottfried[17]. The approximation is good except near the near the $E=0$ ionization threshold. At the $E=0$ ionization threshold the density of plane wave states goes to zero, whereas the true density of states does not go to zero at $E=0$.

In Fig. 5.1 we plot (dotted line) the results of our full theory: the energy spectrum predicted by Eq. (5.7b). The agreement is good enough to give us confidence in our numerical methods. The third and fourth Keldysh ionization peaks have the wrong side-lobe structure in comparison to the numerical integration, but the right cross section and shape for the central part of the peak.

The theory presented here, Eq. (5.7b) is basically Schrödinger's equation in the momentum picture simplified by two approximations. The first approximation was to discard from the basis set of Fig. 3.1 some unimportant states. The second approximation is the plane-wave approximation, Eq. (5.4). Finally, in using Eq. (5.7b) to

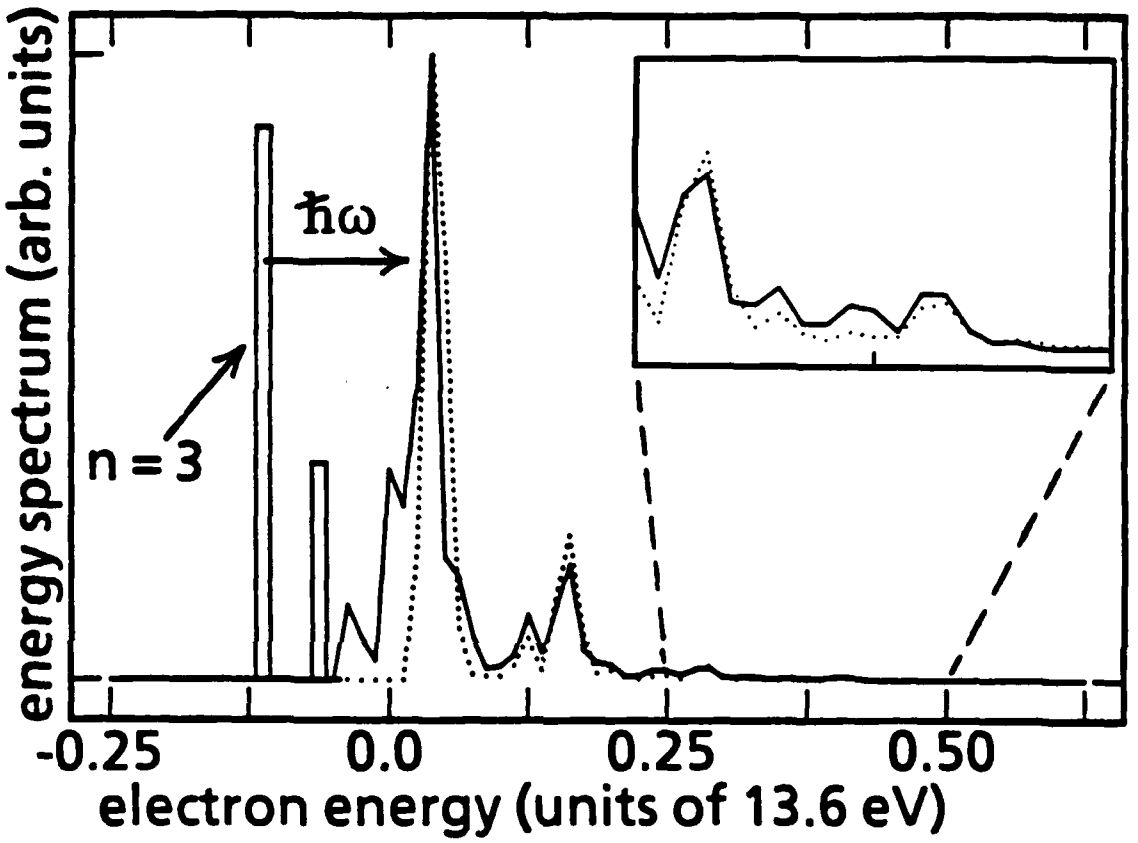

Fig. 5.1. Electron energy at the end of the laser pulse. The solid line is the prediction of numerically integrating Schrödinger's equation. The dotted line is the prediction of the Keldysh-type theory proposed here, Eq. (5.7).

calculate a cross section, the plane-wave density of states is used. This approximation is good except near the threshold of ionization[17].

Section 5.4 The Slowly-varying Population Approximation

In the previous section we used the numerically integrated initial state $\Psi^T_i(t)$ in order to test how well Eq. (5.7b) predicts the ATI spectrum. This strategy was useful in testing the theory, but the strategy is not of much use in modeling experiments. In order to make the theory of practical value in situations where Schrödinger's equation has not been or cannot be integrated, it is necessary to use an approximate Ψ^T_i . In this section we will review a standard approach to choosing an approximate Ψ^T_i , which we will call the slowly-varying population approximation. The results of this section are also necessary in order to compare our theory with the standard Keldysh theories, which are formulated in the slowly-varying population approximation.

By the slowly-varying population approximation we mean the assumption that the population of the initial state remains constant during the excitation, or is slowly varying. This approximation is commonly made in order to use formulas such as Eq. (5.7b) to calculate transition rates, or equivalently cross sections. To see the effect of this approximation on Eq. (5.7b), consider the operator $H_0 - i\hbar d/dt$ in the matrix element of Eq.(5.7b). This operator, acting on any state yields:

$$(H_0 - i\hbar\frac{d}{dt})\sum_i a_i(t)\exp(-iE_it/\hbar)|i> = \frac{\hbar}{i}\sum_i \frac{da_i(t)}{dt}\exp(-iE_it/\hbar)|i> . \quad (5.8) \qquad (8)$$

In Eq. (5.8), H_0 is the atomic Hamiltonian, E_i is the energy of the i_{th} state, and the $a_i(t)$ are the probabiltity amplitudes of the states. In the slowly-varying population approximation it is assumed that each amplitude $a_i(t)$ is constant in time or so slowly varying that da_i/dt is negligible. By the slowly-varying population approximation we mean, then, that $H_0 - i\hbar d/dt$ disappears from the matrix element of Eq. (5.7b).

In the previous section it was pointed out that conventional Keldysh theory predicts different physical results, depending on whether it is derived from the Schrödinger equation for Ψ^T, or from the Schrödinger equation for Ψ. This difficulty is avoided if the slowly-varying population approximation is correctly applied.

The next step is to apply the slowly-varying population approximation to Eq. (5.5). Since the interaction Hamiltonian now has the $\mathbf{A}\cdot\mathbf{A}$ term in it, we apply the transformation Eq. (5.6) to the wave function of Eq. (5.8). Consider the operator $H_0 - i\hbar d/dt + e^2\,\mathbf{A}\cdot\mathbf{A}/2mc^2$ acting on that state:

$$(H_0 - i\hbar\frac{d}{dt} + \frac{e^2\,\mathbf{A}\cdot\mathbf{A}}{2mc^2}) \sum_i a_i(t)\ \exp\left[-\frac{i}{\hbar}\int_{-\infty}^{t} dt'\left[\frac{e^2\,\mathbf{A}\cdot\mathbf{A}}{2mc^2}\right]\right] \exp(-iE_i t/\hbar)\,|\,i> =$$

$$\frac{\hbar}{i}\sum_i \frac{da_i(t)}{dt}\ \exp\left[-\frac{i}{\hbar}\int_{-\infty}^{t} dt'\left[\frac{e^2\,\mathbf{A}\cdot\mathbf{A}}{2mc^2}\right]\right] \exp(-iE_i t/\hbar)\,|\,i> \qquad (5.9)$$

If the $\mathbf{A}\cdot\mathbf{A}$ term is in the interaction Hamiltonian, then the slowly-varying quantity is the amplitude $a_i(t)$ of Eq. (5.9) (assuming that $a_i(t)$ is the slowly varying quantity of Eq. (5.8)). Consequently, the slowly-varying population approximation applied to Eq. (5.5) means that $da_i(t)/dt$ is negligible and $H_0 - i\hbar d/dt + e^2\,\mathbf{A}\cdot\mathbf{A}/2mc^2$ is discarded from the matrix element of Eq. (5.5). As a result, application of the slowly-varying

population approximation to Eq. (5.5) yields exactly the same formula that application of the slowly-varying population approximation to Eq. (5.7b) yielded.

To model actual experiments, or calculate cross sections, a further approximation is usually made: it is assumed that the population remains entirely in a single bound state rather that the three that make up the $\Psi_i(t)$ used in the previous section. This further approximation will not be investigated here. Instead the numerically integrated $\Psi_i(t)$ will be used in our test of the theory.

The slowly-varying population approximation and its consequence in Eq. (5.7b), $H_0 - i\hbar d/dt = 0$, are made so commonly in the theory of multi-photon processes that it is worth while to investigate its validity here. It is also used in the standard Keldysh approach, the KFR theory, to be discussed in section 5.5. So, in order to compare our theory, Eq. (5.7b), with the KFR theory, we must apply the slowly-varying population approximation to Eq. (5.7b). To do this, we remove $H_0 - i\hbar d/dt$ from the matrix element of Eq. (5.7b) and plot the results.

In Fig. 5.2 is shown (dotted line) the energy spectrum predicted by Eq. (5.7b) with the $H_0 - i\hbar d/dt$ operator discarded. The ionization peaks predicted by the theory are in the right places, but the cross section of the first Keldysh peak is wrong by a factor of 2 and the cross section of the second Keldysh peak is wrong by a factor of 4.

The d/dt operator plays such an important role in Eq. (5.7b) because of the rapid oscillations in ground state decay, as shown in Fig. 3.3(b). These rapid oscillations have a frequency of twice the frequency of the electric

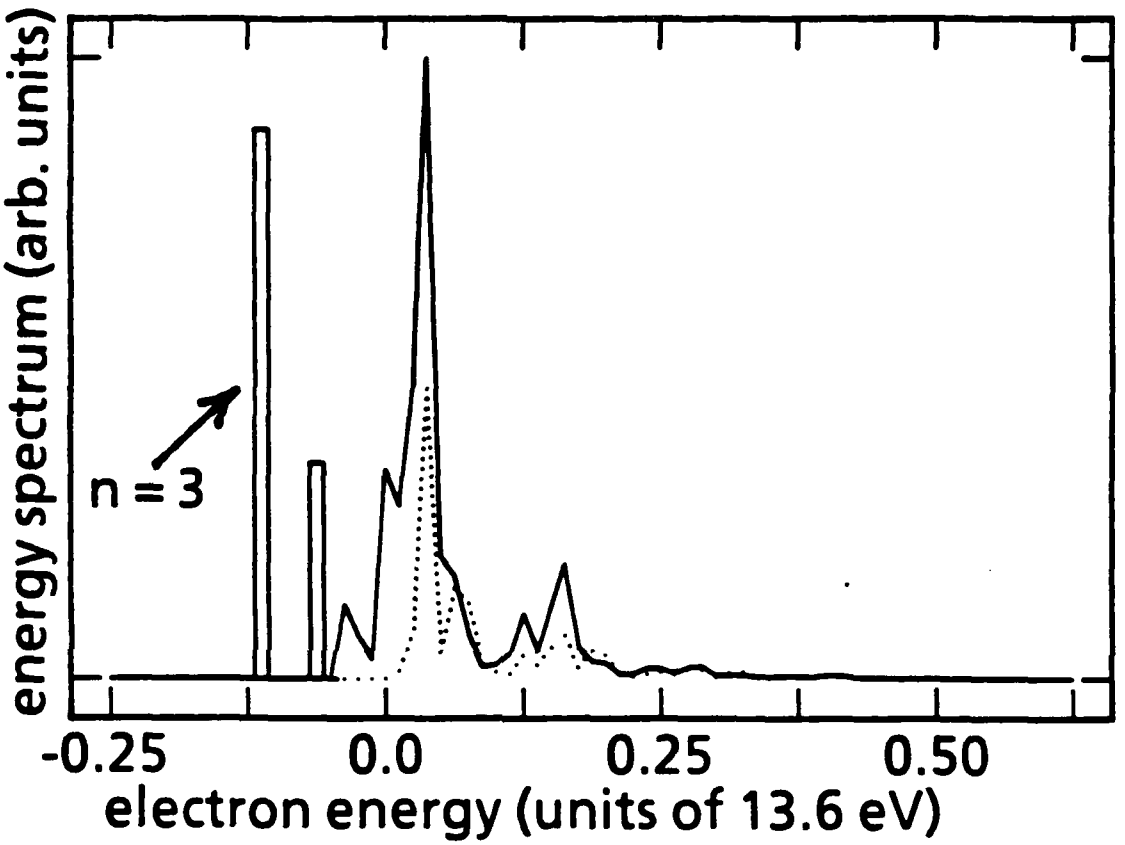

Fig. 5.2. Electron energy at the end of the laser pulse. The solid line is the prediction of numerically integrating Schrödinger's equation. The dotted line is the prediction of the Keldysh-type theory proposed here (Eq. (5.7)) in the slowly-varying population approximation.

field. They are sometimes called counter-rotating oscillations because they are due to rapidly oscillating terms in Schrödinger's equation that are discarded in the rotating-wave approximation (RWA). In terms of Eq. (5.8), the rapid oscillations mean that the functions $a_i(t)$ have parts that go as $\sin(2\omega t)$ where ω is the optical frequency. As a consequence, $H_0 - i\hbar d/dt$ gives a large contribution in Eq. (5.7b).

Section 5.5 Comparison With KFR Theory

In this section we will write down one of the better known Keldysh formulas describing ATI of atoms in intense fields, namely the KFR theory, of Keldysh, Faisal, and Reiss. The KFR formula will be compared with the formula derived in the section 5.3 and with the numerical solution of Schrödinger's equation. We will show that the two theories predict different results.

A physically appealing[6] derivation of the transition probability $|M_{fi}|^2$ describing an ATI transition in intense fields assumes that a single matrix element connects the initial atomic bound state Ψ_i to an unbound (dressed) state Ψ_f. The final state $\Psi_f(\mathbf{p},\mathbf{r},t)$ is assumed to be the Volkoff state, an exact solution of Schrödinger's equation for an unbound electron in a time-varying electric field. With these assumptions the probability of scattering a bound electron into a plane wave $\Psi_f(\mathbf{p},\mathbf{r},t)$ of momentum $\mathbf{p}$ is,

$$|M_{fi}(\mathbf{p})|^2 = \left| \frac{1}{\hbar} \int_{-\infty}^{\infty} dt' \, \langle \Psi_f(\mathbf{p},\mathbf{r},t') | \, H_{int}(t') \, | \Psi_i(\mathbf{r},t') \rangle \right|^2 , \qquad (5.10)$$

where H_{int} is the interaction Hamiltonian. The Volkoff state is

$$\Psi_f(\mathbf{p},r,t) = \Psi_0 \exp(i\,\mathbf{p}\cdot\mathbf{r}/\hbar)\ \exp\left[-\frac{i}{\hbar}\int_{-\infty}^{t} dt'\left(\frac{\mathbf{p}\cdot\mathbf{p}}{2m} + H_{int}(t')\right)\right], \qquad (5.11)$$

where Ψ_0 is the inverse of the square root of the quantization volume. The published Keldysh-type theories share a form similar to Eq. (5.10). Reiss[3] derives an equivalent formula from scattering theory. The equation is, in our notation,

$$|a(\mathbf{p},t)|^2 = \left|\frac{1}{\hbar}\int_{-\infty}^{t} dt' \exp\left[\frac{i}{\hbar}\int_{-\infty}^{t'} dt''\left(\frac{\mathbf{p}\cdot\mathbf{p}}{2m} + H_{int}(t'')\right)\right] <\mathbf{p}|\ H_{int}(t')\ |\Psi_i(t')>\right|^2 . \qquad (5.12)$$

In Eqs. (5.10), (5.11), and (5.12) the interaction Hamiltonian H_{int} is

$$-e\mathbf{p}\cdot\mathbf{A}/mc + e^2\mathbf{A}\cdot\mathbf{A}/2mc^2. \qquad (5.13)$$

Now it is straightforward to see the relationship between our theory, Eq. (5.5), and the KFR theory, Eq (5.12). In the KFR theory[4], a cross section or rate is calculated from Eq. (5.12) by choosing the initial state Ψ_i to be a single bound state of constant population, $\Psi_i = \exp(-iE_it/\hbar)|i>$. One can readily verify that substituting this initial state into Eq. (5.5) yields Eq. (5.12).

To further clarify the differences between our theory and the KFR theory, we will show how to use our theory, Eq. (5.5) and Eq. (5.7b), to calculate an ionization cross section from an initial bound state of constant population $|i>$. It follows from the discussion of sections 5.3 and 5.4 that the proper initial state of constant population to put into Eq. (5.5) to get an ionization cross section is $\Psi_i = \exp[-i\,(e^2/2mc^2\hbar)\int^t \mathbf{A}\cdot\mathbf{A}]\times\exp(-iE_it/\hbar)|i>$. The proper initial state of constant population to put into Eq. (5.7b) is $\Psi^T_i = \exp(-iE_it/\hbar)|i>$. To get the KFR equation and the related Keldysh formulas, we must put $\Psi_i = \exp(-iE_it/\hbar)|i>$ into Eq. (5.5).

Still another way to characterize the differences between the theories is this: our theory uses the dressed initial state; even when it is assumed that population in the initial state is constant, the initial state is dressed by the A·A term of the interaction Hamiltonian. The KFR uses the initial atomic state unperturbed by external fields.

It was shown in section 5.4 that the slowly-varying population approximation fails in the example of ATI discussed here. The approximation, however, is successful in a wide class of problems, and in particular may be useful in modelling other examples of ATI. For these reasons, it is worth comparing the predictions of our theory, Eq. (5.7b), (in the slowly-varying population approximation) with the KFR theory. We will show that the two theories give different predictions. The prediction of our theory is given in Fig. 5.2, and described in section 5.4. In Fig. 5.3 is shown (dotted line) the prediction of Eq. (5.12). The initial state $\Psi_i(t)$, used in Eq. (5.12) is as defined in section 5.2, the coherent superposition of three bound states. Comparison of Fig. 5.2 (our theory) and Fig. 5.3, shows that the theories predict different spectra.

Section 5.6 Conclusion

We have derived directly from Schrödinger's equation a very general formula of the Keldysh type. The general formula is valuable in two respects. First, it is this general formula that makes possible a useful comparison of Keldysh theory with the results of the numerical integration of Schrödinger's equation. The general Keldysh theory agrees in some

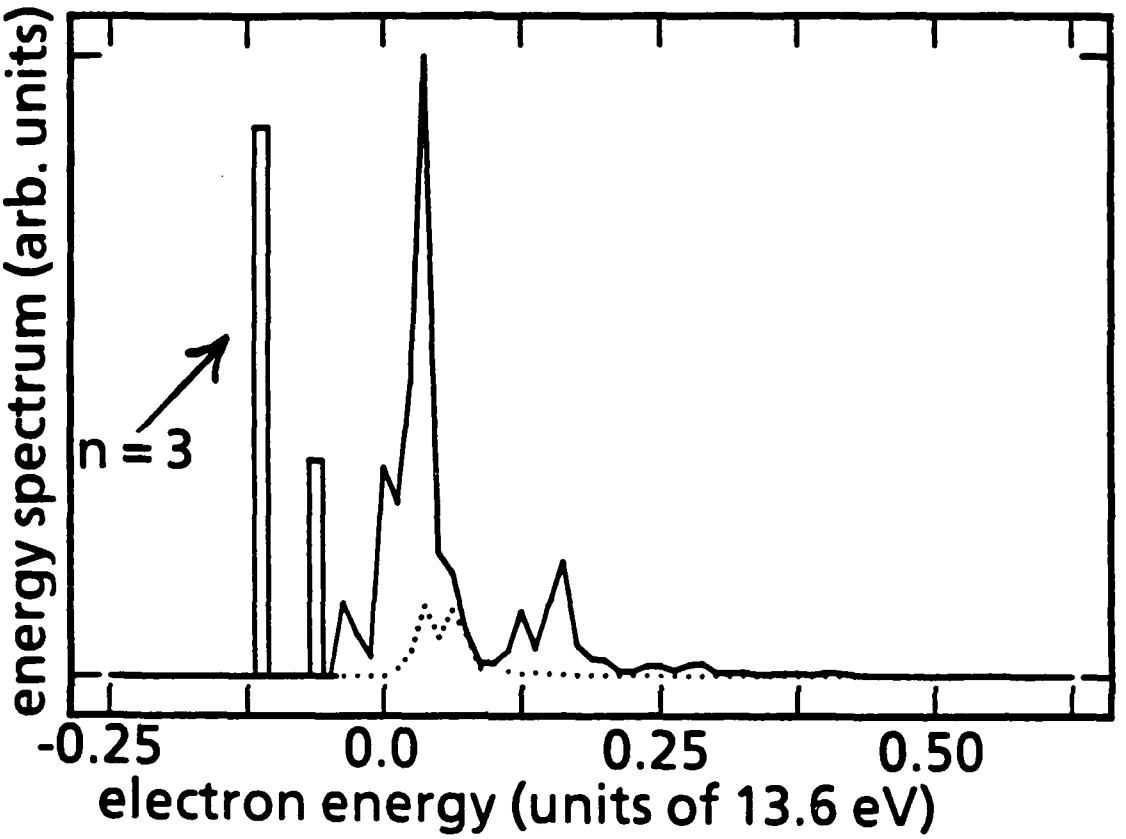

Fig. 5.3. Electron energy at the end of the laser pulse. The solid line is the prediction of the numerically integrated Schrödinger's equation. The dotted line is the prediction of KFR theory.

respects with numerical integration and disagrees in others. The comparison is in effect a numerical test of the first two major approximations necessary to derive Keldysh-type theories. The general formula is valuable in another respect. It allowed us to correct a well-known[15,16] defect in the standard KFR Keldysh theory. The standard theory gives different physical predictions depending on whether it is derived from the Schrödinger's equation with the $\mathbf{A}\cdot\mathbf{A}$ term or alternately from the Schrödinger's equation without the $\mathbf{A}\cdot\mathbf{A}$ term. We have shown that our theory gives the same physical predictions in either case. We have further shown how to preserve this invariance in the limit of the slowly-varying population approximation.

Next we have discussed at length the slowly-varying population approximation (SVPA). We done this for two reasons. The first reason was to test the agreement of our Keldysh theory in this limit with the numerical integration. This is important because so much of the theory of multi-photon processes is done in the SVPA. The second reason is that the standard Keldysh theory is in the SVPA, and so the SVPA is the limit in which our Keldysh may be compared with standard KFR Keldysh theory. We have shown that ours is not equivalent to the well-known KFR theory (section 5.5). Perhaps the most important characteristic shared by all the theories of the Keldysh type is the plane-wave approximation, Eq. (5.4).

By this set of steps that we have shown how to derive theories of the Keldysh-type directly from Schrödinger's time-dependent equation, and have numerically tested the series of approximations necessary to derive the theories.

References

1. P. Agostini, F. Fabre, G. Mainfray, G. Petite, and N. Rahman, Phys. Rev. Lett. 42, 1127 (1979).

2. L. V. Keldysh, Sov. Phys. JETP 20, 1307 (1965).

3. A. I. Nikishov and V. I. Ritus, Sov. Phys. 23, 168 (1966); F. Faisal, J. Phys. B 6, L312 (1973); H. R. Reiss, Phys. Rev. A 22, 1786 (1980).

4. D. Feldmann, B. Wolff, M. Wemhöner, and K. H. Welge, Z. Phys. 6, 293 (1987).

5. J. Javanainen and J. H. Eberly, J. Phys. B 21, L93 (1988); J. Javanainen and J. H. Eberly, Phys. Rev. A 39, 458 (1988).

6. W. Becker, R. R. Schlichter, and M. O. Scully and K. Wodkiewicz, J. Opt. Soc. Am. B 4, 743 (1987).

7. J. Kupersztych, Europhys. Lett. 4 (1), 23 (1987).

8. S. M. Susskind and R. V. Jensen, Phys. Rev. A 38, 711 (1988).

9. J. Parker and C. R. Stroud, Jr., Phys. Rev. A 40, 5651 (1989).

10. J. H. Eberly and. J. Javanainen, Phys. Rev. Lett. 60, 1346 (1988).

11. Bala Sundaram and Lloyd Armstrong, Jr., Phys. Rev. A 38, 152 (1988).

12. H. R. Gray, R. M. Whitley, and C. R. Stroud, Jr., Opt. Lett. **3**, 218 (1978); P. L. Knight, Opt. Comm. **31**, 148 (1979); P. E. Coleman and P. L. Knight, J. Phys. B **15**, 1235 (1982); P. M. Radmore and P. L. Knight, Phys. Lett. **102a**, 180 (1984).

13. D. A. Cardimona, M. G. Raymer and C. R. Stroud Jr., J. Phys. B **15**, 63 (1982); E. Kyrölä and J. H. Eberly, J. Chem. Phys. **82** (4), 1841 (1985).

14. H. A. Bethe and E. E. Salpeter, **Quantum Mechanics of One- and Two-Electron Atoms** (Plenum, New York, 1977), p. 303.

15. H. S. Antunes and L. Davidovich, Phys. Rev. Lett. **53**, 2283 (1984).

16. P. W. Milonni, Phys. Rev. A **38**, 2682 (1988); P. W. Milonni and J. R. Ackerhalt, Phys. Rev. A **39**, 1139 (1988).

17. K. Gottfried, **Quantum Mechanics**, (W. A. Benjamin, New York, 1966).

CHAPTER VI
A NUMERICAL COMPARISON OF CLASSICAL AND QUANTUM MECHANICAL ATI

Section 6.1 Introduction

In this chapter we will describe some numerical experiments we have conducted on classical above-threshold ionization of atomic hydrogen. The principal goal of this chapter is to describe a search for a classical system that exhibits energy absorption in intense fields similar to the examples of quantum mechanical above-threshold ionization described in the previous chapters.

The physical parameters of the numerical experiments will be identical with those of the ATI example studies in the previous chapter. The field will be taken to be linearly polarized, with frequency 1/8th of the Rydberg frequency. the pulse envelope will be Gaussian with a duration of three optical periods (FWHM) or about 7.5 femtoseconds. The peak pulse intensity will be $2.2 \cdot 10^{14}\,W/cm^2$. The initial state is the ($n=3$, $\ell=2$, $m=2$) state and the dipole approximation is made.

Except for a few remarks on the theory of the classical correspondence, the discussion in this chapter will be limited to numerical experiments on the example described above. Numerical experiments are powerful in some respects and limited in others. They cannot prove theorems, but they can uncover evidence of unexpected phenomena, and can serve as counter-examples to widely held beliefs. Numerical experiments permit the study

of complex systems that resist analytical methods. Like laboratory experiments, numerical experiments can provide experimental guidance when analytical methods fail.

Arguments based on the correspondence principle played a fundamental role in the early development of quantum mechanics. As a result, the classical correspondence of one-electron atoms unperturbed by external fields has been well understood from the early days of quantum mechanics. However, quantitative study of the classical correspondence of one-electron atoms interacting with external electromagnetic fields has proven to be a far more difficult problem. One of the earliest and still the most widely applied of all approaches to the problem was formulated by Wigner[1] in 1932. Wigner used the quantum mechanical wavefunction of a particle to construct a distribution function $\rho_W(\mathbf{r},\mathbf{p},t)$ that could be interpreted under some circumstances as the joint position, momentum probability distribution of the particle. Wigner showed that under certain conditions (and in the $\hbar = 0$ limit) the quantum mechanical evolution of $\rho_W(\mathbf{r},\mathbf{p},t)$ is identical to the classical evolution of a statistical ensemble of classical particles satisfying the same initial distribution in $\mathbf{r}$ and $\mathbf{p}$ as the quantum mechanical particle. The function $\rho_W(\mathbf{r},t)$, which is derived from $\rho_W(\mathbf{r},\mathbf{p},t)$ by integrating over all $\mathbf{p}$, equals the square modulus of the wave function: $\Psi^*\Psi(\mathbf{r},t)$.

The modern experimental methods of quantum optics have brought quantum optics into the regime in which classical descriptions are of considerable practical and theoretical importance. Classical dynamics, for example, yielded the first theoretical agreement[2,3] with the experiments of

Bayfield, Koch, and Gardner[4], in which highly excited hydrogen atoms were ionized with microwaves in a multi-photon process. The problem still resists a full quantal analysis, and numerical models have been restricted to one dimension. The study of the classical correspondence of quantum optics, in general, has proven to be a rich source of data on "quantum chaos", because classical dynamical systems driven by external fields sometimes exhibit chaotic behavior[5]. Another ionization phenomenon has for twenty years proven too formidable for a complete quantal analysis. Lu, Tompkins, and Garton[6] showed that the absorption spectrum near ionization threshold of an atom in a strong magnetic field shows sinusoidal oscillations. Recently a classical analysis[7] successfully yielded quantitative agreement with experiment. It was shown that the quantum mechanical spectrum could be explained very simply in terms of the closed classical orbits of an electron in the combined coulombic and magnetic fields. Recently, Yeazell and Stroud[8] have demonstrated that a Monte Carlo classical model of the dc ionization of Rydberg electron wave packets yields good agreement with experiment.

Section 6.2 Classical Model

Our approach to the classical correspondence is a Monte Carlo approach. The Monte Carlo approach to the classical correspondence may be motivated by the observation of Wigner (and earlier, Dirac) that in the $\hbar = 0$ limit a classical ensemble $\rho(\mathbf{r},\mathbf{p},t)$ may under some circumstances (a harmonic oscillator atomic potential) evolve identically as a quantum

state. (The classical distribution function $\rho(\mathbf{r},\mathbf{p},t)$ will be distinguished here from the Wigner distribution $\rho_W(\mathbf{r},\mathbf{p},t)$ by the absence of the subscript W.) Both the quantum and the classical states should have the same initial distribution in momentum and space. The initial classical distribution $\rho(\mathbf{r},\mathbf{p},t_0)$ may, for example, be derived from the Wigner distribution $\rho_W(\mathbf{r},\mathbf{p},t)$. The Husimi distribution[9] is another possibility. What is special about the Wigner distribution is that it makes the equality between $\rho_W(\mathbf{r},t)$ and $\Psi^*\Psi(\mathbf{r},t)$ exact, but at the expense of making $\rho_W(\mathbf{r},\mathbf{p},t)$ negative in some cases. Non-negative distributions, such as the Husimi distribution, may be easily constructed, but at the expense of making the equality between $\rho(\mathbf{r},t)$ and $\Psi^*\Psi(\mathbf{r},t)$ inexact. The density functions associated with the Monte Carlo distributions to be studied in this chapter must of course be non-negative functions, unlike the Wigner distribution.

What Dirac and Wigner proved many years ago were mathematical theorems revealing sufficient conditions for an exact correspondence. In this chapter we have a much more limited goal of searching for a classical system that exhibits similar behavior to the quantum mechanical hydrogen atom undergoing ATI in intense fields. In the search for such a classical system it becomes apparent that the theorems are at best a guide: $\hbar$ is not zero, the Coulomb potential is not harmonic or linear, and the Monte Carlo ρ must be greater than zero.

The main difficulty here is in choosing the initial classical ensemble. Once the initial ensemble is chosen, its classical evolution is compared with the quantum mechanical evolution of the corresponding quantum state. A precise set of classical steps that yields agreement with the

quantum mechanical result may then be offered as evidence of a classical origin to certain ATI phenomena.

Our approach to the classical correspondence will differ in some respects from the standard methods described in the literature. The Wigner method with its negative distributions cannot of course serve as a guide to the construction of the initial classical Monte Carlo ensemble. The well known Monte Carlo method of Abrines, Percival, and Richards[10] sums together all of the degenerate sub-levels (ℓ,m) of a principal quantum number n to get a spherically symmetric initial ensemble, the micro-canonical ensemble. This is the proper approach to model certain experiments, but it is unsuitable to the problem discussed in this chapter, in which the initial states are not spherically symmetric.

Let us review in four steps our approach to constructing the initial classical ensemble, which we will call $\rho(\mathbf{r},\mathbf{p},t_0)$.

Step 1: The first characteristic of the initial classical state is that, like the initial quantum eigenstate, before the laser pulse arrives it should be time independent, or stationary: $\rho(\mathbf{r},\mathbf{p},t) = \rho(\mathbf{r},\mathbf{p},t_0)$. Let us give an argument for this requirement by looking at the corresponding time-evolution series for ρ and ψ.

Any state $\rho(\mathbf{r},\mathbf{p},t)$ evolving in the absence of external fields under an atomic Hamiltonian $H_a(\mathbf{r},\mathbf{p}) = \mathbf{p}^2/2m + V(\mathbf{r})$, satisfies:

$$\rho(\mathbf{r},\mathbf{p},t) = \exp\left[- H^{op}_a(t-t_0)\right] \rho(\mathbf{r},\mathbf{p},t_0), \qquad (6.1a)$$

where the classical time evolution operator $H^{op}{}_a$ is $\Sigma(\partial H_a/\partial p_i)(\partial/\partial x_i) - \Sigma(\partial H_a/\partial x_i)(\partial/\partial p_i)$. Similarly Ψ satisfies:

$$\Psi(\mathbf{r},t) = \exp\left[- \frac{i}{\hbar} H_a(t-t_0)\right] \Psi(\mathbf{r},t_0). \qquad (6.1b)$$

In Eq. (6.1b) H_a is the quantum mechanical atomic Hamiltonian. Equation (6.1) tells us that a formal perturbation series for the evolution of ρ can be constructed that corresponds to the quantum series. When ρ is stationary then Eq. (6.1a) reduces to

$$\rho(\mathbf{r},\mathbf{p},t) = \rho(\mathbf{r},\mathbf{p},t_0), \qquad (6.2a)$$

and quantum mechanically Eq. (6.1b) is,

$$\Psi(\mathbf{r},t) = \exp\left[-\frac{i}{\hbar}E_n(t-t_0)\right]\Psi(\mathbf{r},t_0). \qquad (6.2b)$$

The equation that corresponds to Eq. (6.2a) is $\Psi^*\Psi(\mathbf{r},t) = \Psi^*\Psi(\mathbf{r},t_0)$.

The two time-evolution series of Eq. (6.1) may be easily generalized to time-dependent Hamiltonians to describe the laser interaction. We require that the initial classical state be stationary so that such a generalized time-evolution series will reduce to Eq. (6.2) (via Eq. (6.1)) in the weak-field limit.

Step 2: A stationary classical initial state may be constructed as follows: it is a set of Monte Carlo electrons, (a statistical ensemble of classical electrons), all in the same orbital ellipse. The distribution along the orbital path of the electrons is chosen so that, in the limit in which the number of electrons in the ensemble is infinite, the distribution is time independent. There is straightforward way of achieving this approximately in the numerical experiments. If, for example, 1600 electrons are used in the ensemble, then the orbital period associated with the ellipse is divided by 1600 to get a small interval of time Δt, and an electron is released into the orbit at its apogee at intervals of Δt. As a result the 1600 electrons will be distributed about the orbit, each a fixed distance (in time) from its neighbors. Spatially, the electrons are closer

together at apogee (far from the nucleus) and farther apart at perigee, (near the nucleus). These classical stationary ellipses (CSE's) are in a sense the smallest classical stationary states: all classical stationary states are superpositions of these distributions, and all superpositions of these distributions are stationary states. The microcanonical ensemble of Percival and Richards is a superposition of these ellipses (but of many different angular momenta).

Step 3: The Wigner and Dirac formulations of correspondence theory demonstrate the importance of establishing equality between the initial classical statistical ensemble $\rho(\mathbf{r},t_0)$ and the corresponding quantum distribution $\Psi^*\Psi(\mathbf{r},t_0)$. Let us next turn to this part of the problem.

It is instructive to first review the correspondence argument of Dirac.[11] Dirac observed the formal equality of certain classical Poisson brackets and quantum commutators in the $\hbar = 0$ limit. For example $[q,p]/(i\hbar)$ equals $\{q,p\}$, but $[q^2,p^2]/(i\hbar)$ is identical to $\{q^2,p^2\}$ only in the $\hbar = 0$ limit. As a result, the classical expectation value of a particular Poisson bracket will equal the expectation value of the corresponding quantum mechanical commutator in the $\hbar=0$ limit provided the classical statistical ensemble represented by $\rho(\mathbf{r},\mathbf{p},t)$ agrees with the quantum mechanical distribution in space and in momentum. Let us look at a particularly instructive example of this, the time derivative of the atomic Hamiltonian H_a: $[H_a,H]/(i\hbar)$, where H is the atomic Hamiltonian plus the $(\mathbf{p}\cdot\mathbf{A})$ interaction Hamiltonian. The atomic Hamiltonian H_a is a useful quantity because it gives the energy of the atom at the end of the pulse. Without approximation:

$$\left\{ \begin{array}{c} \frac{d}{dt} <H_a>_{classical} \\ \frac{d}{dt} <H_a>_{QM} \end{array} \right\} = [\frac{e}{mc}] \int d^3r' \, \mathbf{A}(t) \cdot \nabla V(r') \left\{ \begin{array}{c} \rho(r',t) \\ |\Psi(r',t)|^2 \end{array} \right\}. \qquad (6.3)$$

Because of the $\nabla V(r) = re^2/r^3$ term in Eq. (6.3), it is especially important that ρ and $\Psi^*\Psi$ agree to good approximation near the nucleus where the energy is absorbed. By setting L_z and L^2 equal to the corresponding quantum values, and by setting the classical energy equal to the quantum mechanical energy, the CSE's described above satisfy this requirement naturally: they have the same orbital turning points (in the radial variable r) as the quantum state.

Figure 6.1 shows the classical orbital ellipse superimposed on a coordinate system. The z direction was chosen as the polarization direction of the laser. By setting L_z , L^2 and the energy E equal to the corresponding quantum values, the classical orbit is uniqely determined except for one remaining parameter, labeled θ in Fig. 6.1. The variable θ is the angle between the electric field (in the z direction) and the major axis of the orbital ellipse. The CSE's (and any superposition of CSE's) are the natural solution of the problem in the radial variable r, but the agreement between $\Psi^*\Psi(r,t)$ and $\rho(r,t)$ is nevertheless rough.

Step 4: Now we have the problem of matching $\rho(r',t_0)$ and $\Psi^*\Psi(r',t_0)$ in θ' (which is related to r' by $z' = r'\cos(\theta')$). Energy absorption depends of course on θ': in Eq. (6.3) the term $\mathbf{A}(t)\cdot \mathbf{r}' = |\mathbf{A}(t)|r'\cos(\theta')$ appears. Each CSE, fixed in θ, is itself a broad distribution in θ', but one can imagine a superposition of such ellipses that is a better approximation of $\Psi^*\Psi(r',t_0)$ (but still not a particularly good approximation of $\Psi^*\Psi(r',t_0)$).

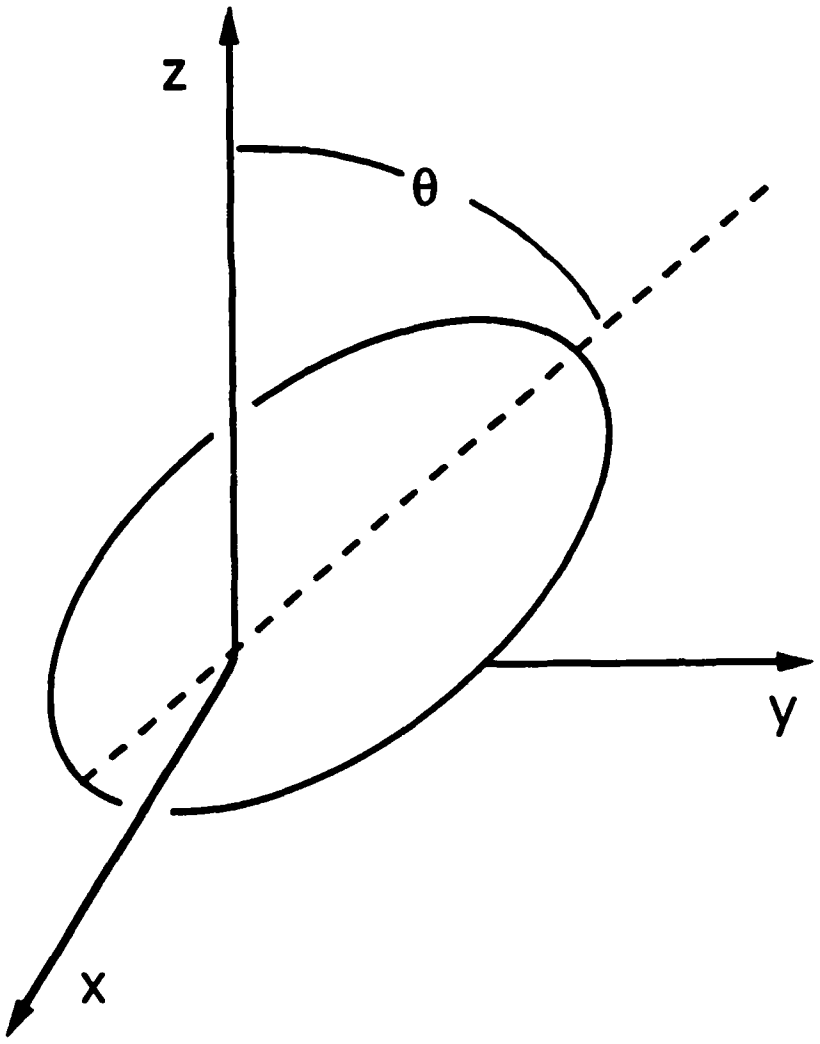

Fig. 6.1. Spatial electron distribution of the initial classical electron ensemble. The ellipse represents a classical orbit in the Coulomb potential. The nucleus of the atom is at the origin of the coordinate system. The classical orbital ellipse is populated with Monte Carlo electrons in such a way that the initial state is stationary (in the limit in which an infinite number of electrons are used). In practice, 1600 to 3200 electrons per ellipse are used.

An attempt to construct such an ensemble would be in the spirit of the Wigner appproach or the Percival and Richards approach. One can think of an infinite number of ways to construct such an ensemble, but there appears to be no unique or natural way. We cannot follow the Percival and Richards approach of summing all the degenerate sublevels of $n=3$ to get a spherically symmetric initial state. In the absence of theoretical guidance we choose to leave this problem open to numerical test by choosing initial states localized in θ.

Section 6.3 Numerical Results

In Figures 6.2, 6.3 and 6.4 the classical and quantal results are compared for three different values of θ. The dotted lines represent the energy distribution of the classical ensemble at the end of the laser pulse, as predicted by a numerical integration of Newton's equation. The solid lines represent the prediction of Schrödinger's equation described in the previous chapters. The rectangles again represent population in the $n=3$ and $n=4$ bound states. Three different numerical experiments are shown. In the three plots Figs. 6.2, 6.3, and 6.4 the initial classical ensemble is a classical stationary ellipse (CSE) with θ set to 64.7^0, 54^0, and 90^0 respectively. In the three examples described in the figures, the classical ensembles were composed of 3200 Monte Carlo electrons. The results are unchanged if 1600 Monte Carlo electrons are used.

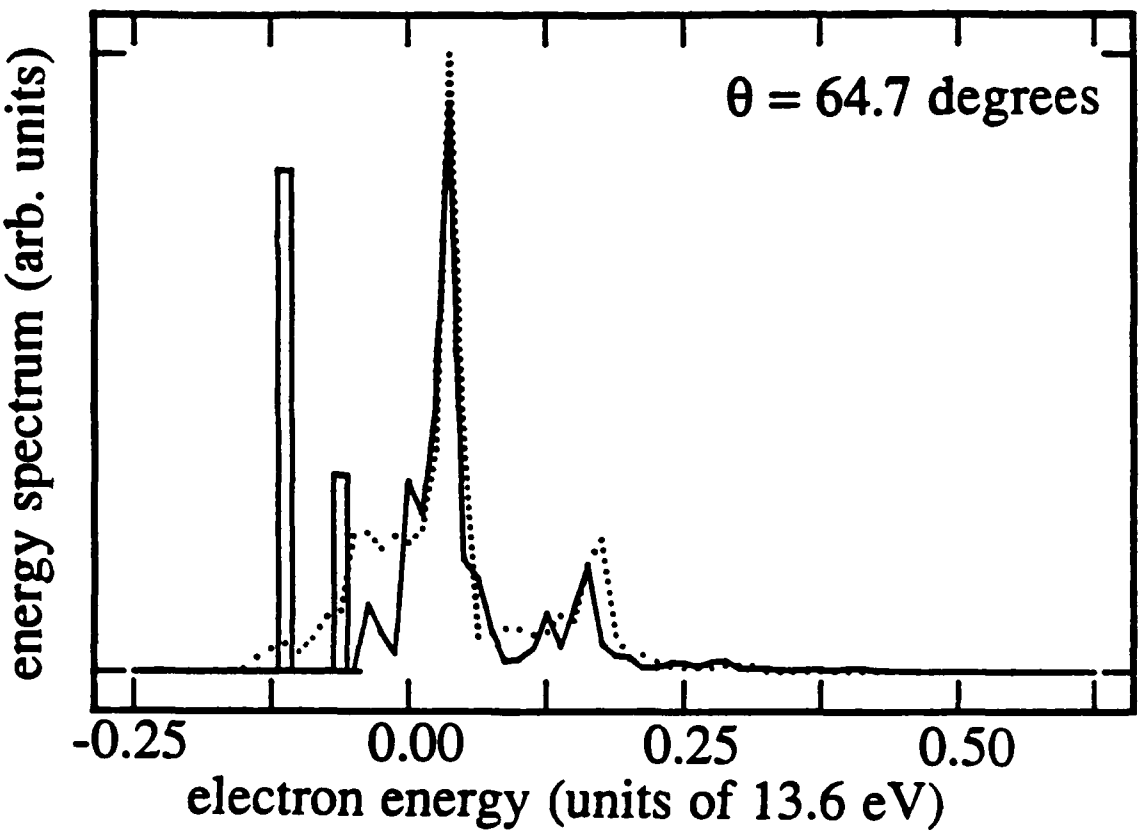

Fig. 6.2. Electron energy at the end of the excitation pulse. The separation of the x-axis hash marks is one photon in energy: 1/8th Rydberg. The curves are constructed by dividing each interval of 1/8th Rydberg into ten bins. Quantal population in each bin is plotted with a solid line and classical population in each bin is plotted with a dotted line. The rectangles represent population in bound states. Here the initial state is $(n=3, \ell=2, m=2)$ and the peak pulse intensity is $2.2 \cdot 10^{14}$ W/cm^2. The angle θ between the electric field polarization and the major axis of the orbital ellipse is in this case 64.7 degrees.

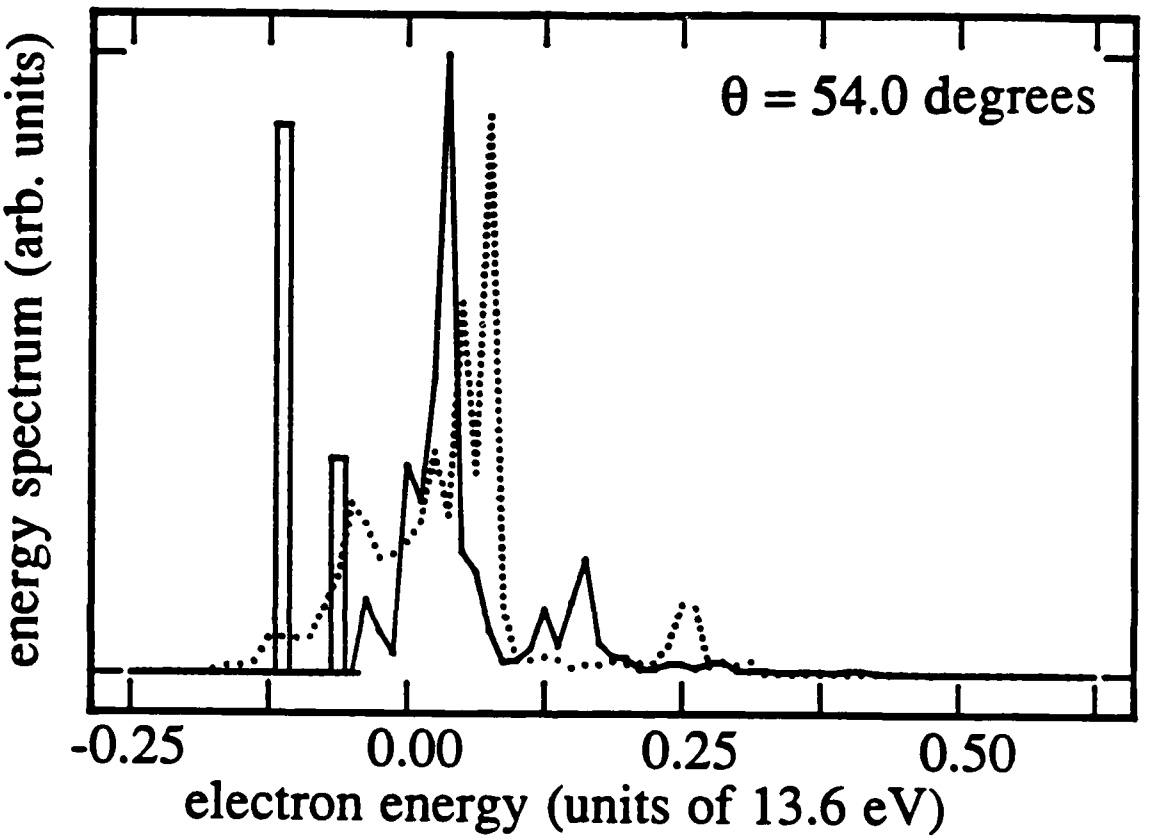

Fig. 6.3. Electron energy at the end of the excitation pulse. The initial state is ($n=3, \ell=2, m=1$), and the peak pulse intensity is $2.2 \cdot 10^{14}$ W/cm^2. The quantal population is plotted with a solid line, and the classical population is plotted with a dotted line. The angle θ between the electric field polarization and the major axis of the orbital ellipse is in this case 54.0 degrees.

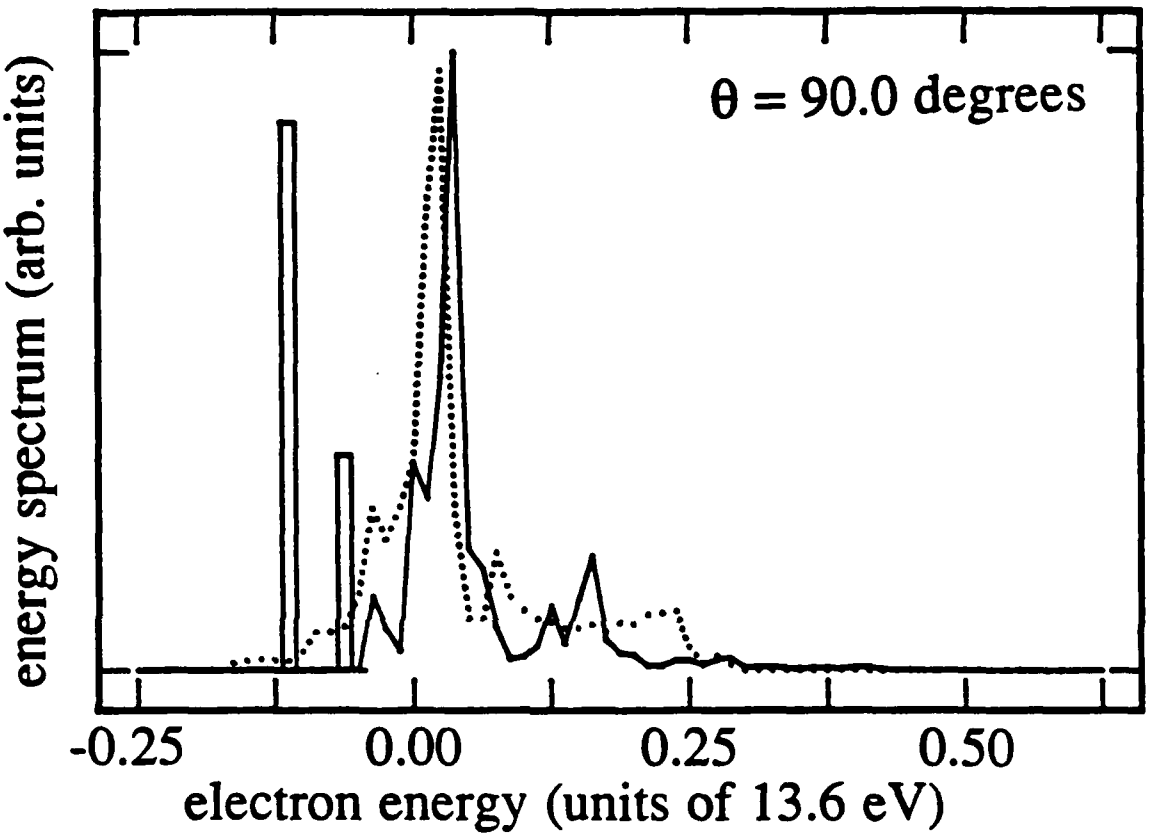

Fig. 6.4. Electron energy at the end of the excitation pulse. The initial state is ($n=3, \ell=2, m=1$), and the peak pulse intensity is $2.2 \cdot 10^{14}$ W/cm^2. The quantal population is constructed with a solid line, and the classical population is plotted with a dotted line. The angle θ between the electric field polarization and the major axis of the orbital ellipse is in this case 90.0 degrees.

All three classical distributions have a high-energy cutoff at about the third quantum peak. Figure 6.2 shows the classical results with θ chosen so that the first two classical lobes approximately overlap the first two quantum peaks. In Fig. 6.2 the agreement in classical and quantum cross sections is particularly good for the first quantum peak. What is surprising is the approximate agreement between the shapes of the classical lobes and the quantum peaks where they overlap. The first quantum peak has a width and shape similar to the first classical lobe. The agreement in shape disappears as θ is varied and the classical lobes move away from the quantum peaks.

The variation of the classical spectrum with θ may be explained very simply in terms of Eq. (6.3). Recall that θ is the angle between the electric field polarization and the major axis of the classical ellipse. As θ decreases, the electrons in the ellipse are on the average moving more nearly in the direction of the electric field as they pass near the nucleus and absorb the one of more photons of energy during ionization. As θ decreases, the $\cos(\theta')$ of Eq. (6.3) increases on the average, $d<H_a>/dt$ increases and the ensemble absorbs more energy on the average from the electric field. The argument is qualitative because θ gives us a rough measure of the distribution of ensemble only initially, before the electric field perturbs the distribution. Nevertheless, the argument agrees with the numerical results.

Section 6.4 Conclusion

Several practical applications of these numerical experiments are worth mentioning. First of all, the classical trajectories of the electrons undergoing above-threshold ionization are useful in revealing where in space and time the ionization energy is absorbed (classically) from the laser. Examination of the classical trajectories reveals that the ionization energy is absorbed within a few Bohr radii of the nucleus, and in a time short compared to both the period of the laser field and the orbital period of the electron. During the energy absorption, the external electric field is comparable to the electric field strength of the Coulomb potential. This suggests that a neither a perturbation theory based on a weak external field, or a perturbation theory based on a weak Coulomb field would be valid in this problem. The corresponding quantum mechanical estimate is difficult because the electron's wave function is smeared out over a large portion of the Coulomb potential. It is not clear where in space the energy is absorbed, and consequently reasonable estimates of the ratio of the Coulomb and external fields during the energy absorption can easily differ by orders of magnitude.

Another practical application of the classical method is the calculation of quadrupole and ponderomotive effects. Both of these effects are due to gradients in the laser's electric field that are neglected in the dipole approximation. Both of these are effects are difficult to model using the numerical methods described in chapter III for integrating

Schrödinger's equation, but are trivial to add to the classical equations. We have added the quadrupole term to Newton's equation and have redone the numerical integration of Newton's equation shown in Fig. 6.2. The results are unchanged. Quantum mechanically, quadrupole moments are easily calculated and shown to be small, but the argument used in justifying the dipole approximation requires that the energy absorption process take place in a space that is small in comparison to the wavelength of the laser field. As explained above, this is a difficult claim to justify quantum mechanically in such a complex process as ATI. The classical results are instructive, but of course we cannot claim that they will reliably predict the correct quantum mechanical results.

To summarize, we have presented evidence of a classical correspondence in an ionization process in which the classical electron is stripped from an atom in a time short compared to both the optical period and the classical orbital period. There was found little or no evidence of chaos in the classical integration: adjusting the initial condition θ slightly modified the final spectra slightly. Previous studies of the classical correspondence of quantum optics have focused on the traditional correspondence limit: Rydberg initial states ($n>>1$) in microwave fields. In the examples presented here the initial state was very quantum mechanical ($n=3$) and the field optical.

References

1. E. Wigner, Phys. Rev. 40, 749 (1932).

2. J. G. Leopold and I. C. Percival, Phys. Rev. Lett. 41, 944 (1978); D. A. Jones, J. G. Leopold, and I. C. Percival, J. Phys. B 13, 31 (1980).

3. K. A. H. van Leeuwen, G. v. Oppen, S. Renwick, J. B. Bowlin, P. M. Koch, R. V. Jensen, O. Rath, D. Richards, J. G. Leopold, Phys. Rev. Lett., 55, 2231 (1985).

4. J. E. Bayfield and P. M. Koch, Phys. Rev. Lett. 33, 258 (1974); J. E. Bayfield, L. D. Gardner, and P. M. Koch, Phys. Rev. Lett. 39, 76 (1977).

5. G. Casati, B. V. Chirikov, D. L. Shepelyansky, and I. Guarneri, Phys. Rev. Lett., 57, 823 (1986).

6. K. T. Lu, F. S. Tompkins, and W. R. S. Garton, Proc. Roy. Soc. London, Ser. A 362, 421 (1978).

7. M. L. Du and J. B. Delos, Phys. Rev. Lett. 58, 1731 (1987).

8. J. A. Yeazell and C. R. Stroud, Jr., Phys. Rev. Lett. 56, 716 (1986).

9. I. Takahashi and N. Saito, Phys. Rev. Lett. 55, 645 (1985).

10. R. A. Abrines and I. C. Percival, Proc. Phys. Soc. London 88, 873 (1966); I. C. Percival and D. Richards, J. Phys. B 10, 1497 (1977).

11. P. A. M. Dirac, **The Principles of Quantum Mechanics** (Oxford University Press, Oxford, 1958), p. 88.

CHAPTER VII
CONCLUDING REMARKS

The interaction of atoms with short laser pulses and with ultra-intense fields is a relatively new field in atomic physics. In this thesis we studied the interaction of hydrogen with coherent laser pulses in the 5 femtosecond to 10 picosecond range, in the weak-field limit, and at field intensities as high as $2 \cdot 10^{14}$ W/cm^2.

A number of new theoretical results were presented in this thesis. In chapter II we approached the problem of the interaction of atomic hydrogen with laser pulses from a novel point of view, by studying the relationship between the Fourier relation of the laser pulse $\Delta\omega\Delta t$ and the $\Delta E\Delta t$ relation of the Rydberg wave packet generated by the laser pulse. It was shown that under certain conditions the wave packet's $\Delta E\Delta t/\hbar$ acquires the laser pulse's $\Delta\omega\Delta t$. In a sense, a transform-limited laser pulse (satisfying $\Delta\omega\Delta t = 1/2$) can generate a transform-limited electron (satisfying $\Delta E\Delta t/\hbar \simeq 1/2$). To get this result it was necessary to derive a formula for the electron wave packet using the WKB approximation, and to define the electron's Δt in terms of the WKB wave packet.

It was noted that many of the assumptions made in chapter II were likely to break down in the intense fields necessary to ionize an atom substantially with 5 femtosecond pulses. The succeeding chapters were devoted to studying the interaction of hydrogen with femtosecond pulses of intensity $2 \cdot 10^{14}$ W/cm^2. Using the FGR formulation of ionization for comparison, the results of these chapters may be summarized as follows:

just about every approximation used in the derivation of FGR failed. The rotating-wave approximation, which usually works well in resonance phenomena, failed. The essential-state approximation usually employed in FGR (which assumes that all bound states but the initial state may be discarded) failed completely. Similarly there occurred transitions among continuum states (above-threshold ionization) that are ordinarily neglected in FGR calculations.

Considerable effort went into finding an example of ATI in which the complexities could be minimized and treated separately. For this reason it was assumed throughout that the initial state of the atom was the ($n=3$, $\ell=2$, $m=2$) state, and the frequency of the laser was such that the absorption of a single photon was sufficient to ionize the atom. If we had attempted to model a typical ATI experiment, then the appropriate initial state would have been the ground state, and then a complicated multi-photon process would have been required to ionize the electron.

It proved possible to isolate the various intense field phenomena, like ATI and population trapping, and study each of them separately. It was possible to model the physics of the various effects with relatively simple model atoms and provide straightforward non-perturbative theoretical methods to replace standard perturbative methods employed in the derivation of FGR.

The greatest surprise in this study was the observation, first made numerically, that even in the intense fields employed in the examples we studied, population is recaptured from the ionization continuum by bound states, and returns with just the right phase to strongly suppress

ionization. A non-pertubative theory was presented that successfully modeled the phenomenon, though not quantitatively. The theory and the corresponding numerical integration of the model atom predicted that the inhibition of ionization occurs for a variety of pulse shapes, and for a variety of atomic structures and laser intensities. The only condition for inhibited ionization was that the laser pulse have sufficiently broad bandwidth to drive both the ionizing transition as well as the transition in which the electron is recaptured by bound states other than the initial state. A further calculation showed that the rotating-wave approximation (RWA) failed in the theory to a small but noticable extent. An improved theory that did not employ the full RWA was presented. The new theory gave superior, but still not quantitative predictions. The exercise was useful in tracking down the major source of the discrepency between theory and numerical integration, because many other approximations were also made in the derivation of the theory.

In chapter V we turned to the problem of the above-threshold ionization (ATI) of hydrogen. The principal result of the chapter was the derivation of a formula related to the Keldysh-type formulas that are sometimes employed to model ATI experiments. The theory presented in chapter V was much more general than the published Keldysh-type theories, and gave good predictions of the ATI peak cross sections. The principal difference between the theory described in chapter V and the published Keldysh-type theories is that our theory, like Schrödinger's equation, is invariant under transformations in which $\Psi(r,t)$ is replaced by

$\Psi(r,t)e^{i\Lambda(t)}$. The published Keldysh-type theories are not invariant under this transformation.

In chapter VI we presented several numerical experiments on classical above-threshold ionization. Chapter VI outlined a Monte Carlo approach to the classical correspondence that differs from conventional theory. We argue at length in chapter VI that this new method is a natural approach to the problem of the classical correspondence of laser-atom interactions. The research described in chapter VI was limited to searching for a classical system that exhibits ionization behavior in intense fields similar to the quantum mechanical system studied in the previous chapters. The results were gratifying, and some evidence was found that there may be a classical origin to certain ATI peak shapes and cross sections. The evidence was based on a limited number of numerical experiments, but was surprising enough to suggest that future research in the classical correspondence of ATI may be fruitful. The widths of ionization peaks ΔE in one-photon ionization typically have an origin in the Fourier relation $\Delta E \Delta t > \hbar/2$ which is due to the fact that Schrödinger's equation is a wave equation. It would be valuable to understand why the classical diffusion-like equations of classical mechanics succeed in predicting the correct ΔE, at least in the special case presented in chapter VI.

References in Alphabetic Order

R. A. Abrines and I. C. Percival, Proc. Phys. Soc. London 88, 873 (1966).

P. Agostini, F. Fabre, G. Mainfray, G. Petite, and N. Rahman, Phys. Rev. Lett. 42, 1127 (1979).

G. Alber, H. Ritsch, and P. Zoller, Phys. Rev. A 36, 683 (1987).

H. S. Antunes and L. Davidovich, Phys. Rev. Lett. 53, 2283 (1984).

E. Arimondo and G. Orriols, Nuovo Cimento Lett. 17, 333 (1976).

P. Avan, C. Cohen-Tannoudji, J. Dupont-Roc, and C. Fabre, J. Phys. (Paris) 37, 993 (1976).

J. E. Bayfield and P. M. Koch, Phys. Rev. Lett. 33, 258 (1974).

J. E. Bayfield, L. D. Gardner, and P. M. Koch, Phys. Rev. Lett. 39, 76 (1977).

W. Becker, R. R. Schlicher, and M. O. Scully, J. Phys. B 19, L-461 (1986).

H. A. Bethe and E. Salpeter, **Quantum Mechanics of One- and Two-Electron Atoms** (Plenum, New York, 1977).

L. S. Brown, Am. J. Phys. 41, 525 (1973).

P. H. Buchsbaum, R. R. Freeman, M. Bashkansky, and T. J. McIlrath, J. Opt. Soc. B 4, 760 (1987).

D. A. Cardimona, M. G. Raymer and C. R. Stroud Jr., J. Phys. B 15, 63 (1982).

G. Casati, B. V. Chirikov, D. L. Shepelyansky, and I. Guarneri, Phys. Rev. Lett., 57, 823 (1986).

C. Cohen-Tannoudji, B. Diu, and F. Laloe, **Quantum Mechanics** (Wiley, New York, 1977), p. 62.

P. E. Coleman and P. L. Knight, J. Phys. B 15, l235 (1982).

P. A. M. Dirac, **The Principles of Quantum Mechanics** (Oxford University Press, Oxford, 1958) p. 88.

M. L. Du and J. B. Delos, Phys. Rev. Lett. 58, 1731 (1987).

J. H. Eberly and. J. Javanainen, Phys. Rev. Lett. 60, 1346 (1988).

F. H. M. Faisal, J. Phys. B 6, L312 (1973).

M. V. Fedorov and A. M. Movsesian, J. Opt. Soc. Am. B 6, 928 (1988).

D. Feldmann, B. Wolff, M. Wemhöner, and K. H. Welge, Z. Phys. 6, 293 (1987).

R. R. Freeman, P. H. Buchsbaum, H. Milchberg, S. Darack, D. Schumacher, and M. E. Geusic, Phys. Rev. Lett. 59, 1092 (1987).

H. R. Gray, R. M. Whitley, and C. R. Stroud, Jr., Opt. Lett. 3, 218 (1978).

W. A. Henle, H. Ritsch, and P. Zoller, Phys. Rev. A 36, 683 (1987).

J. Javanainen and J. H. Eberly, J. Phys. B 21, L93 (1988).

J. Javanainen and J. H. Eberly, Phys. Rev. A 39, 458 (1988).

K. Gottfried, **Quantum Mechanics**, (W. A. Benjamin, New York, 1966).

D. A. Jones, J. G. Leopold, and I. C. Percival, J. Phys. B 13, 31 (1980).

L. V. Keldysh, Sov. Phys. JETP 20, 1307 (1965).

P. L. Knight, Opt. Comm. 31, 148 (1979).

J. Kupersztych, Europhys. Lett. 4, 23 (1987).

E. Kyrölä and J. H. Eberly, J. Chem. Phys. 82 (4), 1841 (1985).

K. A. H. van Leeuwen, G. v. Oppen, S. Renwick, J. B. Bowlin, P. M. Koch, R. V. Jensen, O. Rath, D. Richards, J. G. Leopold, Phys. Rev. Lett., 55, 2231 (1985).

J. G. Leopold and I. C. Percival, Phys. Rev. Lett. 41, 944 (1978).

K. T. Lu, F. S. Tompkins, and W. R. S. Garton, Proc. Roy. Soc. London, Ser. A 362, 421 (1978).

P. W. Milonni, Phys. Rev. A 38, 2682 (1988).

P. W. Milonni and J. R. Ackerhalt, Phys. Rev. A 39, 1139 (1988).

A. I. Nikishov and V. I. Ritus, Sov. Phys. 23, 168 (1966).

L. Pan, L. Armstrong, Jr., and J. H. Eberly, J. Opt. Soc. Am. B 3, 1319 (1986).

J. Parker and C. R. Stroud, Jr., Phys. Rev. Lett. 56, 716 (1986).

J. Parker and C. R. Stroud, Jr., Physica Scripta T12, 70 (1986).

J. Parker and C. R. Stroud Jr., Phys. Rev. A 35, pp. 4226-4237 (1987).

J. Parker and C. R. Stroud Jr., Phys. Rev. A 40, 5651-5658 (1989).

I. C. Percival and D. Richards, J. Phys. B 10, 1497 (1977).

W. H. Press, B. P. Flannery, S. A. Teulosky, and W. T. Vetterling, Numerical Recipes (Cambridge University Press, Cambridge, 1986) p. 582.

Letters on Wave Mechanics (edited by K. Przibram), Philosophical Library (1967).

P. M. Radmore and P. L. Knight, Phys. Lett. 102a, 180 (1984).

H. R. Reiss, Phys. Rev. A 22, 1786 (1980).

H. R. Reiss, J. Phys. B 20, L-79 (1987).

E. Schrödinger, Natürwissenschaften 28, 664 (1926).

B. Sundaram and Lloyd Armstrong, Jr., Phys. Rev. A 38, 152 (1988).

S. M. Susskind and R. V. Jensen, Phys. Rev. A 38, 711 (1988).

J. H. Van Vleck, Proc. N. A. S 14, 178 (1928).

E. Wigner, Phys. Rev. 40, 749 (1932).

A. ten Wolde, L. D. Noordam, H. G. Muller, A. Lagendijk and H. B. Van Linden van den Heuvell, Phys. Rev. Lett. **61**, 2099 (1988).

J. A. Yeazell and C. R. Stroud, Jr., Phys. Rev. A **35**, 2806 (1987).

J. A. Yeazell and C. R. Stroud, Jr., Phys. Rev. Lett. **60**, 1494 (1988).

J. J. Yeh, C. M. Bowden, and J. H. Eberly, J. Chem. Phys. **76**, 5936 (1982).